**Title**
Synthesis and Defect Science and Engineering of Two-Dimensional Materials



**Author**
Chan, Leslie

**Publication Date**
2019

Peer reviewed|Thesis/dissertation

# Synthesis and Defect Science and Engineering of Two-Dimensional Materials

by

Leslie L. Chan

A dissertation submitted in partial satisfaction of the

requirements for the degree of

Doctor of Philosophy

in

Chemical Engineering

in the

Graduate Division

of the

University of California, Berkeley

Committee in charge:

Professor Roya Maboudian, Chair
Professor Carlo Carraro
Professor Ali Javey

Summer 2019

**Abstract**

Synthesis and Defect Science and Engineering of Two-Dimensional Materials

by

Leslie Lefang Chan

Doctor of Philosophy in Chemical Engineering

University of California, Berkeley

Professor Roya Maboudian, Chair

Rapid scaling of silicon-based transistors has enabled remarkable performance enhancements in integrated electronics. However, silicon-based transistors are quickly reaching theoretical scaling limits as a result of short channel effects dictated by silicon's intrinsic material properties. As such, there is a need for alternative materials that can transcend or better address these limitations. Scaling theory suggests that atomically thin, pristine semiconductors can enable more aggressive shrinking of the gate length. Given these requirements, two-dimensional materials (2DMs) have emerged as promising alternatives because they can be scaled down to single or few atomic layers, have no dangling bonds, and exhibit unique electrical properties.

Despite the burgeoning trove of proof-of-concept demonstrations of 2DM-based devices, large-scale fabrication and commercialization remain elusive. At this time, two of the most pressing shortcomings include (1) the transfer step requirement, wherein the 2DM must be physically transferred from a growth substrate to the target substrate, and (2) the high contact resistance between the 2DM and metal contacts. These device requirements create significant bottlenecks and challenges that limit the current feasibility of 2DM implementation in everyday devices. This work focuses on two particular classes of two-dimensional materials—graphene and transition metal dichalcogenides—and highlights some of the progress made towards addressing both of these device-

related issues.

To start, this work details the development of improved transfer-free graphene synthesis by chemical vapor deposition (CVD) directly on $SiO_2$. We outline an expansion of the parameter space that optimizes process conditions, using nickel and copper as metal catalysts and gaseous methane as the carbon precursor. We introduce a mechanism based on carbon permeability that provides deeper insight into the growth process. Low-energy electron microscopy (LEEM) is utilized to showcase some of the intrinsic differences between nickel and copper that lead to contrasting results. In the end, we demonstrate reproducible, monolayer graphene with low defect density using nickel as a catalyst, and reproducible, 2–3 layer graphene with uniform coverage using copper as a catalyst.

To address the high metal–2DM contact resistance, mild hydrogen plasma treatment is applied to $WSe_2$. X-ray photoemission spectroscopy (XPS) indicates that $H_2$ plasma treatment selectively induces selenium vacancies in the $WSe_2$ lattice, resulting in controllable n-doping with increasing plasma treatment times. $WSe_2$ n-FETs fabricated with $H_2$ treatment on the contact regions demonstrate two orders of magnitude decrease in contact resistance.

By addressing some of the challenges related to graphene transfer and TMDC contact resistance, these studies help establish a foundation towards scalable integration of 2DMs in beyond-silicon electronics.

# Nomenclature

**2DM** two-dimensional material.

**AES** Auger electron spectroscopy.

**AFM** atomic force microscopy.

**CVD** chemical vapor deposition.

**FET** field-effect transistor.

**FFT** fast Fourier transform.

**FWHM** full width at half maximum.

**HOPG** highly-oriented pyrolytic graphite.

**ICP** inductively coupled plasma.

**LEED** low-energy electron diffraction.

**LEEM** low-energy electron microscopy.

**$MoS_2$** molydenum disulfide.

**PSD** power spectral density.

**$R_c$** contact resistance.

**SAM** self-assembled monolayer.

**SPLEEM** spin-polarized low-energy electron microscopy.

**SPM** scanning probe microscopy.

**TAM** texture analysis microscopy.

**TMDC** transition metal dichalcogenide.

**UHV** ultra-high vacuum.

**$WSe_2$** tungsten diselenide.

**XPS** X-ray photoemission spectroscopy.

**XRD** X-ray diffraction.

# List of Figures

# Contents

# Acknowledgments

Graduate school is not an independent pursuit but rather a collaborative journey. I would like to thank everyone who fueled this process with immeasurable contributions of scholarship, optimism, and support.

I would like to express my deepest gratitude to my advisor Roya Maboudian, who guided me through the uncertain forest that is scientific research. I appreciate the freedom that was granted to pursue many projects, yielding plentiful successes, ample failures, and deep personal growth. Thank you for giving me time and space to get lost in problems while gently keeping me grounded. I am grateful not only for your encouragement, but also for your patience, kindness, and understanding throughout. Thank you for fostering a congenial lab community, managing group activities, and supporting us all. I always appreciated the variety of projects the Maboudian Lab pursues—thank you for leaning into interesting research topics and encouraging us to tackle real-world problems with tangible solutions. It has been a distinct pleasure working together.

I would also like to thank Carlo Carraro for being a phenomenal source of intellectual advice, rapport, and guidance. I learned immensely during our valuable discussions filled with value-less Greek letters. Your mathematical facility, physics prowess, and topical expertise inspired many fruitful outcomes in this and other work. Thank you to my committee member Ali Javey for additional support and the insightful collaboration that helped me get a head start on my research.

Thank you to my many collaborators on various projects; some results are presented here, some are not, but all were impactful in my lab experience. Many deep thanks go to Dung-Sheng Tsai, Zhongtao Wang, Yuhui Xie, Justin Cheng, and Hai Liu for their contributions to the graphitization work. Tim Schultz, Ning Wang, Gary Yama, Uma Krishnamoorthy, Franz Laermer, and the rest of the Bosch team were incredibly supportive collaborators. Thank you to Andreas Schmid and Gong Chen for unending patience and guidance on the low-energy electron microscopy projects, as well as Andre Cauduro, Kevin Franke, and Roberto Lo Conte for SPLEEM support. Hu Long and Wenjun Yan were wonderful teammates on the transition-metal dichalcogenide aerogel work. Thank you to Mahmut Tosun and Ali Javey for getting me started on the right track with the tungsten diselenide plasma project. Ryan Yao and Neel Raman's patience

and eagerness made undergraduate mentorship all the more fulfilling. All the staff scientists who trained and assisted me on various tools at Lawrence Berkeley National Lab, Marvell NanoLab, and the Biomolecular Nanotechnology Center—Ed Barnard, Emory Chan, Virginia Altoe, Tracy Mattox, Scott Dhuey, Mike Elowson, Rich Hemphill, Allison Dove, Ryan Rivers, Paul Lum—thank you.

These research efforts were supported by Bosch, Samsung, and the National Science Foundation Graduate Research Fellowship under Grant No. 1106400. Work performed at the Molecular Foundry was funded by the Director, Office of Science, Office of Basic Energy Sciences, Material Sciences and Engineering Division of the U.S. Department of Energy under Contract No. DE-AC02-05CH11231. Additional funding, guidance, and support was provided by Berkeley Science and Actuator Center industrial members.

The Maboudian Lab has hosted some of the kindest, hardest-working, most inspiring people I have ever known. Lunet E. Luna taught me the true meaning of integrity, determination, and grit. Anna Harley-Trochimcyzk showed me what it means to be a fearless leader and Renaissance woman. Steven DelaCruz, thank you for being there through it all. Thanks to all the Maboudian Lab members past and present for the workplace community: Raphi Brechbühler, Ping Cheng, Siyi Cheng, Lucas Chi, Adrian Davey, Xiang Gao, Yuan Gao, David Gardner, Sam He, Chuan-Pei Lee, Ying Li, Peter Lobaccaro, Arthur Montazeri, Sinem Ortaboy, Aifei Pan, Ameya Rao, Yong Xia, Tina Yang, Gina Zaghi.

Many important people and programs enriched my time at UC Berkeley. Special thanks to Carlet Altamirano for matchless dedication to graduate students. Much-deserved recognition goes to the Chemical and Biomolecular Engineering Graduate Student Advisory Committee for fostering a united department community. Thank you Mike Cable, Dalene Schwartz Corey, Richard Lossing, Kim Ly, and the Berkeley Sensor & Actuator Center for inviting me to contribute and learn from all the conferences, symposia, and outreach events. The Graduate Women of Engineering, Society of Women Engineers, and Women in Science and Engineering provided mentorship opportunities that were gratifying reminders of our responsibility to pay it forward in addressing STEM diversity. Sincerest thanks go to Hadley Sikes for inspiring me to go on this path in the first place. Thank you for providing lasting encouragement and restoring optimism even in our limited times together. I would like to recognize Jeff Davis for the astute pedagogy that helped me grow so much personally, academically, and musically. I would also like to thank members of the World Carillon Federation, the Guild of Carillonneurs in North America, and the Berkeley Carillon Guild for bringing balance and perspective to my life.

Berkeley has not been an idle idyll. To my roommates past and present: words are insufficient to express my gratitude. Thank you for all the conversations short and long that brought immeasurable clarity to my life. Thank you to Tom and Candy Simonen,

whose open-hearted generosity transported me into a glorious world for part of the year. A reverential nod goes to Berkeley Bowl, the Cheese Board Collective, David Lance Goines, and Alice Waters for friendly neighborhood jaunts and conversations, epitomizing the utopia that is Berkeley, California. What a special luxury it has been to live and breathe Berzerkeley.

Thank you to my friends near and far, new and old. Thanks to those in the department for indulging in thermodynamics chatter; thanks to those outside of the department for dynamically chatting about non-thermo. Much appreciation goes to campus peers and faculty for teaching me volumes: I am decibels wiser about the properties of magnetotactic bacteria, the assets of the Logic Library, the techniques of printmaking, the critiques of FRCP Rule 12(b)(6), and the evolution of Proto-Indo-European language. Deepest respects go to my graduate school elders at UC Berkeley, MIT, and elsewhere who paved the way as my exemplars. Grateful acknowledgments go to my East Bay friends for being paragons of diversity and inclusion. Thank you to my Bay Area tech friends for the vicarious opportunities. Thank you, all, for teaching me new things, challenging me to think critically, and accepting me into your communities with open arms.

Finally, I would like to thank my family—Lim, Yung, and Lawrence—for being there with me all the way. Thank you for laughing off my doubts, putting things in perspective, and bringing endless joy into my life.

# Chapter 1

# Introduction

## 1.1 Introduction to two-dimensional materials

Two-dimensional materials (2DMs) have surged into the limelight as a unique class of materials with remarkable electronic, optoelectronic, mechanical, and chemical properties [1–3]. These layer-dependent properties, coupled with ultimate atomic scalability, have enabled impressive demonstrations of applications from wearable devices to chemical sensors to organic light-emitting diodes [4–7]. Two preeminent 2DMs include graphene and transition metal dichalcogenides, which have uniquely valuable properties in their own rights.

### 1.1.1 Graphene

Graphene, the monolayer form of graphite, consists of $sp^2$-hybridized carbon atoms arranged in a hexagonal lattice with bond lengths of 1.42 Å and in-plane lattice constant 2.46 Å [8]. Graphene has long been touted for its atomic scalability—its single-layer form is the ultimate demonstration of material thinness. In addition, graphene has impressive electronic and optoelectronic properties including, but not limited to, a high theoretical electron mobility ($2 \times 10^5$ cm$^2$ V$^{-1}$ s$^{-1}$ [9]), large Young's modulus (1 TPa [10]), high thermal conductivity ($> 3000$ W m K$^{-1}$ [11]), and high optical transparency [2, 12].

A multitude of applications have been demonstrated and continue to be explored for graphene [2–7, 12–16]. As Ferrari *et al.* write in a roadmap guided by the European Graphene Flagship, "[...] it is not a question of if, but a question of how many applications will graphene be used for, and how pervasive it will become" [4]. From electronics to spintronics and optoelectronics, from sensors to energy storage to biomedical applications, graphene continues to assert its presence as a basis for "disruptive technology" [4].

Graphene synthesis has been a thriving topic of investigation. Common approaches largely fit into two categories: bottom-up approaches, where a carbon-based precursor is used to form graphene, and top-down approaches, where bulk graphite is exfoliated down to a single- or few-layer scale [2, 7, 15, 17].

While original work and proof-of-concept demonstrations made and continue to make use of mechanical exfoliation—using adhesive tape on bulk graphite to extract graphene flakes—there are a number of alternative methods, each with their own inherent benefits, shortcomings, and suitable applications [2, 7, 15, 17]. For instance, liquid-phase exfoliation offers a way to scalably manufacture graphene, but it is more difficult to control layer number and ensure quality; this may prove sufficient for applications such as conductive inks [2]. Silicon carbide decomposition, in which graphene is obtained from SiC by subliming silicon at high temperatures (>1000 °C), produces high-quality graphene sheets but is relatively costly [2]. Chemical vapor deposition has emerged as perhaps the most viable technique for large-scale manufacturing: as a bottom-up method, it is controllable, scalable, and conducive to integrated manufacturing [18]. Each technique comes with its own benefits and drawbacks; ultimately, synthesis method selection is a corollary of cost, throughput, and quality optimization.

### 1.1.2 Transition metal dichalcogenides

Transition metal dichalcogenides (TMDCs) are characterized by atomic trilayers of the form $MX_2$, where two chalcogen atoms ($X$) are covalently bonded to a transition metal atom ($M$) in an $X$-$M$-$X$ configuration (Figure 1.1) [3, 19]. Like other 2DMs, individual layers—typically $\sim$ 6-7 Å thick—are held together by weak van der Waals forces, making TMDCs readily scalable down to monolayer thickness [19]. However, these materials offer a compelling alternative over graphene because they exhibit not only a non-zero band gap, but also an indirect-to-direct band gap transition from bulk to monolayer form as a result of quantum confinement effects [3, 20–22]. This property is particularly valuable for applications from field-effect transistors and logic devices to catalysis and sensing.

Methods of producing TMDCs have largely followed the lead from earlier studies on the paradigmatic graphite [5, 23–25]. Like graphite, bulk TMDCs can similarly be mechanically exfoliated using adhesive tape to produce high-quality TMDC flakes of various thicknesses. Liquid-phase exfoliation has also demonstrated promise, but some quality and side-reaction issues remain to be addressed [3]. Chemical vapor deposition remains a more viable alternative that enables scalable synthesis without compromising quality to such an extent [25].

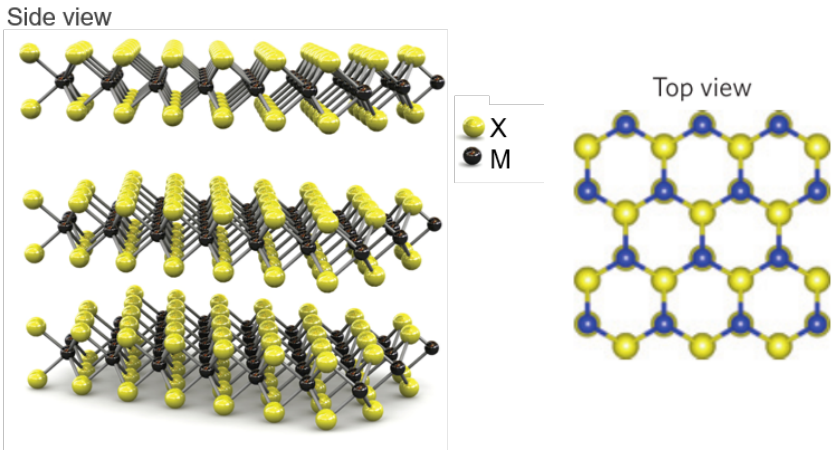


Figure 1.1: Layered structure of transition metal dichalcogenides [19].

## 1.2 Barriers to high-performance applications

While contributions to 2DM literature continue to increase, there is still a significant barrier between proof-of-concept devices and scalable reality. In particular, high-performance applications stipulate stringent quality specifications that are not currently feasible with existing technologies.

### 1.2.1 Fabrication challenges of graphene

Chemical vapor deposition (CVD) has risen as an ideal choice for scalable production of graphene [16, 18, 26]. However, CVD graphene is typically transferred from a generic metal growth substrate onto the desired insulating substrate; this extra step can lead to defects that ultimately result in poor device performance. Several groups have demonstrated metal-catalyzed direct CVD-graphene growth on insulating substrates, but the final graphene products are deficient in quality and uniformity [27].

### 1.2.2 Quality control of transition metal dichalcogenide devices

In contrast to graphene, which requires a disparate, foreign metal catalyst to lower the thermodynamic barrier to CVD growth, transition metal dichalcogenides can be catalyzed simply with the intrinsic transition metal or related transition metal oxide [5, 23–25].

In the case of TMDC-based applications, device performance is limited by other fundamental issues such as large contact resistances [28–31]. To lower the contact resistance,

intentional doping can be used to reduce the depletion width (*i.e.*, the Schottky barrier width), increasing the probability of electron tunneling [32]. To date, controllable methods for doping TMDCs *via* defect engineering are still in fairly early stages of study [33–36].

## 1.3 Outline of this work

The goal of this research is to investigate methods that can improve the performance of two-dimensional materials in electronics and sensing applications. Namely, this work highlights pre-processing (*i.e.*, synthesis) and post-processing (*i.e.*, defect engineering) approaches bringing graphene and transition metal dichalcogenides closer to scalable device implementation.

Chapter 2 explores progress that has been made developing transfer-free graphene synthesis methods. Specifically, a direct method of synthesizing graphene on $SiO_2$ using metal-catalyzed low-pressure chemical vapor deposition is optimized and discussed. Two catalysts commonly used for top-layer graphene growth are discussed in particular: nickel and copper.

Chapter 3 is focused on fundamental understanding of the thermodynamic processes that are crucial to transfer-free growth, namely spinodal dewetting. In this section, we use low-energy electron microscopy in ultra-high vacuum to elucidate the mechanisms of synthesis and modification of graphene.

Chapter 4 looks into the judicious modification of transition metal dichalcogenides using plasma treatment to improve electronic performance (*i.e.*, lower contact resistance) in field effect transistors.

Chapter 5 provides a summary of this research and outlook to the future.

# Chapter 2

# Metal-induced graphitization with gaseous methane

## 2.1 Introduction

Silicon-based transistors are quickly reaching theoretical scaling limits (*i.e.*, $\sim 5$ nm gate lengths) as a result of short channel effects dictated by silicon's intrinsic material properties [37]. To address this, alternative materials have been proposed: scaling theory suggests that atomically thin, pristine semiconductors can enable more aggressive shrinking of the gate length [38]. Given these requirements, graphene has emerged as a promising channel material because it can be scaled down to a single atomic layer, has no dangling bonds, and has superior electrical properties such as high electron mobility [39].

Large-scale fabrication of high-quality, high-uniformity graphene for integrated devices has remained elusive. Several methods of obtaining graphene include mechanical exfoliation and liquid-phase exfoliation, but these have challenges in scalability and layer number control, respectively. CVD has emerged as the predominant approach because it enables scalable, controllable production of graphene while optimizing quality and cost. To satisfy the stringent performance requirements of electronic devices, CVD graphene methods still need to address the transfer step: typically, CVD graphene is transferred from a generic metal growth substrate onto the desired substrate (*e.g.*, $SiO_2$). This extra transfer often leads to wrinkles, contamination, and breakage, ultimately resulting in poor device performance. Several groups have demonstrated metal-catalyzed direct CVD-graphene growth on insulating substrates, but the final graphene products are deficient in quality and uniformity [27].

This work details the development of improved transfer-free CVD graphene synthesis directly on $SiO_2$. We outline an expansion of the parameter space that optimizes process conditions, using nickel and copper as metal catalysts and gaseous methane as

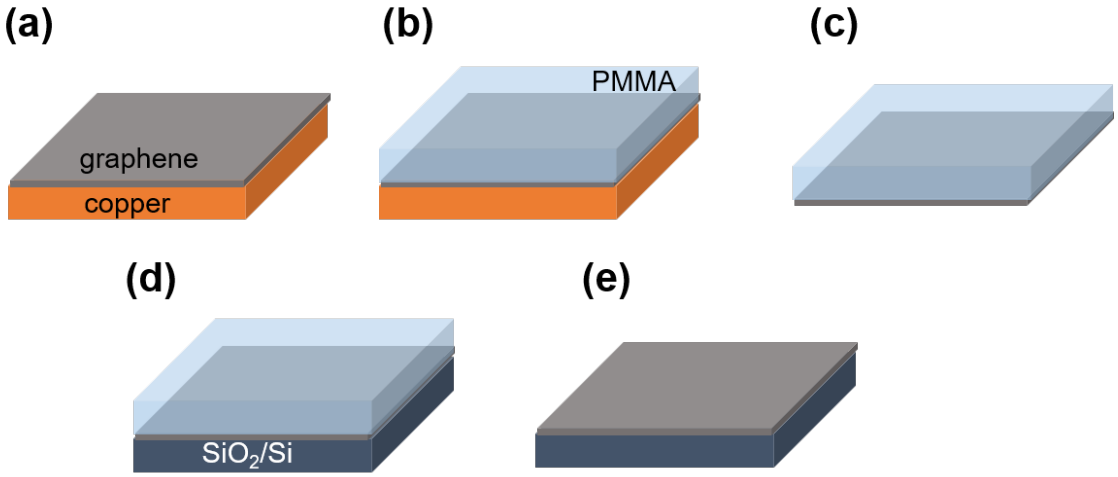


Figure 2.1: Schematics of representative polymer-assisted wet graphene transfer process. (a) CVD graphene grown on copper foil, (b) poly(methyl methacrylate) deposition, (c) copper etch and rinse, (d) transfer to desired substrate, (e) polymer removal.

the carbon precursor. We introduce a mechanism based on carbon permeability that provides deeper insight into the growth process. In the end, we demonstrate reproducible, monolayer graphene with low defects using nickel as a catalyst, and reproducible, 2–3 layer graphene with uniform coverage using copper as a catalyst. Hall mobility measurements of nickel- and copper-catalyzed graphene on $SiO_2$ at room temperature are 352 $cm^2/V{\cdot}s$ and 124 $cm^2/V{\cdot}s$, respectively, within the same order of magnitude as values reported in literature for transfer-free graphene [27]. Ultimately, these studies seek to inform judicious choices of process parameters that will lead to high-quality, uniform, layer-controlled graphene for scalable integration in beyond-silicon electronics.

### 2.1.1 Motivation for transfer-free synthesis

Recent research is bringing rapid improvements to scalable production of graphene via CVD, addressing cost, reproducibility, and availability. At this time, CVD is widely regarded as the ideal method for fabricating large-scale graphene films with uniform thickness and high quality. However, conventional CVD methods require a metal film or foil growth substrate to catalyze the reaction to occur at reasonable process temperatures [14, 18, 26, 40–42]. Nickel and copper catalysts are by far the most commonly explored, but these do not correspond with the typical desired substrate (*e.g.*, a silicon wafer with a $SiO_2$ isolation layer for electronics and optoelectronics applications). Thus, an additional transfer step is required to place graphene on the desired material.

As depicted in Figure 2.1, graphene transfer commonly involves deposition of a sacrificial polymer film (*e.g.*, poly(methyl methacrylate)) followed by mechanical or chemical etching of the underlying metal. The graphene is then transferred to the target substrate and the polymer layer is removed. This additional processing leads to wrinkles, polymer residues, and breakage; hence, many efforts have been made to mitigate this step or provide alternative transfer mechanisms. Despite these improvements, defects are still inevitable when a transfer step is involved. An ideal solution would be to eliminate the transfer step entirely.

### 2.1.2 Status of transfer-free methods

Several groups have reported the possibility of transfer-free growth of graphene using sacrificial metal-assisted CVD [43]. In many of these cases, as depicted in Figure 2.2, a solid carbon layer (*e.g.*, self-assembled monolayer, polymer film, amorphous carbon) is used as a precursor in the presence of a metal catalyst or metal silicide. Upon annealing, carbon dissolves in the metal capping layer and upon cooling, it segregates to the substrate interface and graphene is formed directly on the substrate of interest, successfully eliminating the transfer step altogether.

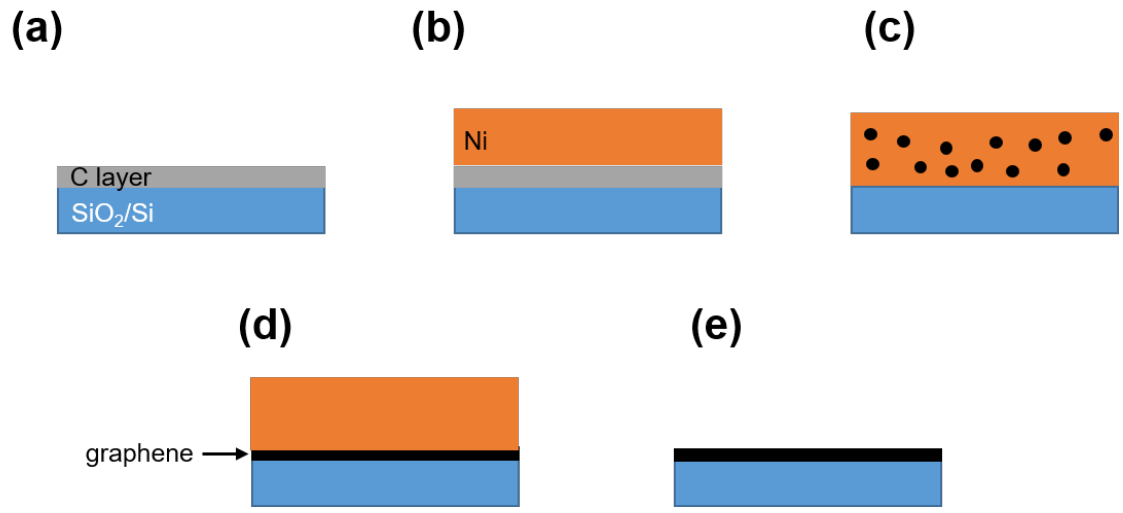


Figure 2.2: Schematics of transfer-free graphene growth with solid carbon source. (a) Carbon layer deposition, (b) Ni deposition, (c) high-temperature annealing (C diffusion), (d) graphene segregation and precipitation, (e) Ni layer removal.

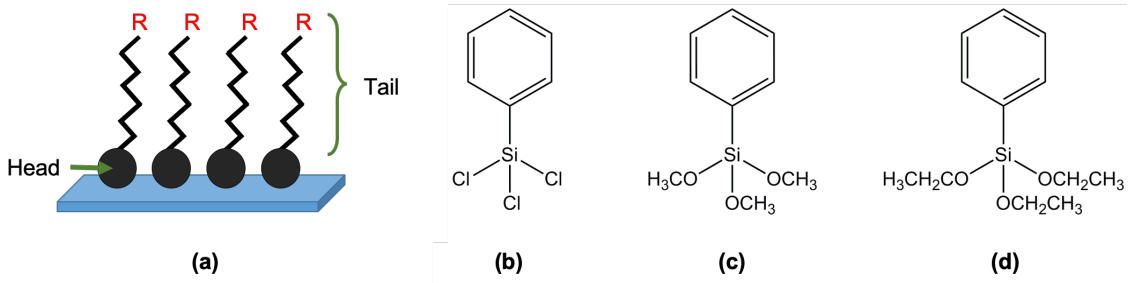


Figure 2.3: (a) Generic self-assembled monolayer structure. Representative SAM precursors (b) trichlorophenylsilane, (c) trimethoxyphenylsilane, and (d) triethoxyphenylsilane.

### Self-assembled monolayers

Self-assembled monolayers (SAMs) are organic molecules that spontaneously chemisorb on surfaces in an ordered fashion [44–46]. As represented in Figure 2.3a, these molecules are composed of a "head group" that forms stable covalent bonds on a lower-free-energy surface, and a "tail group" consisting of a molecular chain with a terminal functional group.

For graphene synthesis, SAMs with terminal phenyl groups are promising precursors because such tails act as structural analogues that may facilitate molecular rearrangement during graphene formation. Example molecular structures of phenyl-based SAMs are shown in Figure 2.3b-d. To date, various SAMs of related forms have been demonstrated as possible precursors for graphene growth [47–49].

### Carbonaceous polymers and amorphous carbon

Polymers have also received some attention as a precursor for transfer-free graphene growth. Example polymers that have been explored include polystyrene, PAN, and PMMA, PPMS, and ABS with a nickel capping layer [50–52]. Sputtered silicon carbide or carbon layers with nickel catalysts have also been studied [53, 54]. Copper capping layers have appeared as well [55].

### Gaseous precursor

Despite the promising results obtained from research on solid carbon-based precursors, it cannot be ignored that the carbon layer requirement creates additional process steps and complexities that could be avoided using a simple gaseous precursor. In addition, a gaseous inlet flow enables uniform access of feedstock molecules to the catalyst surface.

Indeed, recent papers have shown the viability of methane and ethylene gases for metal-catalyzed, transfer-free fabrication of graphene on insulating substrates. While these studies provide promising alternatives to transfer, the graphene domain sizes are small or the layer numbers are not controllable.

In this work, we report the direct growth of graphene on $SiO_2$ by metal-assisted low-pressure thermal CVD, with a specific focus on copper and nickel as reaction catalysts. We consider the mechanism that supports these results and discuss several considerations that are often overlooked in results reported in literature. This study opens avenues to achieve wafer-scale and transfer-free graphene on $SiO_2$ substrates, leading to the more practical applications of graphene in next-generation semiconductor devices.

## 2.2 Nickel-induced graphitization with gaseous methane

### 2.2.1 Process development

Improved transfer-free graphene synthesis hinges upon finding the optimized parameter space in light of various tradeoffs. For this particular work, two references are cited as the starting bases for further improvement. In Reina *et al.*, CVD graphene growth on top of the metal catalyst (henceforth referred to as top-layer graphene) is systematically studied with a focus on precursor concentration and cooling rate [56]. In McNerny *et al.*, CVD graphene growth below the metal catalyst (henceforth referred to as bottom-layer graphene) is rigorously reported with analysis about microstructure and effect of parameters on the resulting films [57].

#### Previous experimental work

Although the work by Reina *et al.* examines only top-layer graphene films, the process choices and analysis are equally relevant for bottom-layer graphene growth, particularly given the diffusion and solubility time scales discussed earlier. Figure 2.5 illustrates the temperature profile used to produce 1–2 layer graphene on Ni films on $SiO_2$. In this process, there are three regimes of interest: (1) the initial heating and annealing step in the presence of a carrier gas, which facilitates Ni grain growth and surface smoothing, (2) methane introduction, when carbon enters the system, and (3) substrate cooling, when carbon precipitation and graphene formation occur. For higher $CH_4$ concentrations (*i.e.*, $> 0.7$ %), the grain size of Ni is found to be a critical determinant of graphene coverage; in contrast, the cooling rate does not have a strong impact on the size of 1–2L graphene formed.

Similarly, McNerny *et al.* study the formation of Ni-assisted CVD graphene [57]. In this case, ethylene is used as the precursor carbon source, and stress-induced delamina-

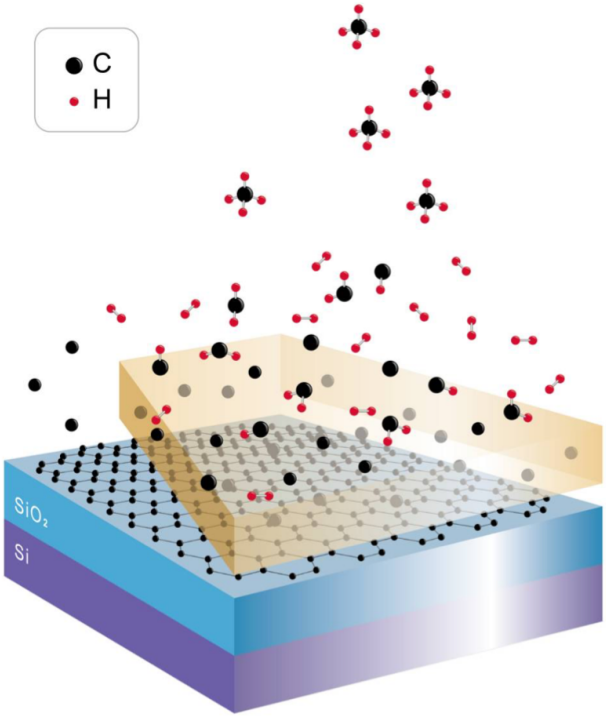


Figure 2.4: Schematic of metal-catalyzed, transfer-free CVD graphene growth with gaseous methane precursor.

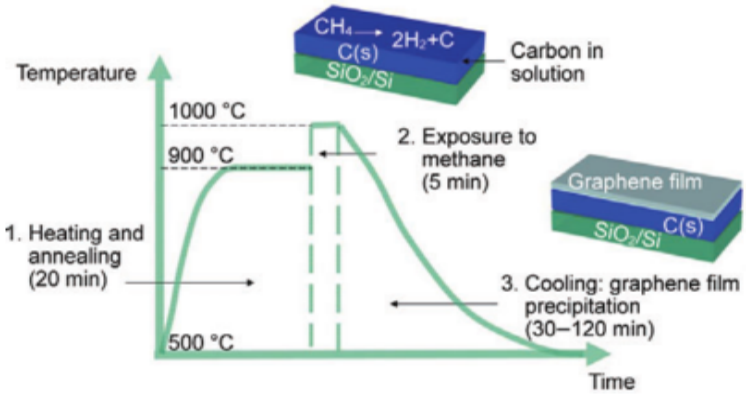


Figure 2.5: Schematic of annealing profile and graphene growth from Ref. [56].

tion of Ni is used to mechanically exfoliate the metal from the system. The annealing profile is given in Fig. 2.6. Notably, this profile has a longer annealing time (5 minutes) than growth time (2 minutes) and the overall process temperature is between 800–900 °C. Again, the initial annealing is said to increase the grain size of the initial Ni films.

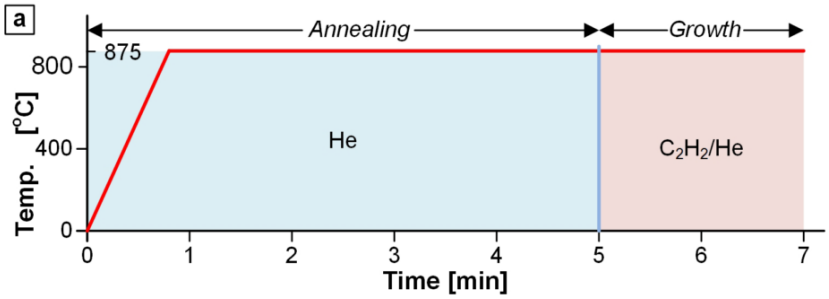


Figure 2.6: Temperature profile for CVD graphene growth from Ref. [57].

**Theoretical analysis**

The solubility of carbon in catalyst metals dictates the equilibrium formation of graphene. Indeed, the nickel-carbon phase diagram (Figure 2.7) is often cited as a notable determining factor to the ultimate quality and thickness of CVD graphene [14, 18, 26, 40–42]. For nickel, this solubility was studied extensively by Baraton, *et al.* by induced ion implantation of carbon [58]. Graphene growth in nickel occurs in two overarching stages: (1) carbon is dissolved into the metal at high temperatures (700–1000 °C and (2) carbon atoms are "crystallized" to form graphene via equilibrium surface segregation and precipitation owing to saturation of the solid solution. Equilibrium surface segregation is a result of compositional heterogeneity and manifests itself as free energy minimization of an undersaturated solution. Precipitation refers to the transition point of classical phase separation, with the corresponding solubility $S_P$.

As depicted in the phase diagram in Fig. 2.8, after annealing, cooling carbon first crystallizes as graphene on the Ni surface and then undergoes bulk precipitation. Baraton *et al.* offer an expression for solubility given by

$$S_P = S_{P_0} e^{H_P/kT} \tag{2.1}$$

where $S_P$ is the solubility, $S_{P0}$ is the entropic pre-factor related to the density of solute sites, $H_P$ is the heat of precipitation, and $k$ is Boltzmann's constant. Using $S_{P0} = 5.33 \times 10^{22}$ atoms cm$^{-3}$ and $H_P = -0.47$ eV [58, 60],the temperature above which carbon is completely soluble in Ni is $T_S \sim 1046$ °C.

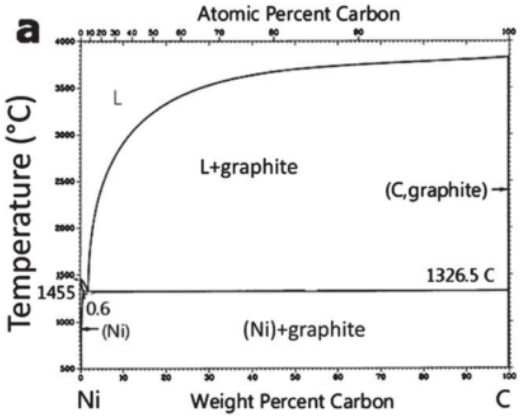


Figure 2.7: Nickel-carbon phase diagram from Ref. [59].

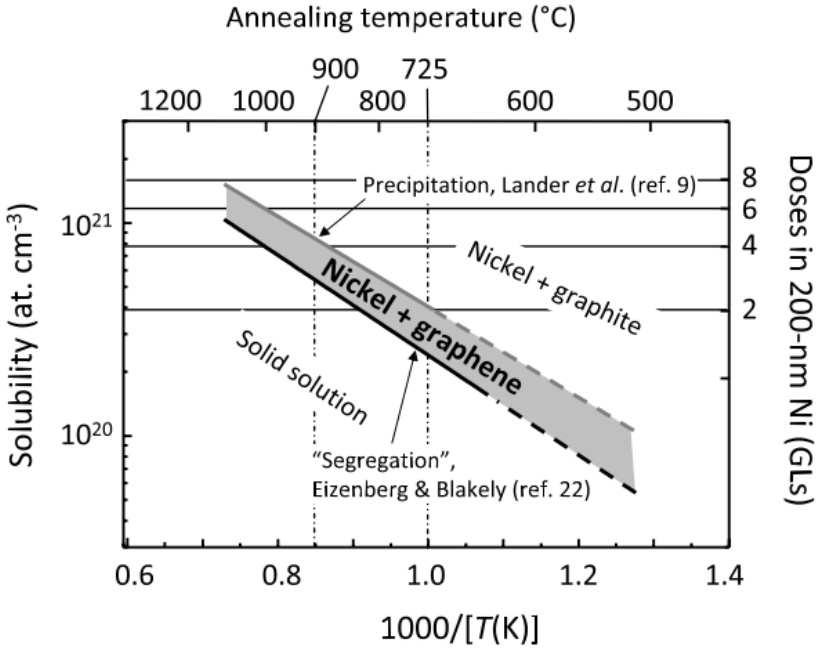


Figure 2.8: Carbon solubility in nickel based on various reference correlations, Ref. [58].

### Adapted experimental design

Adapted based on these references [56, 57], a two-step heating process was used and further optimized. Briefly, nickel was evaporated on silicon (100) substrates with a thermally-grown $SiO_2$ and heated in a quartz-tube furnace in a two-step process employing $CH_4$ precursor.

### Substrate preparation

P-type Si(100) substrates with 300 nm wet thermal oxide (University Wafer) were cleaned in acetone and isopropanol prior to use. Nickel films (100 nm) were deposited using electron-beam evaporation (Thermionics VE-700) of nickel pellets ()99.995%). Samples were cleaved into 1 cm $\times$ 1 cm pieces, loaded into a hot-wall chemical vapor deposition reactor (Lindberg/Blue M), and pumped to a background pressure of $\sim$10 mTorr.

Silicon dioxide thickness of 300 nm was chosen to avoid metal silicide formation during the high temperature synthesis processes, as noted previously [53, 61], and to enable optical detection of graphene (due to the layer-specific optical contrast of graphene on $SiO_2$) [62]. Nickel thickness was chosen considering the tradeoffs between metal dewetting and graphene viability based on previous studies [53]—*i.e.*, optimized for the minimum thickness needed to grow graphene without significant metal dewetting.

### Chemical vapor deposition

Annealing temperatures were selected to be the minimum temperatures that result in graphene without marked metal dewetting during annealing. Process pressures were limited by the pump speed for the given gas flow rates. In the first step, the furnace temperature was raised to 800 °C (ramp rate $\sim$40 °C/min) and held for 10 minutes under 200 sccm Ar (Praxair, 99.999%) to facilitate grain growth of the polycrystalline metal and smooth the metal surface, as suggested in previous literature [56, 57]. The temperature was then raised to 1000 °C within 2 minutes and introduced to 60 sccm $CH_4$ (Praxair, 99.97%) and 40 sccm $H_2$ (Praxair, 99.999%) for 150 seconds. This was done to facilitate graphene nucleation and growth both on top of and underneath the metal layer.

The gases were then turned off, the furnace heater was switched off, and the sample was cooled down at P $\sim$ 10 mTorr. A range of cooling rates were tested; the natural cooling rate of the furnace ($\sim$20 °C/min) resulted in bottom-layer graphene with highest efficacy. Finally, the samples were removed and treated with mild $O_2$ plasma (RF plasma, 20W, 200 mTorr, 10 minutes) to remove top-layer graphene. The nickel was etched using a $HNO_3$:$CH_3COOH$:$H_2SO_4$ (5:5:2) solution to obtain bottom-layer graphene.

### 2.2.2 Graphene characterization

#### Optical microscopy

Figure 2.9 shows the optical images for representative samples of bottom-layer graphene using a nickel catalyst (Leica DM4000 Microscope). The surface is mottled with features of $< 5$ $\mu$m size, indicating variation in the morphology and thickness throughout the sample due to the layer-specific optical contrast of graphene on 300 nm $SiO_2$ [62].

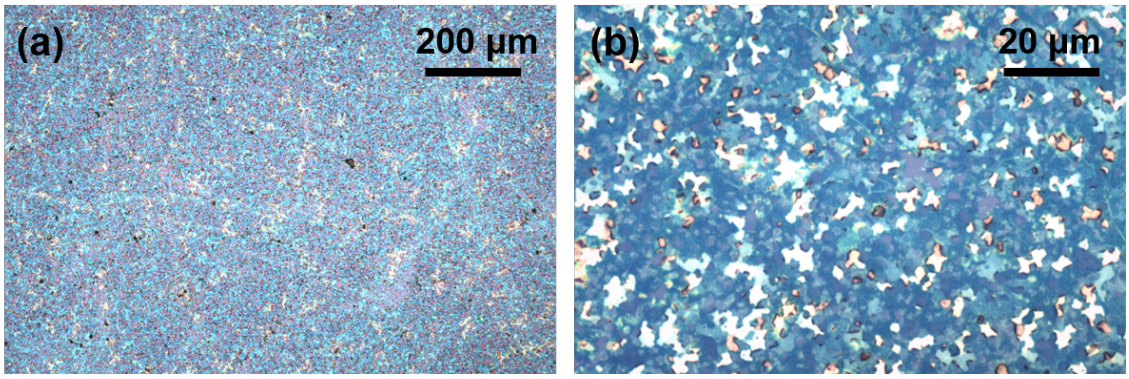


Figure 2.9: Optical microscopy of bottom-layer Ni-catalyzed CVD graphene annealed to 1000 °C in the presence of $CH_4$, (a) 10x magnification, (b) 100x magnification.

#### Raman spectroscopy

Raman spectroscopy can be used to assess the quality and thickness of a given graphene film [63–65]. Specifically, graphene exhibits characteristic Raman peaks often denoted D ($\approx$ 1350 cm$^{-1}$), G ($\approx$ 1600 cm$^{-1}$), and 2D ($\approx$ 2700 cm$^{-1}$) [63]. The ratio of the 2D and G peaks ($I_{2D}/I_G$) and the full width at half maximum (FWHM) of the 2D peak can be used to determine layer number, with $I_{2D}/I_G > 1$ and FWHM $< 30$ cm$^{-1}$ representing single-layer graphene and $I_{2D}/I_G < 0.7$ and FWHM $> 70$ cm$^{-1}$ representing 3 or more layers of graphene [56, 65]. In addition, the intensity of the D peak, which is related to the boundaries and edge states of graphene, can be an indicator of graphene quality; *i.e.*, a large D peak suggests a defective graphene film.

After CVD growth as described previously (Section 2.2.1), graphene is formed both on top the nickel catalyst and below the nickel catalyst (accessible after nickel removal by wet etch or mechanical exfoliation). Figure 2.10 shows the Raman spectra for representative top-layer graphene (a) and bottom-layer graphene by exfoliation (b). We note that the efficacy of mechanical exfoliation is imperfect and can result in spurious layer thickness results as shown in Figure 2.10b, similar to what has been shown previously by Su *et al.* [66]. Because the mechanism (*i.e.* carbon kinetics and transport) of top-layer

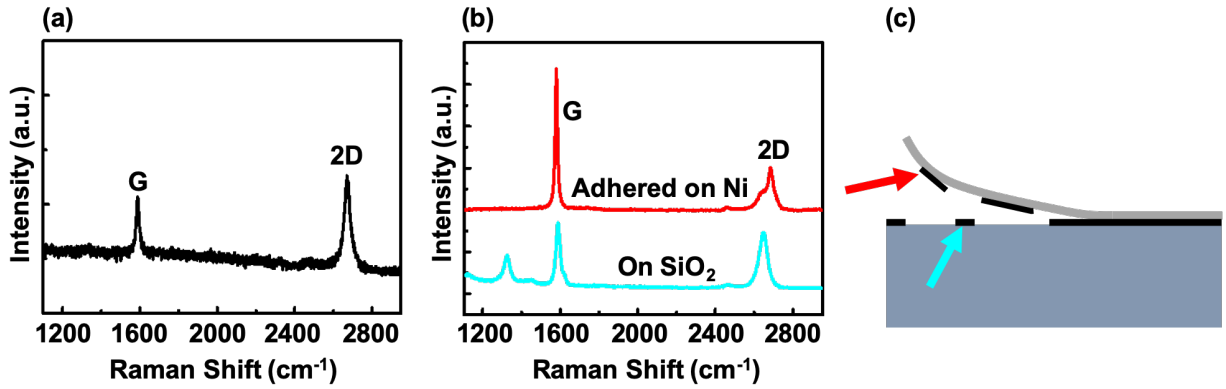


Figure 2.10: Raman spectra for (a) top-layer CVD graphene and (b) bottom-layer CVD graphene adhered on Ni (red) and on $SiO_2$ (cyan). (c) Schematic of exfoliated nickel-catalyzed bottom-layer graphene resulting in the two distinct spectra shown in (b).

and bottom-layer graphene are inherently different, the final graphene characteristics are often expectedly dissimilar. Keeping in line with the original motivation of developing a method of transfer-free growth on $SiO_2$, the following results explore in particular bottom-layer graphene.

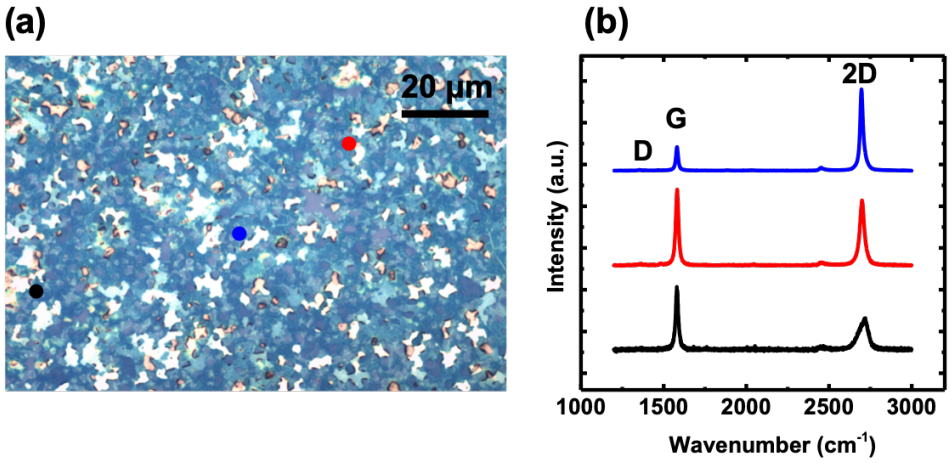


Figure 2.11: Raman spectra for three representative locations on bottom-layer nickel-catalyzed CVD graphene on $SiO_2$, using an 800 °C Ar ramp and 1000 °C $CH_4/H_2$ anneal followed by $O_2$ plasma and $HNO_3$:$CH_3COOH$:$H_2SO_4$ etch as described in Section 2.2.1.

In Figure 2.11, representative Raman spectra for nickel-catalyzed CVD graphene (confocal Raman spectroscopy, Horiba LabRam ARAMIS, 532 nm excitation, 100× objec-

tive) show a marked variation in $I_{2D}/I_G$ ratio across the region, indicating the presence of nonuniform layer thickness throughout the surface. However, the weak D peak—which arises from disorder in the $sp^2$ carbon atoms in graphene rings [63, 64]—suggests that the graphene is high quality, irrespective of its layer number. Lower-wavenumber regions of the Raman spectra (not shown) do not show characteristic nickel silicide peaks (100, 140, 199, 217, 250, 400 $cm^{-1}$ [67–69]), confirming that no chemical reaction has occurred between the catalyst and substrate during annealing.

Two-dimensional Raman mapping is used to investigate the uniformity of graphene across the surface. Large-area Raman mapping (1 $\mu$m step size) shows full coverage of graphene over the substrate, based on the presence of characteristic graphene peaks at each sampling point over a 20 $\mu m$ × 20 $\mu m$ region (representative of the 1 cm × 1 cm sample, limited only by the tube furnace dimensions). For nickel-catalyzed bottom-layer graphene (Figures 2.12a-b), there is a wide $I_{2D}/I_G$ distribution from 0.1 to 5.3, with monolayer ($I_{2D}/I_G > 1$) graphene coverage greater than 45%. Higher-resolution (0.3 $\mu$m step size) Raman mapping of this monolayer region (Figure 2.12c) reveals an average $I_{2D}/I_G$ peak intensity ratio of 1.8 ± 0.37 and average $I_D/I_G$ peak ratio of 0.14, indicating high-quality monolayer graphene over the 7.5 $\mu m^2$ domain. Accordingly, the monolayer graphene exhibits high coverage and low defects, among the highest quality of all transfer-free nickel-catalyzed graphene grown via thermal CVD to our knowledge [27, 43].

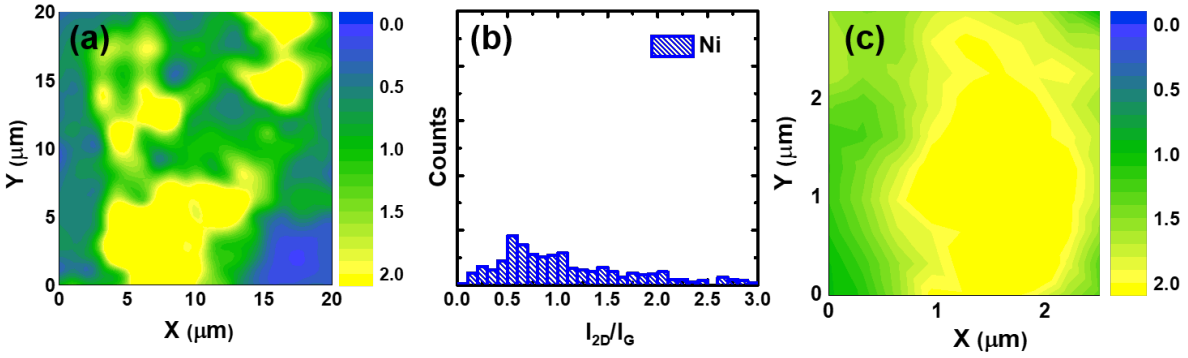


Figure 2.12: Raman mapping data of bottom-layer metal-catalyzed CVD graphene on $SiO_2$, using an 800 °C Ar ramp and 1000 °C $CH_4/H_2$ anneal followed by $O_2$ plasma and $HNO_3$:$CH_3COOH$:$H_2SO_4$ etch as described in Section 2.2.1. (a) Large-area $I_{2D}/I_G$ Raman map for Ni-catalyzed graphene, (b) histogram of Iarge-area $_{2D}/I_G$ map for Ni-catalyzed graphene, (c) small-area $I_{2D}/I_G$ Raman map for Ni-catalyzed graphene

**Hall probe measurement**

For semiconductor devices, mobility is a key parameter for gauging and comparing device performance. Therefore, Hall measurements based on the Van der Pauw method (Ecopia HMS-5000, In contacts, magnetic field 0.55 T) were conducted at room temperature (Figure 2.13). The current-voltage characteristics for both showed a linear dependence, indicating ohmic behavior of the graphene film. Nickel-catalyzed bottom-layer graphene yielded a resistivity of 2.7 m$\Omega$·cm and average mobility of 352 cm$^2$/V·s, on par with the mobilities reported to date for direct graphene on dielectric substrates [27]. Note that tool dimensions limited the measurements to entire centimeter-scale samples; higher mobility values would be expected for smaller-area measurements on the high-quality domains as characterized by Raman spectroscopy. Further work on post-synthesis defect engineering of these films could increase mobility values closer to the theoretical limit.

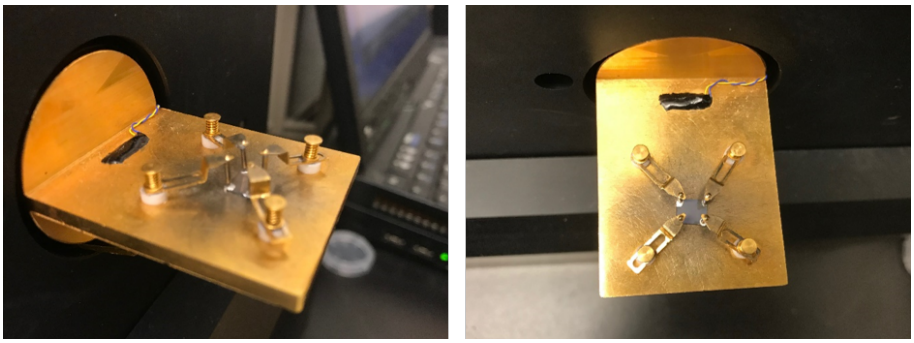

Figure 2.13: Hall-effect measurement setup. (a) Side view (b) top view

## 2.3 Copper-induced graphitization with gaseous methane

Process specifications still hindering widespread incorporation of graphene in consumer electronics include (1) large-scale production (2) high-quality films, and (3) wafer-scale uniformity. Section 2.2 addressed the non-ideal transfer step by optimizing a nickel-catalyzed transfer-free approach. This method proved to be feasible and the graphene films were high-quality, but the final graphene formed was patchy. This is a significant deterrent for electronics devices, which typically require conformal films for the best performance. As such, it is important to find an alternative method that can provide more uniform graphene growth.

### 2.3.1 Process development

#### Previous work

Beyond nickel, copper is the next most-commonly-explored catalyst for graphene synthesis. Although there are many differences between nickel and copper, carbon solubility and diffusion constants are often cited as the key factors to layer-number variations [14]. Several works have explored transfer-free growth of graphene using copper as the catalyst choice.

Su *et al.* were among the first to expound upon a transfer-free copper-assisted graphitization process with emphasis on top-layer graphene [66]. Wafer-size bilayer/few-layer graphene is grown on $SiO_2$ and quartz substrates capped with 300 nm copper, with methane as the carbon precursor. Using a 900 °C annealing temperature—lower than typical in order to minimize $SiO_2$ quality degradation—the methane dissociates to yield carbon, which reportedly diffuses through copper grain boundaries to the copper-insulator interface. In addition, the growth pressure is higher than typical ($>$ 800 mtorr) in order to avoid rapid evaporation or dewetting of copper. The copper thickness is found to be important as well: when Cu is too thin, dewetting can occur, but when Cu is too thick, there is poor continuity of bottom-layer graphene. The bottom-layer graphene is found to be consistently few-layered.

The proposed mechanism of growth is suggested in Figure 2.14. In the initial thermal annealing stage, copper grains are formed and enlarged. When $CH_4$ is introduced, the precursors dissociate at elevated temperatures—these carbon species both migrate on the surface and diffuse through grain boundaries. In the third step, graphene forms on the surface (top-layer graphene) while other carbon species continue to diffuse through grain boundaries, eventually forming bottom-layer graphene, Finally, the top-layer graphene is removed with $O_2$ plasma and Cu is wet etched with $Fe(NO_3)_3$ in order to obtain graphene directly on the insulating substrate.

Huet and Raskin studied the chemical vapor deposition of top-layer graphene on thin copper films [70]. In this work, single-layer graphene quality and size were optimized by modifying global pressures and annealing conditions. This work demonstrated the importance of having a high hydrogen-to-methane ratio and high argon atmosphere pressure in the system, as well as an evacuation step to avoid film degradation.

#### Adapted experimental design

Using these two works [66, 70] as bases for experimental design, we developed a transfer-free CVD process that incorporated some of the major takeaways from both.

P-type Si(100) substrates with 300 nm wet thermal oxide (University Wafer) were

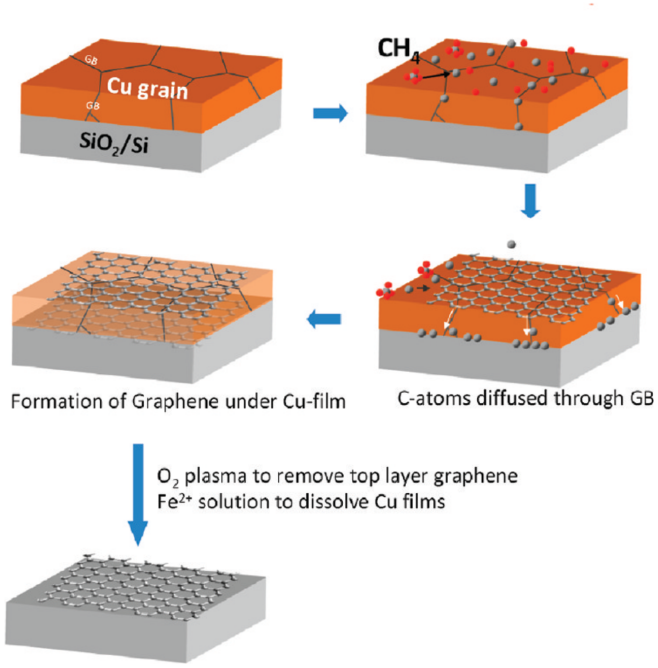


Figure 2.14: Growth schematic for transfer-free copper-assisted graphitization [66].

cleaned in acetone and isopropanol. As in the nickel-induced graphitization studies, silicon dioxide thickness of 300 nm was chosen to avoid metal silicide formation during the high temperature synthesis processes, as noted previously [53, 61], and to enable optical detection of graphene (due to the layer-specific optical contrast of graphene on $SiO_2$) [62].

Copper films (200–300 nm) were then deposited using electron-beam evaporation (Innotec ES26C) of copper pellets (99.99%). Samples were cleaved into 1 cm $\times$ 1 cm pieces, loaded into a hot-wall chemical vapor deposition reactor (Lindberg/Blue M), and pumped to a background pressure of $\sim$10 mTorr prior to annealing.

Following the lead of Su *et al.* and Reina *et al.*, a two-step annealing process was used in order maximize metal grain growth and smoothening prior to graphene growth [56, 66]. In the first step, the furnace temperature was raised to 750 °C (ramp rate $\sim$40 °C/min) in an atmosphere of 41.5 sccm hydrogen gas (Praxair, 99.999%) and 45 sccm argon gas (Praxair, 99.999%). Following grain growth, the furnace temperature was increased to $\sim$ 700–900 °C and introduced to $CH_4$ (Praxair, 99.97%) and $H_2$ (Praxair, 99.999%) for 5 minutes. The gases were then turned off and the sample was cooled down naturally (40 °C/min) at P $\sim$ 10 mTorr. Finally, the samples were removed and treated with mild $O_2$ plasma (RF plasma, 20W, 200 mTorr, 10 minutes) to remove top-layer graphene.

### 2.3.2 Graphene characterization

#### X-ray diffraction

To determine the extent of grain growth, X-ray diffraction (XRD) was performed on copper as-deposited and after two different ramp treatment times (25 minutes, 125 minutes). As shown in Figure 2.15, the primary XRD peak is the Cu (1 1 1) peak at 50.80°. This peak is notable both as-deposited and after each of the ramp variations. After wet etch removal of the copper with $Fe(NO_3)_3$, there are no more characteristic peaks visible, indicating that the copper can be effectively removed using this method.

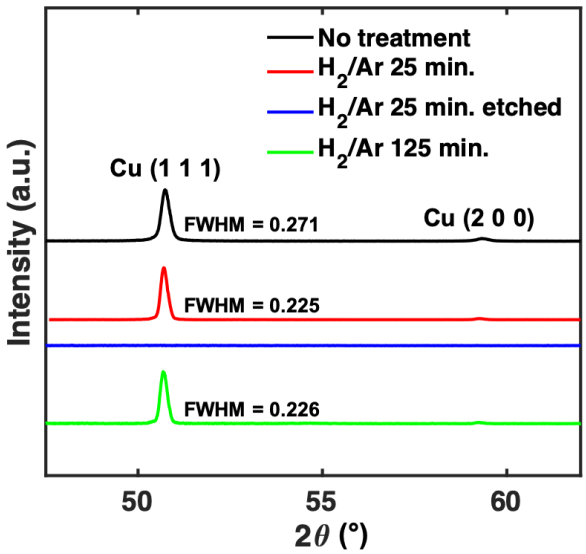


Figure 2.15: XRD patterns showing Cu (111) and (200) peaks before and after annealing treatment of as-deposited evaporated copper for various times and etching conditions.

Additional information about the grain size can be extracted from the Scherrer equation:

$$\tau = \frac{K\lambda}{\beta cos\theta} \tag{2.2}$$

where $\tau$ is the mean size of crystalline domains, $K$ is the dimensionless shape factor, $\lambda$ is the X-ray wavelength, and $\beta$ is the line broadening at half the maximum intensity —*i.e.*, the full width at half maximum (FWHM)—and $\theta$ is the Bragg angle [71, 72]. This equation suggests that grain size is inversely proportional to the FWHM. As shown in Figure 2.15, for both the 25-minute and 125-minute ramp steps, the FWHM decreases, suggesting an enlarging of grain size following both ramp conditions; however, it appears that the shorter time is sufficient to reach similar crystallinity.

### Optical microscopy

Bottom-layer graphene following optimization was characterized as previously described (Section 2.2.2). Figure 2.16 shows optical images representative of the contrasting bottom-layer graphene morphologies that can result from distinct parameter selection in temperature, pressure, and flow rates. As in the nickel-induced graphitization process, annealing temperatures were selected to be the minimum temperatures that result in graphene without marked metal dewetting during annealing. Figures 2.16a and 2.16b show contrasting patchy and conformal bottom-layer graphene morphology at 825 °C and 800 °C, respectively. Annealing temperature of 800 °C is chosen as the highest ideal temperature for annealing. Figures 2.16c and 2.16d contrast 75 torr and 2 torr annealing pressures, respectively (at 800 °C). This corresponds well with what Huet *et al.* showed for top-layer graphene on copper foils, in which a higher pressure was less ideal for continuous graphene and may have even led to higher probability of oxygen impurities in the system [70]. Figures 2.16e and 2.16f examine the effect of varying ratios of hydrogen to methane flow rates, showing ratios of 1:1 and 1:6 respectively. While nonuniform graphene is seen in Figure 2.16e for a 1:1 ratio, more continuous graphene is possible by increasing the methane flow rate (Figure 2.16f). As Huet *et al.* suggest, however, it is also important to examine the ratio in the context of global partial pressures as well [70].

### Raman spectroscopy

Raman spectroscopy was used to assess the quality and thickness of the resulting graphene films. The Raman spectra from several sample locations (indicated in Figure 2.17a)are shown in Figure 2.17b. The spectra are relatively similar (*i.e.*, have similar $I_{2D}/I_G$ ratios) across the region, suggesting uniformity in thickness and coverage in the copper-catalyzed CVD graphene. The notable D peak (*i.e.*, $I_D/I_G \sim 0.6$–$0.8$) indicates the presence of significant degree of defects in this film, likely due to the low process temperature (800 °C) required to minimize copper dewetting during growth. In addition, gaseous $H_2$ has been shown to increase defects in CVD graphene on copper while simultaneously smoothening the Cu surface, further illustrating the trade-off considerations needed in CVD graphene growth [73].

Tables 2.1 and 2.2 show a subset of the experimental conditions and their results in further detail. "Graphene Peaks" is short for the existence of detectable Raman spectroscopy peaks at wavenumbers of $\approx 1350$ cm$^{-1}$, $\approx 1600$ cm$^{-1}$, and $\approx 2700$ cm$^{-1}$, denoted "Yes" (all peaks exist), "No" (no peaks exist), or "amorphous C" (only the latter two peaks with wide FWHMs are detected). As mentioned previously, the starting basis for these adjustments was derived from Su *et al.* (note that flow rates had to be modified in order to accommodate for allowable conditions in the reactor of choice). With this

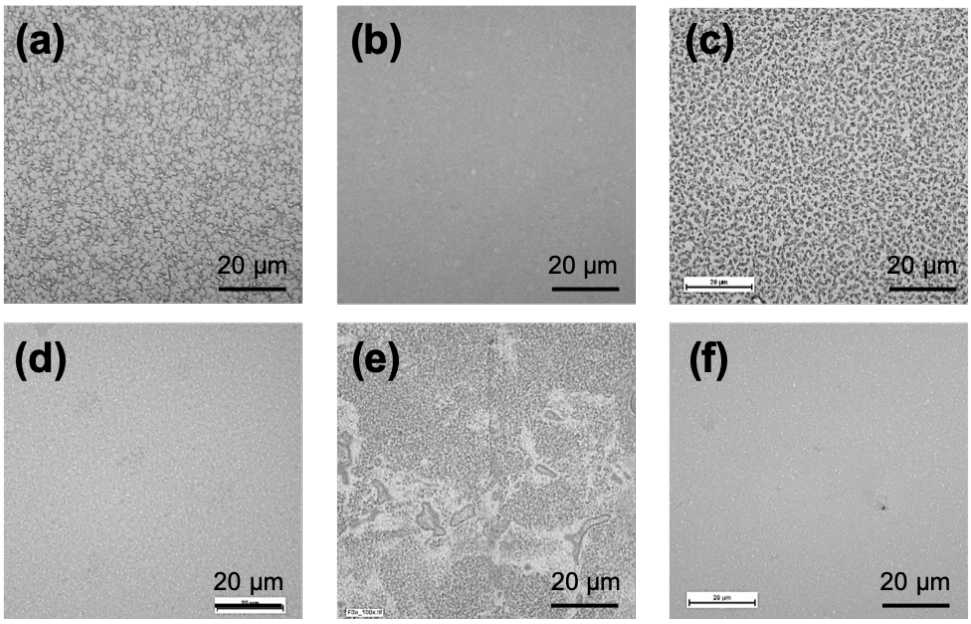


Figure 2.16: Optical images of bottom-layer graphene after CVD growth showing contrasting morphologies for different process conditions. (a) 825 °C annealing, (b) 800 °C annealing, (c) 75 torr, (d) 2 torr, (e) 1:1 $H_2$:$CH_4$, (f) 1:6 $H_2$:$CH_4$.

.

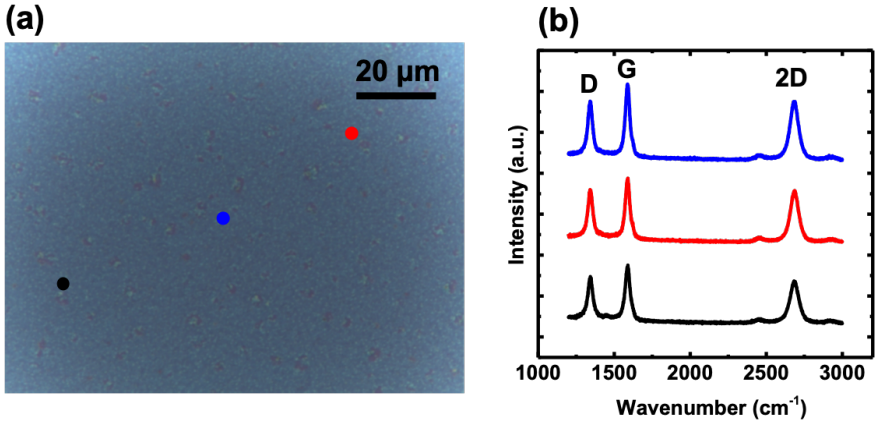


Figure 2.17: Raman spectroscopy data for copper-catalyzed bottom-layer graphene after 800 °C CVD annealing process and wet etch as outlined in Section 2.3.1.

foundation, adaptations were made in the ramp conditions and annealing conditions (*e.g.*, flow rates, temperature, time). Other experiments performed—including varying the oxygen plasma etch time, cleaning treatment procedure, and cooling rate—are not shown in these tables either due to lack of correlation or lack of clear trends.

Table 2.1: Summary of select LPCVD ramp and annealing parameters and resulting top-layer and bottom-layer graphene outcomes, as characterized by Raman spectroscopy (Yes/No identifying peaks at $\approx 1350$ cm$^{-1}$, $\approx 1600$ cm$^{-1}$, and $\approx 2700$ cm$^{-1}$).

| $H_2$/Ar Ramp Conditions | $CH_4$/$H_2$ Anneal Conditions | Graphene Peaks Before Etch | Graphene Peaks After Etch |
|---|---|---|---|
| 415 sccm $H_2$<br>450 sccm Ar<br>750 °C, 25 min. | 75 sccm $CH_4$<br>15 sccm $H_2$<br>900 °C, 5 min. | Yes [66] | Yes [66] |
| 41.5 sccm $H_2$<br>45 sccm Ar<br>750 °C, 25 min. | 75 sccm $CH_4$<br>15 sccm $H_2$<br>900 °C, 5 min. | Yes<br>(poor<br>uniformity) | Yes<br>(poor<br>uniformity) |
| 83 sccm $H_2$<br>90 sccm Ar<br>750 °C, 125 min. | 75 sccm $CH_4$<br>15 sccm $H_2$<br>900 °C, 5 min. | No<br>(poor<br>uniformity) | No<br>(poor<br>uniformity) |
| 41.5 sccm $H_2$<br>45 sccm Ar<br>750 °C, 25 min. | 75 sccm $CH_4$<br>15 sccm $H_2$<br>900 °C, 10 min. | Amorphous C | Amorphous C |
| 41.5 sccm $H_2$<br>45 sccm Ar<br>750 °C, 25 min. | 75 sccm $CH_4$<br>15 sccm $H_2$<br>900 °C, 20 min. | No | Yes<br>(poor<br>uniformity) |
| 41.5 sccm $H_2$<br>45 sccm Ar<br>750 °C, 25 min. | 75 sccm CH4<br>15 sccm $H_2$<br>800 °C, 5 min. | Yes | Yes |
| 41.5 sccm $H_2$<br>45 sccm Ar<br>750 °C, 25 min. | 75 sccm CH4<br>15 sccm $H_2$<br>800 °C, 10 min. | No | Yes<br>(poor<br>uniformity) |

Table 2.2: Additional summary of select LPCVD ramp and annealing parameters and resulting top-layer and bottom-layer graphene outcomes, as characterized by Raman spectroscopy (Yes/No identifying peaks at $\approx 1350\,\mathrm{cm}^{-1}$, $\approx 1600\,\mathrm{cm}^{-1}$, and $\approx 2700\,\mathrm{cm}^{-1}$).

| $H_2$/Ar Ramp Conditions | $CH_4/H_2$ Anneal Conditions | Graphene Peaks Before Etch | Graphene Peaks After Etch |
|---|---|---|---|
| 41.5 sccm $H_2$<br>45 sccm Ar<br>750 °C, 25 min. | 75 sccm CH4<br>15 sccm $H_2$<br>800 °C, 5 min. | Yes | Yes |
| 41.5 sccm $H_2$<br>45 sccm Ar<br>750 °C, 25 min. | 75 sccm CH4<br>15 sccm $H_2$<br>825 °C, 5 min. | Yes | Yes |
| 41.5 sccm $H_2$<br>45 sccm Ar<br>750 °C, 25 min. | 75 sccm CH4<br>15 sccm $H_2$<br>850 °C, 5 min. | Amorphous C | Yes |
| 41.5 sccm $H_2$<br>45 sccm Ar<br>750 °C, 25 min. | 75 sccm CH4<br>15 sccm $H_2$<br>875 °C, 5 min. | Amorphous C | Amorphous C |
| 41.5 sccm $H_2$<br>45 sccm Ar<br>750 °C, 25 min. | 45 sccm CH4<br>9 sccm $H_2$<br>800 °C, 5 min. | Yes | No |
| 41.5 sccm $H_2$<br>45 sccm Ar<br>750 °C, 25 min. | 8.5 sccm CH4<br>15 sccm $H_2$<br>800 °C, 5 min. | Amorphous C | Yes |

Raman spectroscopy was also used to evaluate the etching methodology and efficacy. Figure 2.18a shows representative Raman spectra of top-layer amorphous carbon after CVD annealing (black) and after $O_2$ plasma etching (red). The copper was etched using a $Fe(NO_3)_3$ solution to obtain bottom-layer graphene. As Figure 2.18b shows, both $FeCl_3$ and $Fe(NO_3)_3$ can effectively remove the copper such that the Si peak at 520 $cm^{-1}$ reappears, signifying that Si is once again accessible and "visible" without the copper capping layer.

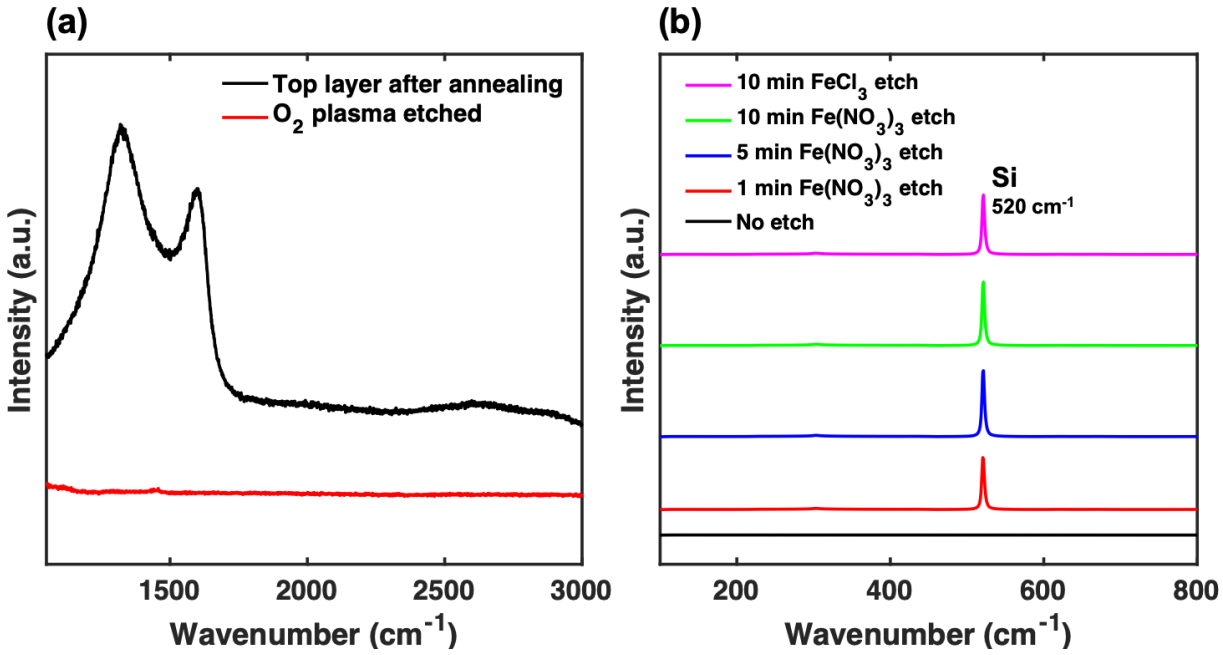


Figure 2.18: (a) Raman spectra of top-layer carbon before and after $O_2$ plasma treatment, (b) Raman spectra of 800 °C CVD-annealed 300 nm Cu on 300 nm $SiO_2$ on Si before and after etching with $FeCl_3$ or $Fe(NO_3)_3$ for 1–10 minutes, with appearance of 520 $cm^{-1}$ Si suggesting effective etch of Cu.

### Raman mapping

Two-dimensional Raman mapping was used to investigate the uniformity of graphene across the surface. Large-area Raman mapping of a 20 $\mu m \times$ 20 $\mu m$ region of bottom-layer copper-catalyzed CVD graphene is shown in Figure 2.19a. Taking a histogram of this map (Figure 2.19b) shows a much narrower $I_{2D}/I_G$ distribution (0.65 to 1.1) that confirms thickness uniformity over the large area. The higher-resolution Raman map in Figure 2.19c yields an average $I_{2D}/I_G$ peak intensity ratio of 0.97 ± 0.11 and aver-

age $I_D/I_G$ peak ratio of 0.98, indicating defective but uniform bilayer graphene. To our knowledge, this bilayer graphene shows the best uniformity in all transfer-free thermal CVD-grown copper-catalyzed graphene to date [27, 43].

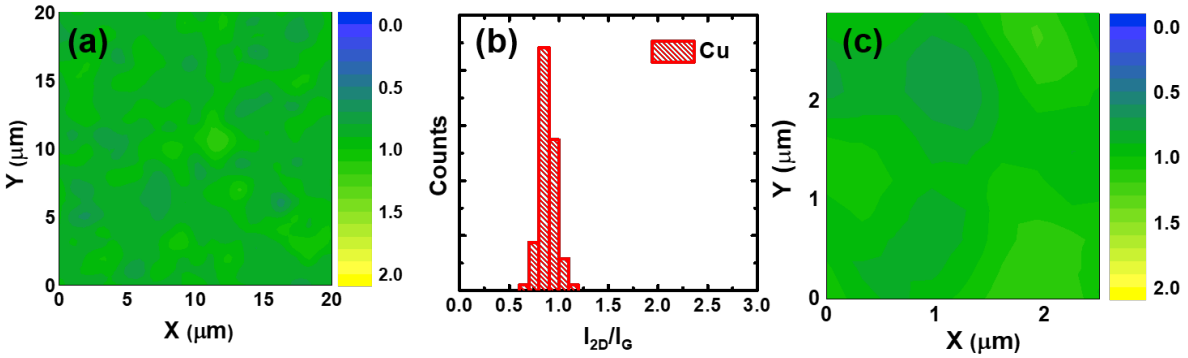


Figure 2.19: Raman mapping data of bottom-layer copper-catalyzed graphene on $SiO_2$ from optimized transfer-free CVD process (750 °C ramp in $H_2$ and Ar, 800 °C anneal in $CH_4$ and $H_2$, $O_2$ plasma and $Fe(NO_3)_3$ etch). (a) Large-area $I_{2D}/I_G$ Raman map for Cu-catalyzed graphene, (b) histogram of large-area $I_{2D}/I_G$ map for Cu-catalyzed graphene, (c) small-area $I_{2D}/I_G$ Raman map for Cu-catalyzed graphene.

### X-ray photoelectron spectroscopy

To evaluate the efficacy of copper etch, X-ray photoemission spectroscopy (XPS) was performed on the final bottom-layer graphene after $O_2$ etch and wet $Fe(NO_3)_3$ etch. Figure 2.20 shows the C 1s, Cu 2p, and O 1s peaks, all of which have measurable peaks intensities. Despite the wet etch, it appears that some Cu still exists on the surface; however, we note that the relative intensity (and therefore the relative composition, after taking into account elemental sensitivity factors) is much lower than that of the C 1s and O 1s peaks.

Hall probe measurements were done as previously described using the Van der Pauw method at room temperature (Section 2.2.2). The current-voltage characteristics showed a linear dependence, indicating ohmic behavior of the graphene film. Copper-catalyzed bottom-layer graphene had a resistivity of 3.3 mΩ·cm and average mobility of 124 $cm^2/V{\cdot}s$. This mobility value is on the lower end of the values reported in the literature for transfer-free graphene and corroborates the large $I_D$ Raman defect peak as noted previously. Further work on post-synthesis defect engineering of these films could increase mobility values closer to the theoretical limit.

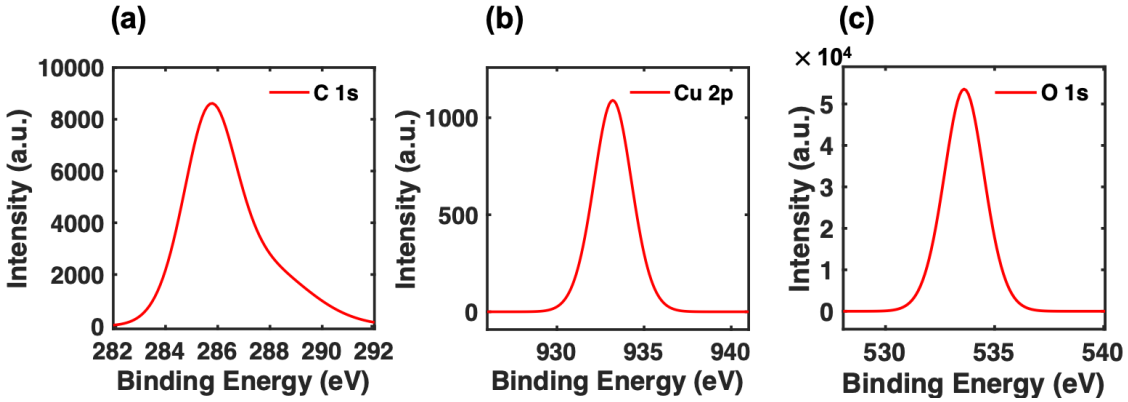


Figure 2.20: XPS characterization of bottom-layer copper-catalyzed graphene on $SiO_2$ from optimized transfer-free CVD process (750 °C ramp in $H_2$ and Ar, 800 °C anneal in $CH_4$ and $H_2$, $O_2$ plasma and $Fe(NO_3)_3$ etch).

## 2.4 Mechanistic understanding

At this time, the mechanism of bottom-layer graphene formation is still not fully understood in the literature. However, a general schematic of direct graphene growth on $SiO_2$ substrates can provide insight about the difference in uniformity between nickel- and copper-catalyzed graphene. Figure 2.21a illustrates a simplification of the metal-catalyzed graphitization process.

At the initial exposure time t = 0, methane and hydrogen gas are flowed across the metal catalyst, introducing carbon and hydrogen to the system. At high temperatures, hydrocarbons dissociate into various $CH_i$ species (i = 0, 1, 2, 3) with different relative populations depending on the catalyst metal and reaction conditions [74, 75]. This impinging dissociated carbon flux contributes to two distinct processes: (1) top-layer graphene growth and (2) carbon diffusion into the catalyst, as previously described in growth models for graphene CVD on transition metal catalysts [76, 77].

For bottom-layer graphene formation, carbon diffusion through the metal catalyst is the critical concern. Fick's second law can be used to describe the time-dependency of diffusion in the absence of chemical reaction. For the specific case of a unidirectional constant flux input $J_I$at $z = 0$, the solution of Fick's law is given by:

$$C(z,t) = \frac{2J_I}{D}\left[\left(\frac{Dt}{\pi}\right)^{1/2} e^{-\frac{z^2}{4Dt}} - \frac{z}{2}\text{erfc}\left(\frac{z}{\sqrt{4Dt}}\right)\right] \tag{2.3}$$

where $C$ is species concentration, $J_I$ is the constant source flux, $D$ is the diffusion coefficient of the species in a bulk material, $z$ is the length scale, and $t$ is diffusion time.

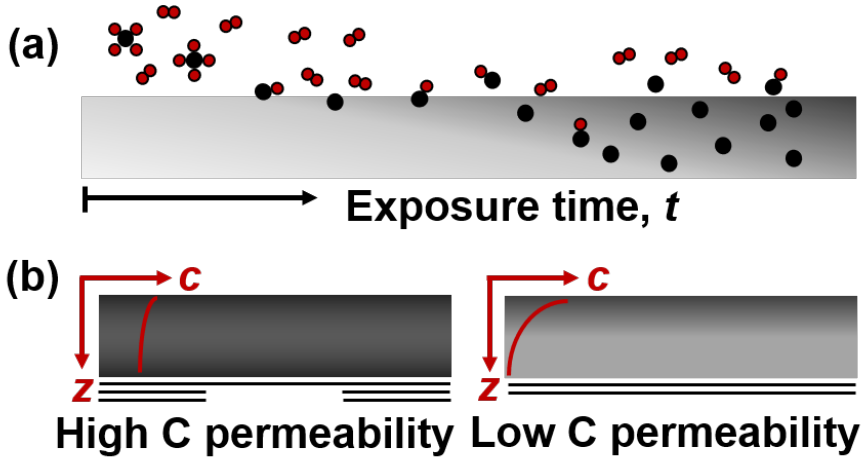


Figure 2.21: (a) Schematic of CVD hydrocarbon migration with increasing exposure time. (b) Differences in carbon migration depending on metal permeability

This characteristic has been experimentally shown to be the a good fit for carbon diffusion in nickel in the presence of methane and hydrogen gas during graphene CVD [78]. From this equation, scaling arguments can be used to estimate the approximate length scale of diffusion to be $x \sim 2(Dt)^{-1/2}$.

Given carbon diffusivities of $3 \times 10^{-11}$ $m^2/s$ at 1000 °C and $6 \times 10^{-13}$ $m^2/s$ at 800 °C in nickel and copper [60, 77], respectively, with a metal thickness of 100 nm, it would theoretically take less than 1 ms for carbon to diffuse through either metal. However, the mechanism is not quite this simple and recent kinetic growth models suggest that carbon permeability, the product of diffusivity and solubility, is the more relevant parameter to understanding carbon migration and the eventual saturation of bulk catalysts [76, 79]. It is widely known that carbon solubility in nickel (∼0.19 at% at 600 °C) [60] is several magnitudes larger than that in copper (∼0.0007 at% at 1000 °C) [80], and this fact is often used to describe the self-limiting growth of top-layer graphene on copper. However, this description is incomplete; more detailed models address how carbon migration is a strong function of kinetics in the system, beyond simple thermodynamics [76, 78, 81–83], providing deeper insight into the parameter choices that dictate graphene growth. Previous literature conjectured that for copper-catalyzed growth, bottom-layer graphene results from carbon diffusion solely through grain boundaries [66], but the striking uniformity seen in current studies (as shown earlier in Figure 3) indicates that carbon likely diffuses through the bulk as well, particularly given the long metal pre-annealing time (which enhances grain growth in the metal) and the presence of strong defects in this uniform film (which would be unexpected if graphene solely laterally extends from select nucleation sites).

Figure 2.21b illustrates the primary difference between a high-carbon-permeability metal (*e.g.*, Ni), and a low-carbon-permeability metal (*e.g.*, Cu). In a high-permeability catalyst, carbon accumulates and aggregates at the bottom interface, while a low-permeability catalyst can act as a mediating sink that can stabilize single-layer graphene growth. The contrasting graphene qualities and uniformities shown previously suggest that our growth processes act near two such regimes; these are represented by the carbon concentration profiles noted in the inset curves in Figure 2.21b. Beyond inherent thermodynamic properties, kinetic growth parameters such as precursor partial pressures and flow rates, catalyst thicknesses, exposure times, and annealing temperatures also affect the carbon saturation in the catalyst, as described extensively by Cabrero-Vilatela, *et al.* [76]. In addition, the interface energetics at the metal/$SiO_2$ interface, carbon solubility in $SiO_2$, and metal dewetting dynamics are important to address. The formation of bottom-layer graphene is highly complex and requires broader analysis beyond grain boundary diffusion or carbon penetration [66, 84]. Further studies on a quantitative model for bottom-layer graphene growth may provide deeper insight on this process.

## 2.5 Conclusion

Metal-assisted low-pressure thermal CVD is shown to be an effective method to produce large-area graphene directly on $SiO_2$. Using a two-step annealing process with optimized process parameters, we have synthesized low-defect $> 45\%$ coverage monolayer nickel-catalyzed graphene and high-uniformity $> 90\%$ coverage bilayer copper-catalyzed graphene. The final nickel- and copper-catalyzed graphene films have Hall mobilities of 352 $cm^2/V{\cdot}s$ and 124 $cm^2/V{\cdot}s$ at room temperature, respectively. These studies highlight the need for further investigations into the mechanism of transfer-free growth of graphene on insulating substrates, ultimately enabling judicious optimization of large-scale graphene-on-insulator production for beyond-silicon electronics applications.

# Chapter 3

# Spinodal dewetting of nickel on highly-oriented pyrolytic graphite (HOPG)

Despite the rapid advances in transfer-free synthesis of graphene, there are still ongoing challenges that make wafer-scale high-quality graphene unobtainable at the industrial scale. In particular, large-area uniformity is a prerequisite for electronic applications but is not yet achievable.

Previous studies showed that uniform coverage was difficult to achieve for nickel-catalyzed bottom-layer graphene. One reason for this may be due to thin film dewetting at elevated temperatures during the CVD process. Studying thin film dewetting may enable not only a deeper fundamental understanding of what is happening on the nanoscale, but also a fuller picture of why different metal catalysts (*e.g.*, Ni, Cu) result in markedly different bottom-layer CVD graphene films.

## 3.1 Introduction to thin film dewetting

Thin film dewetting—the opposite of surface wetting—is observed in everything from paint coatings to oil in a hot frying pan. In integrated circuit processing, thin films are omnipresent as catalyst layers, dielectric layers, lubricant surfaces, and coatings; dewetting of these films can create serious difficulties in achieving pristine, conformal surfaces for device components. Recent developments of new materials and devices towards the nanoscale regime further necessitate dewetting control. A fundamental understanding of metal dewetting is critical to making informed decisions about process conditions and fabrication needs, particularly for the semiconductor industry.

The results of nickel-on-HOPG spinodal dewetting, along with parallel studies

of copper-on-HOPG, are consistent with the results seen previously for low-pressure chemical vapor deposition of graphene with nickel and copper catalysts. In a broader sense, these studies provide fundamental insight on the limitations for evaluating catalyst thickness when pursuing metal-assisted graphene growth in low-pressure systems.

### 3.1.1 Interfacial energetics

When a film on a solid substrate is sufficiently thin (*i.e.*, $< 1\mu m$), its stability is no longer dictated by gravity and long-range forces but rather by intermolecular Van der Waals forces [85–87]. The behavior of such films is complex but is ultimately driven by the minimization of free energy of the system [85].

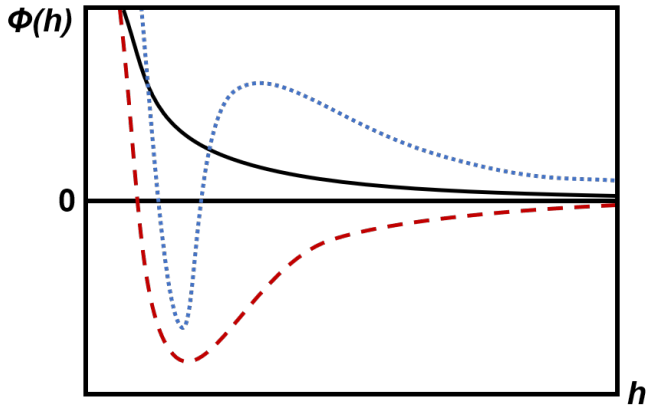


Figure 3.1: Generic effective interface potential $\phi(h)$ as a function of film thickness $h$. Curves represent the interface potential for stable (black solid line), unstable (red dashed line), and metastable (blue dotted line) cases. Adapted from [88].

The stability of a thin film on a solid substrate is characterized by the effective interface potential, $\phi(h)$, defined as the excess free energy per unit area needed for two interfaces to approach from infinity to a separation distance $h$ [86, 88, 89]. Characteristic interface potentials are shown in Figure 3.1. Three important cases are depicted: the stable mode (black solid line), the unstable mode (red dashed line), and the metastable mode (blue dotted line). As in canonical interaction potentials, $\phi \to 0$ when $h \to \infty$ (*i.e.*, for surfaces infinitely far apart). Stability is distinguished by the second derivative of $\phi$ with respect to $h$ [85, 86, 88, 90]. If $\phi''(h) < 0$, the system has unstable modes with exponentially increasing amplitudes [86, 87, 89, 91]. For the interface potential denoted by the black solid line, the thin film is stable, $\phi(h) > 0$, and the global minimum exists when the film is infinitely thick. In contrast, the unstable case (red dashed line) exhibits a global minimum at thickness $h = h^*$, above which the film will spontaneously

dewet. In the metastable case (blue dotted line) $\phi''(h) < 0$ only for very thin films; *i.e.*, two different dewetting regimes arise. As several groups have explored, there are two mechanisms by which a thin film may dewet: nucleation or spinodal dewetting [87–89, 92–96]. In the metastable case, at smaller thicknesses, the film is unstable and under the auspices of spinodal dewetting; for thicker films, the system becomes stable and nucleation becomes the driving force for dewetting [88]. While many preliminary studies commented on the distinction between nucleation and spinodal dewetting, Seemann *et al*. demonstrated a reconciled consistency between the two regimes and enabled deeper quantitative analysis [88].

Spinodal dewetting is described as the physical analogue to spinodal decomposition of a heterogeneous chemical mixture. In spinodal decomposition, a fluid mixture with excess fluid interfacial energy undergoes compositional fluctuations [97–99]; in spinodal dewetting, a thin film with excess surface energy undergoes height fluctuations [86, 87, 89, 91, 95]. Thermal instabilities driven by Van der Waals forces lead to small surface undulations $Z(x,t)$ modeled in equation 3.1, where $h$ is the film thickness, $\delta h$ is the film amplitude, $R$ is growth rate, $t$ is time, coordinate $x$ is parallel to the surface, and $q$ is the wave vector [91].

$$Z(x,t) = h + \delta h_0 e^{Rt} e^{iqx} \tag{3.1}$$

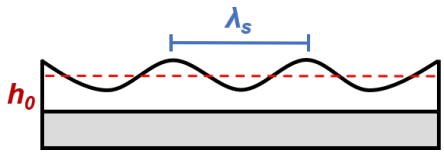


Figure 3.2: Schematic of spinodal dewetting of a thin film on a solid substrate, showing average film thickness $h_0$ and correlation length $\lambda_s$.

When van der Waals forces are the dominant driving force, a critical spinodal wavelength $\lambda_s$ arises where the rate of change is greatest [88, 100]:

$$\lambda_s(h) = \sqrt{\frac{-8\pi^2\sigma}{\phi''(h)}} \tag{3.2}$$

Note here $\lambda_s(h)$ is only real when $\phi''(h) < 0$, the characteristic of a spinodal dewetting film. In addition, $\lambda_s(h) \to \infty$ when $\phi''(h) = 0$.

Previous studies have shown that the radial average of the Fourier transform of a real-space spinodal dewetting image can be used to determine the wave vector $q$ of the system [91, 93]. The peak maximum, $q^*$, corresponds to the inverse size of most unstable surface undulations ($q_M$) during early-stage dewetting, or the size of droplets

during late-stage dewetting [91]. $q^*$ can be related to the correlation length of surface undulations $\lambda(t)$ using the following relationship [85, 100]:

$$\lambda_s(t) \equiv 2\pi/(q^*(t)) \tag{3.3}$$

Here we note that correlation length $\lambda_s$ depends on film-surface interactions, film thickness, and annealing time. For thin films applications, measuring $\lambda_s$ allows us to predict regime in which breakage will not occur. The following sections outline how $\lambda_s$ can be determined experimentally.

### 3.1.2 Characterization techniques

Spinodal dewetting is inherently a composition-dependent, temporal, morphological process. In order to accurately characterize and quantify material dewetting, a system must be able to capture both compositional and topological changes within a carefully controlled environment. To minimize surface contamination, ultra-high vacuum conditions—in which the chamber pressure is $< 10^{-9}$ torr—are critical to minimize the rate of adsorption. To date, studies on spinodal dewetting of metals on various substrates have been limited to *in situ* electron microscopy and computational approaches [87–90, 92–96, 101–108].

The aim of these studies is to ultimately determine the correlation length $\lambda_s$ as a function of dewetting time and temperature. To do so, low-energy electron microscopy (LEEM), low-energy electron diffraction (LEED), and Auger electron spectroscpy (AES) are used to shed insight on the surface composition and structure of the material.

#### Low-energy electron microscopy (LEEM)

To study the temporal and morphological changes of the system, low-energy electron microscopy (LEEM) is a uniquely powerful tool. Briefly, LEEM is a surface-sensitive microscopy technique that allows for real-time, real-space imaging with atomic-scale surface sensitivity.

In the prototypical setup, electrons are emitted from an illumination source and deflected through a prism optic. The electrons decelerate via an objective lens, and the beam impinges on the sample with low energies (*i.e.*, $< 20$ eV, and thus low penetration depth). Backscattered electrons are accelerated into an imaging column, producing a real-space microscope image. This technique particularly lends itself to surface-sensitive applications such as thin film growth and surface dynamics visualization, making it a prime candidate for studying spinodal dewetting.

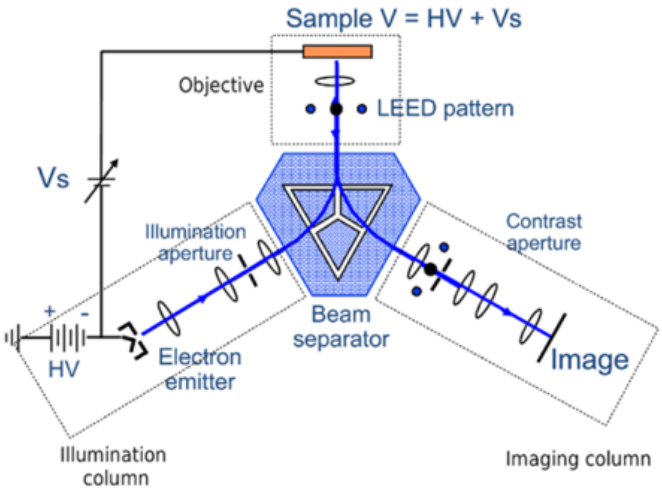


**Low-energy electron diffraction (LEED)**

For well-ordered crystalline substrates, LEED can provide information about the surface structure based on electron backscattering described by Bragg's Law [109]. Because of the nanometer-range inelastic mean free path of electrons at low energies, this technique is much more surface sensitive than X-ray diffraction (few-$\mu m$ inelastic mean free path) and is particularly useful for surface geometry analysis.

**Auger electron spectroscopy (AES)**

Similar to XPS, AES is a surface-sensitive technique that can determine elemental composition and an estimate of film thickness. In AES, a sample is irradiated with an electron beam source (penetration depth of 1–10 nm) and Auger electrons—secondary electrons ejected due to energy transfer from core electron removal—are detected by a spectrometer, enabling non-invasive surface characterization of samples.

In the system described for the following experiments, LEED, LEEM, and AES are all components of a single integrated tool, enabling *in situ* measurements without exposure to atmosphere between intermediate stages.

## 3.2 Experimental setup

The following experiments were performed using the spin-polarized low-energy electron microscopy (SPLEEM) tool at the National Center for Electron Microscopy at

Lawrence Berkeley National Lab (LBNL). See Appendix A for further details on operation.

### 3.2.1 Establishing clean HOPG

Before loading, bulk HOPG was mechanically cleaved and secured into a cartridge holder. The sample was then annealed at mild temperatures ($<$ 600 °C, 2–4 hours) for light outgassing. The purity of the sample was verified with LEED patterns, LEEM images and intensity-voltage spectra, and Auger spectra.

Figure 3.3 shows the LEED patterns for (a) clean single-crystalline graphite and (b) HOPG—note the characteristic rings of HOPG which result from aggregate overlaid orientations of graphite [110]. In Figure 3.3d, the intensity-voltage (I-V) spectrum of HOPG is shown as a baseline reference. The intensity—the grayscale averaged intensity in the field of view—represents surface reflectivity, which is a unique function of the band structure of a given material. For graphite, the characteristic I-V reflectivity curve features an initial low reflectivity below $\sim$ 7 eV, corresponding to the conduction band along the $\Gamma$-A direction perpendicular to the graphite plane surface [111, 112].

Figure 3.4 shows the broad differentiated Auger spectrum (0–1000 eV) of HOPG. The carbon KLL peak ($\approx$ 271 eV) is the only peak present, verifying that oxygen ($\approx$ 503 eV) has been outgassed and the substrate is clean of adsorbates [113, 114].

To assess alternative regeneration methods, HOPG coated with evaporated nickel film was treated by argon sputtering ($1 \times 10^{-6}$ torr, $\approx$ 12 hours, 0.5 keV) and flash heating (30 second annealing with 4.5 minute cool-down periods, $\approx$ 1400 °C, 10 cycles). The LEEM images (Figure 3.5a-b) do not show a significant difference in surface morphology except possible loss of atomic steps. However, this can lead to spurious conclusions. As shown in Figure 3.5c, the intensity-voltage spectrum paints a clearer picture of the efficacy of various HOPG cleaning methods. For exfoliated HOPG (black curve), the characteristic hump around 10–17 V is indicative of pure HOPG, while for sputtered and annealed HOPG (red and blue curves), the intensity is completely flat beyond 4 V—mirroring the characteristic I-V of pure nickel—suggesting that the system is still capped with nickel adlayers. Hence, *ex situ* mechanical exfoliation with mild annealing remains the best way to regenerate a pristine substrate surface.

### 3.2.2 Nickel dosing calibration

To determine the nickel e-beam evaporation rate, Cu(100) was chosen as an arbitrary calibration substrate with similar face-centered cubic crystal structure. Nickel deposition was verified by Auger spectroscopy (see Figure 3.6). Before deposition, Auger peak minima for copper LMM are visible at 776 eV, 849 eV, and 920 eV. After deposition,

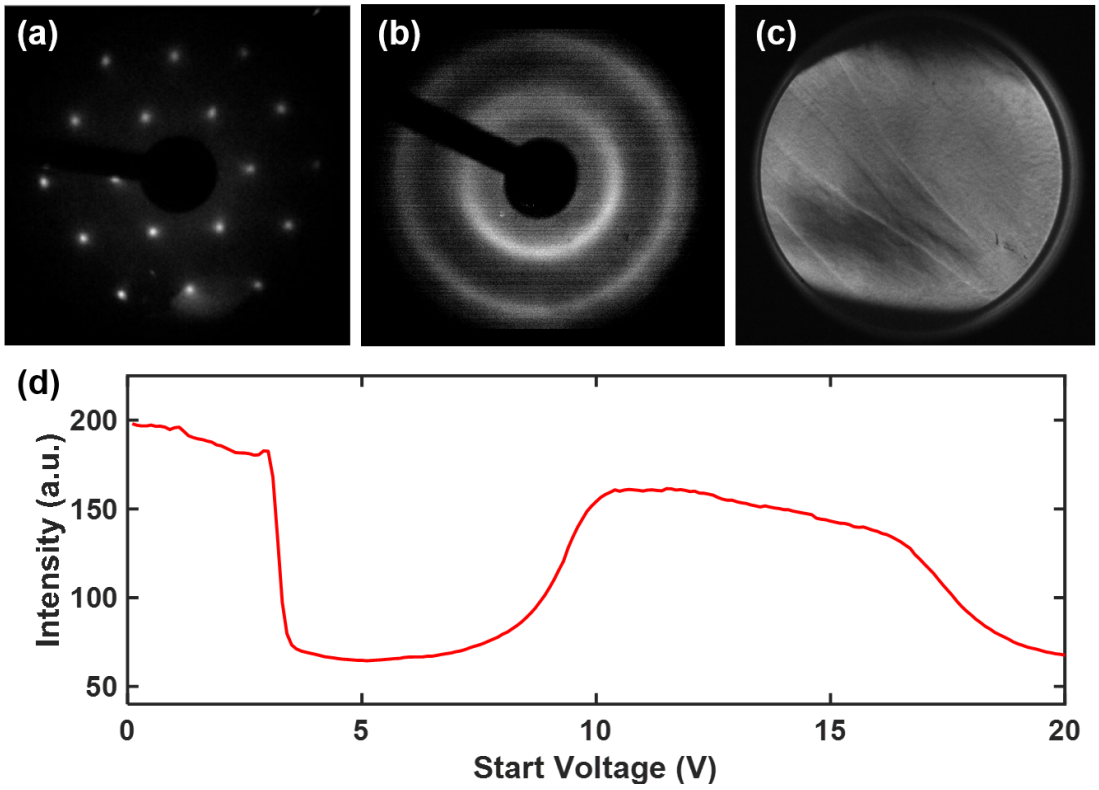


Figure 3.3: Clean HOPG characterization: (a) LEED pattern for reference single-crystalline graphite (266 eV) [110], (b) LEED pattern for experimental highly-oriented pyrolytic graphite (266 eV), (c) LEEM image with step terrace features (3.2 eV start voltage), (d) intensity-voltage spectrum for clean HOPG sample.

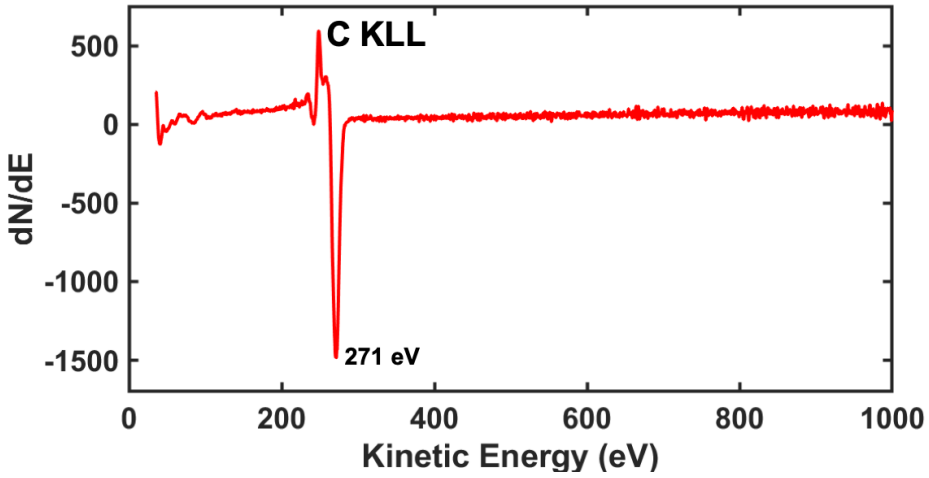


Figure 3.4: Auger spectrum of exfoliated, mildly annealed (<600 °C, 2–4 hours) HOPG showing carbon KLL peak at ≈ 271 eV

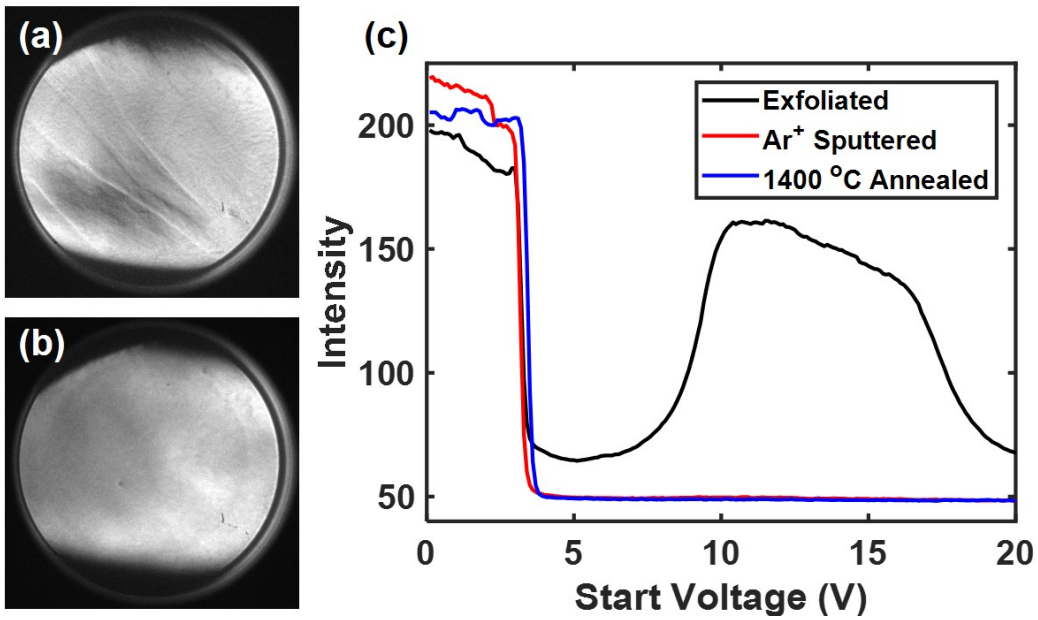


Figure 3.5: Characterization of alternative HOPG regeneration methods: (a) LEEM of mechanically exfoliated HOPG (3.2 eV start voltage), (b) LEEM of $Ar^+$ sputtered, 1400 °C flash-annealed HOPG (3.2 eV start voltage), (c) intensity-voltage spectra for various HOPG treatments.

the copper peaks are subdued in relative intensity compared to the nickel LMM peak minima at 716 eV, 783 eV, and 848 eV [113].

The dosing rate was estimated by calculating the time between oscillations in the reflectivity intensity (Figure 3.7). Based on the peak wavelength (*i.e.*, trough-to-trough distance), the rate was estimated to be approximately 0.012 Ni layers/second (82 seconds/layer of nickel)—however, it should be noted that deposition rates must be recalibrated on a per-session basis due to changes in the melt rod length.

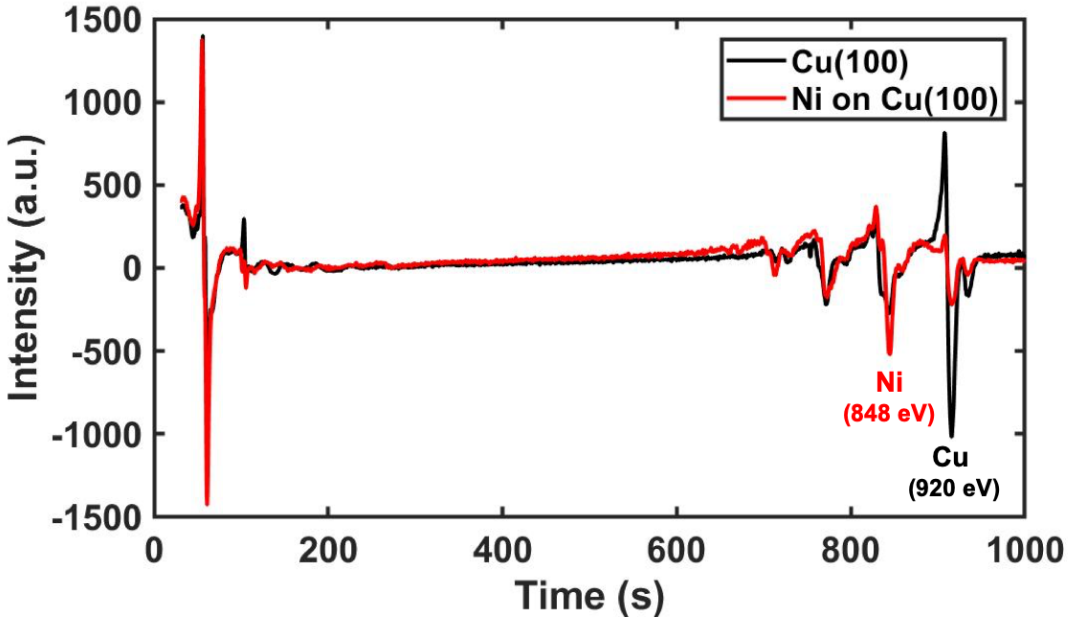


Figure 3.6: Auger electron spectroscopy calibration for nickel on Cu(100). Before deposition (black), the copper LMM 920 eV peak minimum is apparent; after nickel deposition (red), the nickel LMM 848 eV peak minimum dominates.

### 3.2.3 Pyrometer calibration

Temperature measurements were taken using two optical pyrometers designated to separate chambers of the LEEM tool. In optical pyrometry, a non-contact device measures thermal radiation to determine surface temperature of an object. Output radiation is a function of intrinsic material properties; *i.e.*, the object's emissivity value—the object's ability to emit energy by radiation—is a critical parameter to calculate the correct temperature signal.

In certain cases (*e.g.*, within the LBNL SPLEEM chamber), pyrometers may be limited to fixed emissivities—these must be corrected for in order to accurately determine

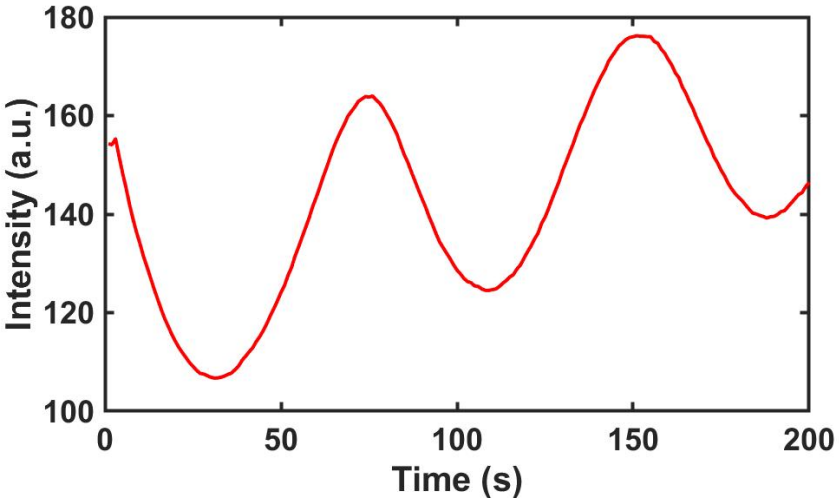


Figure 3.7: Transient LEEM reflectivity during nickel deposition on Cu(100).

temperature. In Figure 3.8, emissivity calibration curves are given for a sample heated from $\approx$ 300–700 °C, showing the pyrometer output at different emissivity values. Note that HOPG has an emissivity range $\sim$ 0.7–0.75 [115].

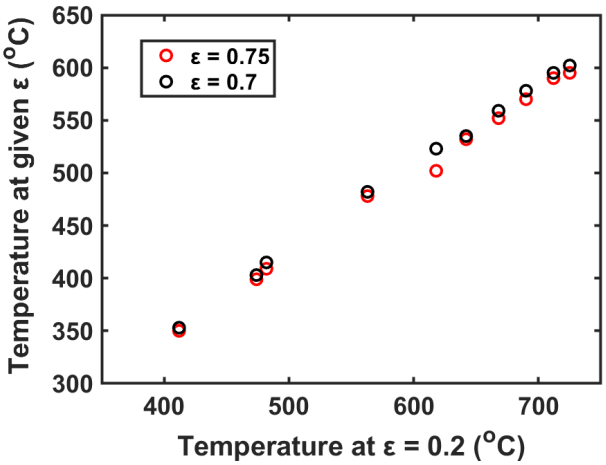


Figure 3.8: Emissivity calibration curves

For all following data, the temperatures (read at $\varepsilon_{0.2}$) are corrected with the following two correlations given in Equations 3.4 and 3.5 (extracted from linear curve fits, $R^2 > 0.997$). Temperatures are still considered within a $\pm$ 50 degree error range.

$$T_{\varepsilon_{0.7}} = 0.79T_{\varepsilon_{0.2}} + 29.21 \tag{3.4}$$

$$T_{\varepsilon_{0.75}} = 0.78T_{\varepsilon_{0.2}} + 29.55 \tag{3.5}$$

### 3.2.4 Nickel deposition and *in situ* heating

For the following experiments, electron-beam evaporation of nickel on HOPG was done using the previously-determined calibration rate. *In situ* heating was facilitated by an on-cartridge hot cathode filament. The base pressure was maintained at or below $10^{-11}$ torr for the entirety of the experiments. Characterization measurements were all done at ambient temperature.

## 3.3 Evaporation of thin nickel

Spinodal dewetting occurs notably at very thin film thicknesses. As a minimal starting point, approximately three equivalent layers of nickel were deposited on the HOPG surface and incrementally heated to higher temperatures for 30 minutes. Figure 3.9a shows the differentiated Auger spectra for 3 layers of nickel annealed to various temperatures, normalized to the maximum carbon peak height. With increasing temperature, the characteristic nickel peaks (peak minima locations $\approx$ 61, 716, 783, 848 eV [113]) have diminishing relative intensities.

Figure 3.9c plots the ratio of peak-to-peak heights of carbon (272 eV) to nickel (848 eV) for each temperature. After heating to approximately 750 °C, the C/Ni ratio increases almost tenfold, suggesting nickel evaporation, nickel intercalation, or partial carbon impurity introduction.

At operating pressures $\approx 10^{-11}$ torr, carbon adsorption/aggregation is assumed to play a relatively minor role. Intercalation of metals under graphene has been demonstrated previously [116] and could be a possible mechanism for apparent Ni loss. However, the nickel peaks of the normalized Auger spectra (Figure 3.9b) show the complete disappearance of nickel signal above 750 °C (blue curve). Since the escape depth (*i.e.*, the inelastic mean free path of Auger electrons) for electron energies of $\sim$50 eV to 3 keV is approximately 4–50 Å[113], AES probes deeper than several layers of Ni and/or graphene (d $\approx$ 3 Å). Mere intercalation would result in mitigated, not nonexistent, Ni Auger signal. While nickel carbide can form when nickel is deposited on graphite, previous studies demonstrated that at least 10 layers of nickel must be deposited to transition from graphitic to carbidic Auger signals [117]. In addition, even if nickel carbide were formed, full decomposition should occur above 400 °C [117–120]. The increase in C/Ni

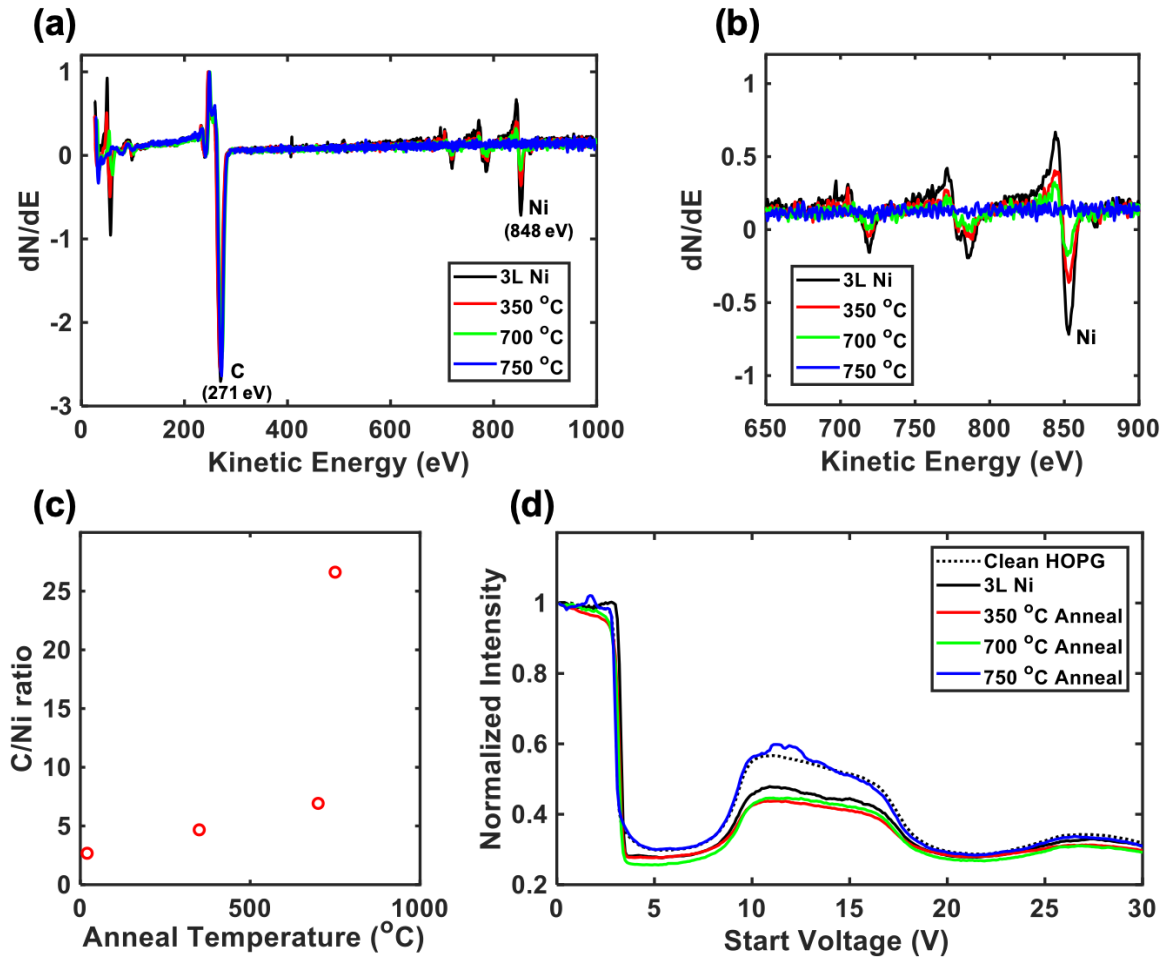


Figure 3.9: (a) Normalized Auger electron spectra for 3 layers of nickel on HOPG with sequential annealing; (b) 650–900 eV regions of Auger spectra with characteristic nickel peak minima ≈ 726, 783, 848 eV; (c) C/Ni ratio as a function of annealing temperature; (d) normalized intensity-voltage curves for pristine HOPG, HOPG after 3L nickel deposition, and 3L Ni-on-HOPG after annealing.

is thus attributed to nickel evaporation. Vapor pressure data for nickel [121], with select temperatures given in Table 3.1 verifies that at base pressures of $\approx 10^{-11}$ torr, nickel will sublime above ≈ 700–800 °C.

Examining the intensity-voltage curves (Figure 3.9d) gives further insight on the surface composition. Progressing from clean HOPG to 3L-Ni-on-HOPG to increasing annealing temperatures, two distinct curvatures arise: (1) rounded drop-off after 3 V with $\sim$ 0.3 increase in normalized intensity arising at 10 V, and (2) sharp drop-off at 3.5 V

Table 3.1: Vapor pressures for solid nickel [121].

| Temperature (°C) | Vapor Pressure (torr) |
|---|---|
| 400 | 2.41E-23 |
| 500 | 4.74E-19 |
| 600 | 9.54E-16 |
| 700 | 3.98E-13 |
| 800 | 5.35E-11 |
| 900 | 3.09E-09 |
| 1000 | 9.40E-08 |
| 1100 | 1.73E-06 |
| 1200 | 2.13E-05 |

with $\sim$ 0.2 increase in normalized intensity arising at 10 V. Notably, the clean HOPG and 750 °C cases have almost exactly the same I-V spectra, suggesting that the substrate has regenerated back to its original form. The minor protrusions at 1.8, 11.2, and 12.1 V are likely artifacts arising from beam instability during measurement.

Using LEEM, the surface morphology can be further clarified. Figure 3.10 shows 8 $\mu$m-field-of-view snapshots of the substrate surface from (a) the pristine state to (b) HOPG capped with a 3L nickel overlayer to (c-e) 3L-Ni-on-HOPG with increasing annealing temperatures. As heating progresses, dark features arise; these are likely to be carbon or nickel aggregations. After the final annealing to 750 °C, the surface no longer shows any dark clusters and looks similar to the initial pristine condition, further suggesting that the thin nickel layers evaporated during annealing.

Similar results are obtained for 15 and 25 layers of nickel on HOPG. A simple back-of-the-envelope calculation accounts for this result. Assuming a Maxwell-Boltzmann distribution of gas at equilibrium, the flux of atoms in a vacuum system is given in Equation 3.6, where $J$ is the flux in molecules/s, $P$ is the vapor pressure of the evaporating material, $m$ is mass, and $k_B$ is the Boltzmann constant, and $T$ is the temperature.

$$J = \frac{P}{2\pi m k_B T} \tag{3.6}$$

Using the vapor pressure relationship discussed previously [121], the evaporation rate at 700 °C is calculated to be $6.9 \times 10^{11}$ molecules/s. Assuming that a single nickel monolayer on HOPG is equivalent to the areal density of carbon on the basal plane of graphite, $1.27 \times 10^{14}$ atoms/cm$^2$ [117], it would take approximately half an hour for a single monolayer of Ni to evaporate. This corresponds well with the results shown

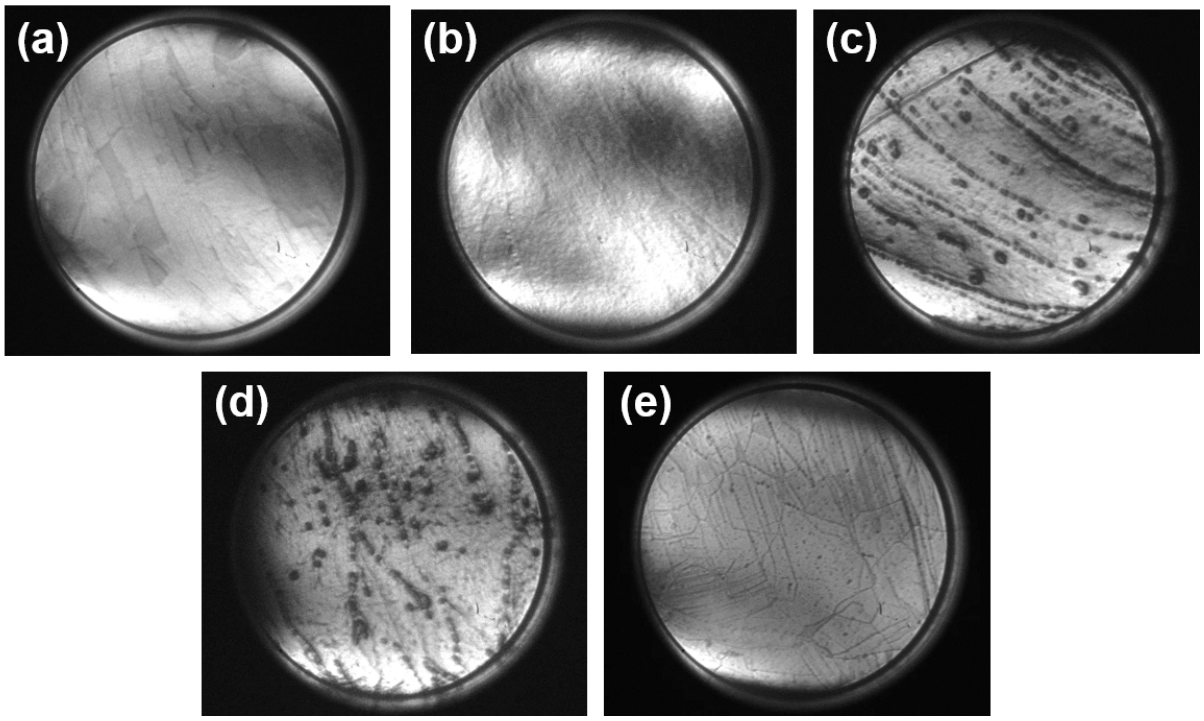


Figure 3.10: 8 $\mu$m-field-of-view 3.2V start voltage LEEM images of (a) pristine HOPG, (b) 3 layers Ni on HOPG, (c) 3L Ni-on-HOPG after 350 °C anneal, (d) 3L Ni-on-HOPG after 700 °C anneal, (e) 3L Ni-on-HOPG after 750 °C anneal.

previously. To account for the loss of Ni by evaporation, 75 layers of nickel are deposited on HOPG for the following sections.

## 3.4 Developing the analysis methodology

To gain a more quantitative understanding of the dynamics of spinodal dewetting, image processing must be carefully implemented. Precise study of morphological changes is particularly important to extract accurate length measurements and relevant parameters. While manual image analysis is possible, the propensity for human error and the sheer volume of images makes this an impractical solution. Computational approaches, on the other hand—when implemented judiciously—are robust alternatives that promise precision and minimize subjective judgments.

Based on earlier understanding of nickel evaporation at elevated temperatures, 22.5 nm nickel is deposited on clean, outgassed HOPG. The sample is annealed sequentially up to $\approx$ 900 °C with continuous image acquisition.

The original LEEM images (8 $\mu$m field of view) are shown in Figure 3.11 for three different start voltages. The images have non-ideal relative contrast and uneven beam distribution, but dewetting features are clearly visible. As described earlier, the average intensity of the image depends on the chosen start voltage (Section 3.2.1). Typically, the image brightness drops off sharply at the sample work function, so it is ideal to choose an imaging start voltage that is lower than both the substrate and thin film material work function. For this particular system, with HOPG with a work function of $\approx$ 4.4–4.8 eV [122, 123] and nickel with a work function of $\approx$ 5 eV, we end up choosing a lower start voltage of 3.2 eV because it lies in the optimal range of image contrast, feature visibility, and micro-channel plate gain.

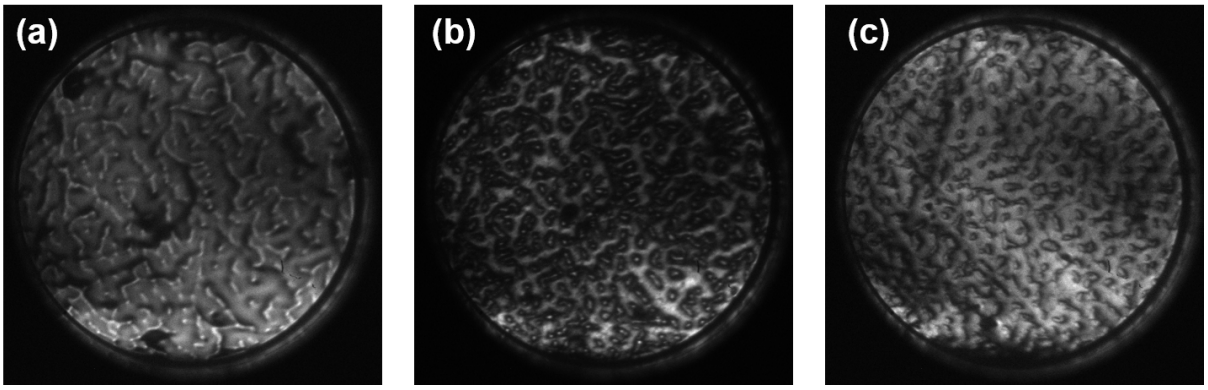


Figure 3.11: 8 $\mu$m field of view LEEM images of 75 layers of Ni on HOPG after heating.

For the following sections, we focus on the images following $\approx$ 730 °C annealing, imaged at 3.2 V start voltage for assessment of image analysis techniques. First, corrections are applied to improve analysis accuracy. Afterwards, the radial power spectral density (PSD) is applied in order to extract quantitative interaction parameters from the images. Several methods are evaluated, discussed, and concatenated to enable the most judicious image analysis for *in situ* LEEM.

### 3.4.1 Image processing

Three software packages were chosen to facilitate image processing because of their unique capabilities in data analysis.

To begin, Gwyddion—an open source scanning probe microscopy (SPM) tool used for visualization and analysis—was used for initializing and preliminary processing. Since this software was developed specifically for SPM techniques such as atomic force microscopy (AFM), Gwyddion includes particularly useful and specific tools for analyzing profilometry data.

ImageJ, a public domain Java-based program, was chosen as the supplementary image processing tool. While originally designed for biological image processing, it has enormous capabilities for image analysis and is amenable to user-defined plugins.

Finally, MATLAB was used for final calculations of the power spectral density functions. The ability to fine-tune calculations and handle large matrices with precision and without excessive computation time is particularly advantageous.

**Initializing leveling tilt/background adjustment**

In electron microscopy, image quality and resolution can be tricky to manipulate, refine, and maintain. For high-temperature annealing in particular, the energy from heating leads to continuous microvibrations that result in blurriness to the output image and physical tilting/shifting of the substrate itself. In addition, the electron beam may be unstable for short periods of time. In LEEM, complex coordination of lenses and magnets introduces difficulties in attaining a perfectly flat beam for imaging. Luckily, SPM programs such as Gwyddion are designed to handle these concerns.

In the ideal case, SPM data is perfectly level and the only initializing needed is moving the minimum to zero (*Fix Zero*). In some cases, SPM microscopes will not be level and require simple plane leveling (*Plane Level*). In complex cases such as LEEM images, however, more discretion must be used to accurately account for variations in the tilt and beam intensity.

For the specific case introduced earlier (75L-Ni-on-HOPG, annealed to h3), two possible leveling functions are selected as the most viable options for level correction: (1) plane leveling with polynomial background subtraction and (2) base flattening. Polynomial background subtraction uses data fit to given polynomial degrees (horizontal and vertical, $m$, $n$ in equation 3.7) and subtracts this from the image [124].

$$\sum_{j=0}^{m}\sum_{j=0}^{n} a_{j,k}x^j y^k \tag{3.7}$$

In contrast, the *Flatten Base* function in Gwyddion uses a combination of facet and polynomial leveling with automated masking to optimize for a sharp height distribution peak [124]. In Figure 3.12, the height distribution for the original as-imported image (a) is compared with the flattened base (b) and polynomial background (c) corrections. The original image (red curve) shows sharp jagged peaks and an irregular distribution. In contrast, both of the leveled cases have a gradual sloping that is more analogous to a typical distribution profile. Comparing the corrections, the flattened base peak position appears to be more well-aligned with the profile of the original image; the polynomial background leveling appears slightly shifted, potentially missing or overcorrecting for

image features which could lead to misleading results. The flattened base correction is chosen as the optimal initial condition for processing.

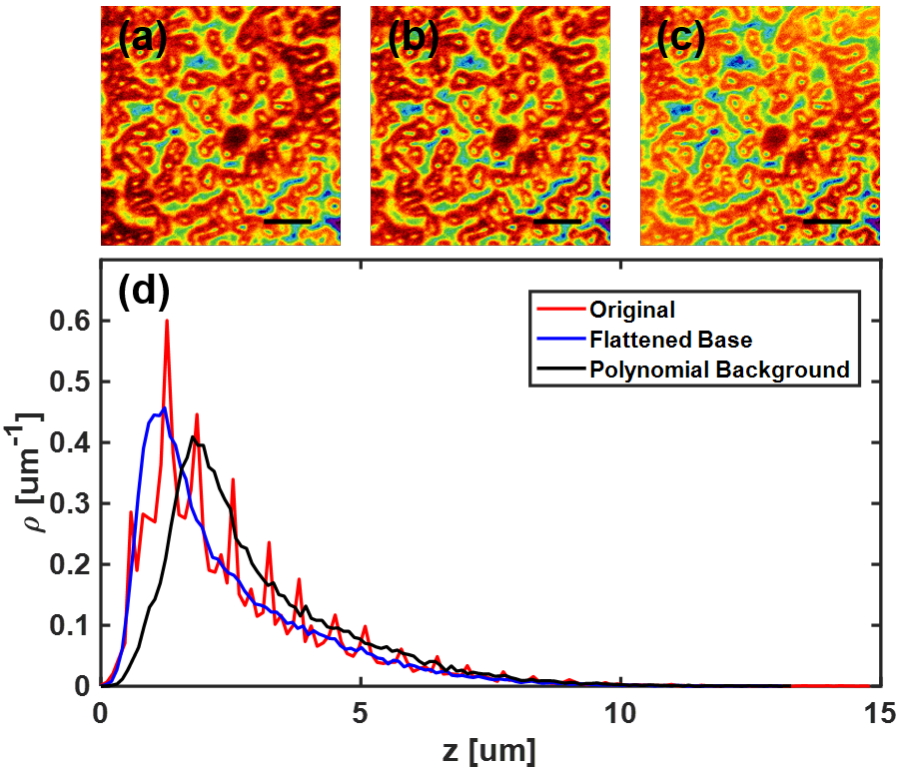


Figure 3.12: 75L-Ni-on-HOPG images (a) as-imported original (b) image corrected with flatten base function (c) image corrected with plane level and polynomial background subtraction (d) height distributions of a-c. Scale bars are all 1 $\mu m$.

### Thresholding/masking

After leveling, the image must be binarized to enable further particle analysis. At this point, we transition to ImageJ to clarify the process in 8-bit grayscale images rather than the multicolored Gwyddion output. Thresholding segments an image into white background and black features (or vice versa) [125]. In Figure 3.13, the base-flattened image is converted to grayscale and modified with a range of thresholds. At low threshold, many features are lost, while at high thresholds, edges and extra features may incorrectly dilate feature sizes. Thresholding at $\approx 66$ % is found to be the optimal compromise between the extremes.

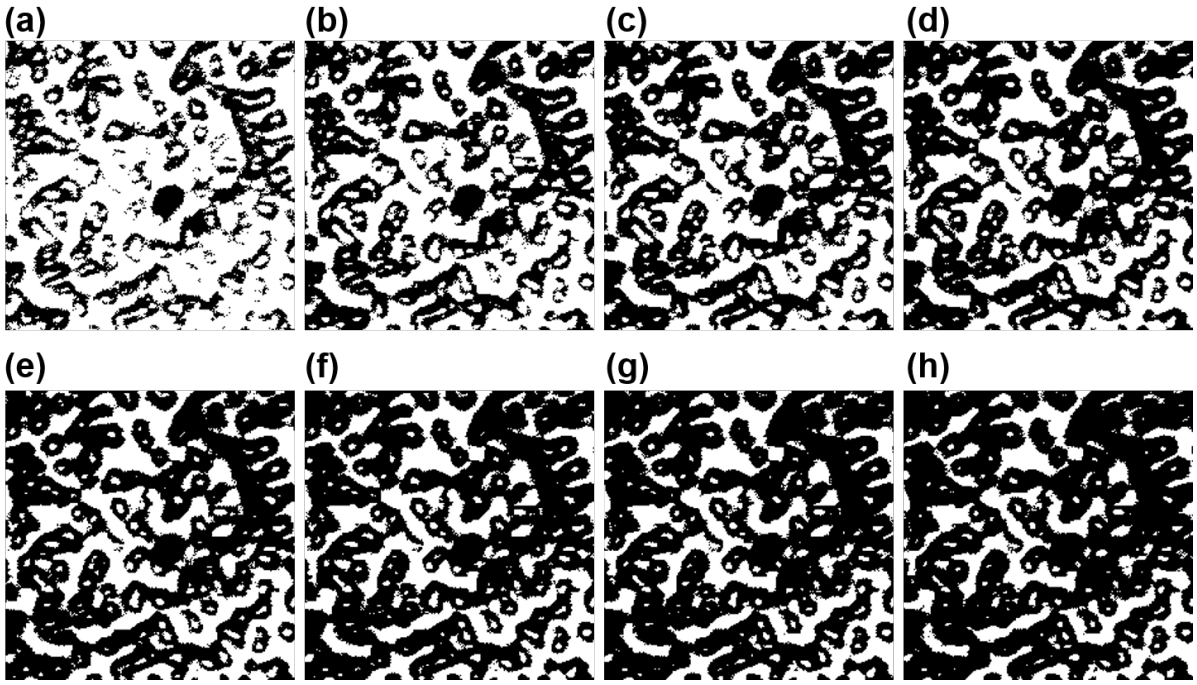


Figure 3.13: 75L-Ni-on-HOPG images with thresholding levels at (a) 33 %, (b) 48.0 %, (c) 53.0 %, (d) 58 %, (e) 62 % (f) 66 %, (g) 68 %, (h) 72 %.

### Correction/filling of voids

Additional corrections can be applied to reduce imaging artifacts. As mentioned previously, microvibrations (*i.e.*, substrate temperature changes) lead to blurriness and noise in LEEM images. In addition, the relatively lower resolution of the images introduces unwanted noise during thresholding. In ImageJ, *Despeckle* uses a median filter in a $3 \times 3$ neighborhood to reduce standard "salt and pepper" noise [125]. Figure 3.14b shows the enhanced clarity in border regions enabled by the *Despeckle* function.

Due to the imaging optics, peaks of hill features are seen as white holes within black regions. Therefore, void filling is critical to have an accurate measure of disc radii and not over-count concentric regions. ImageJ *Fill Holes* can be used to do so in an ideal case; however, it is clear from Figure 3.11c that hole filling via ImageJ is not an effective solution when there are unbounded regions. Rather, manual void filling using Gwyddion (using grain masking with *Fill Voids*) is used to produce the most accurate result without overfilling.

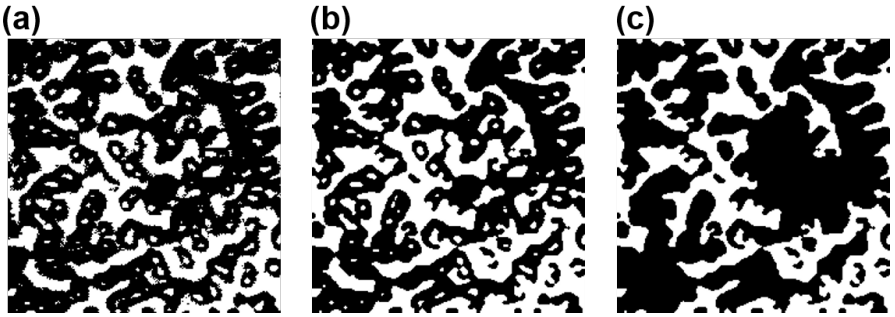


Figure 3.14: 75L-Ni-on-HOPG images corrected with ImageJ functions: (a) *Threshold*, (b) *Despeckle*, (c) *Fill Holes*.

### Radial PSD

After the image is in its most representative state after the corrections mentioned above, the radial PSD can finally be calculated. For this process, a user-developed MATLAB function for calculating radially averaged surface roughness/topography power spectrum is used [126]. For a given image (*i.e.*, matrix of height values), the function calculates the discrete Fourier transform of the surface topography and takes a radial average of the power spectrum to obtain the 2D PSD. Figure 3.15 applies this function to several images of interest: (a) the original flattened-base image, (b) after additional thresholding, and (c) after thresholding and manual void filling. As expected, the curves have markedly different tail curvatures. Despite the corrections, the low-q data points are quite noisy and a clear maximum $q^*$ is difficult to ascertain.

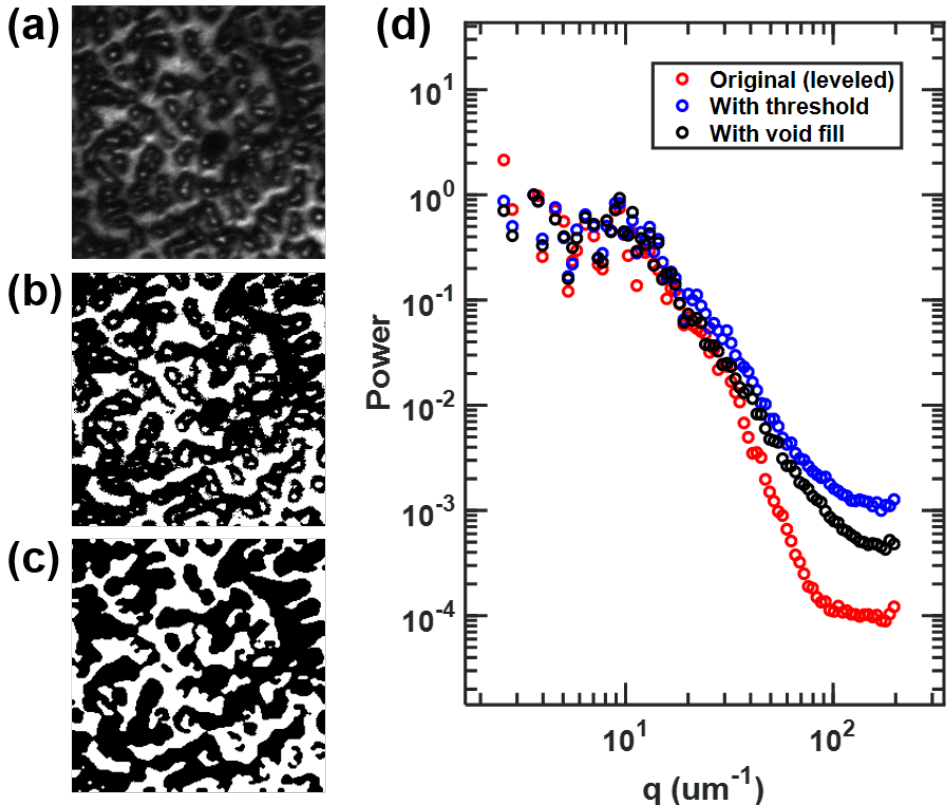


Figure 3.15: Power spectral density functions calculated from discrete Fourier transforms of LEEM surface topography of 75L-Ni-on-HOPG with various corrections: (a) the original flattened-base image, (b) after additional thresholding, and (c) after thresholding and manual void filling.

While the built-in features of Gwyddion and ImageJ enable improved image quality for PSD analysis, the corrections are insufficient to account for poor image resolution, illumination uniformity, and inescapable blurriness/significant noise. Additional adjustments must be made with care (*i.e.*, not to overcorrect), consistency (*i.e.*, systematic equivalency between sets), and specificity to the system of interest (*i.e.*, with appropriate assumptions).

### 3.4.2 Texture analysis microscopy

Texture analysis microscopy (TAM) was developed by Yongxiang Gao and Matthew Helgeson group at the University of Caliornia at Santa Barbara. This methodology uses textural correlation maps to optimize morphological parameters in a nonideal image [127]. TAM was created to enable quantification of poor-quality optical images—including colloidal fluids undergoing spinodal dewetting, collodial fluids undergoing spinodal decomposition, and anisotropic objects in fluid—with uneven illumination, low signal-to-noise ratios, optical artifacts, and clear anisotropy. It is intended to act as a pre-processing method before fast Fourier transform (FFT) analysis (for understanding phase separation dynamics) and feature localization, both of which are relevant in the case of spinodal dewetting.

The algorithm starts with an input image and generates a Gaussian textural kernel $\boldsymbol{G}$ with distinct Gaussian features defined by characteristic size $2w+1$ and variance $w_g^2$. The kernel is then correlated to a sub-matrix of the initial image $\boldsymbol{B}$, generating a correlation coefficient map with globally optimized parameters. Using this map, local features are identified and then locally optimized for the most probable textural features $\bar{w}$ and $\bar{w_g}$. Further details can be found in Gao *et al.* 2014 [127].

#### Initialization

The starting image was the Gwyddion-imported flattened-base standard with no additional corrections (see Section 3.4.1). To ensure coherence with the algorithm, the image must be cropped to a square region including relevant features. Although any $M \times M$ matrix is acceptable, a $256 \times 256$ matrix is chosen as an appropriately large sample region, covering more than half of the acquired LEEM field-of-view window while minimizing misaligned beam artifacts. According to Gao *et al.*, the selection of image size should not strongly affect the final PSD result calculated (see Figure 3.16) [127]. Besides the extremely low and high q-values, the structure function peak and sharpness are mostly unaffected by a smaller image size. Parallel studies on the resolution (pixel size) effects show that there is no apparent effect of pixel size on the power spectra of Fourier transforms of the textural maps, except the inherent truncation at high $q$ values [127].

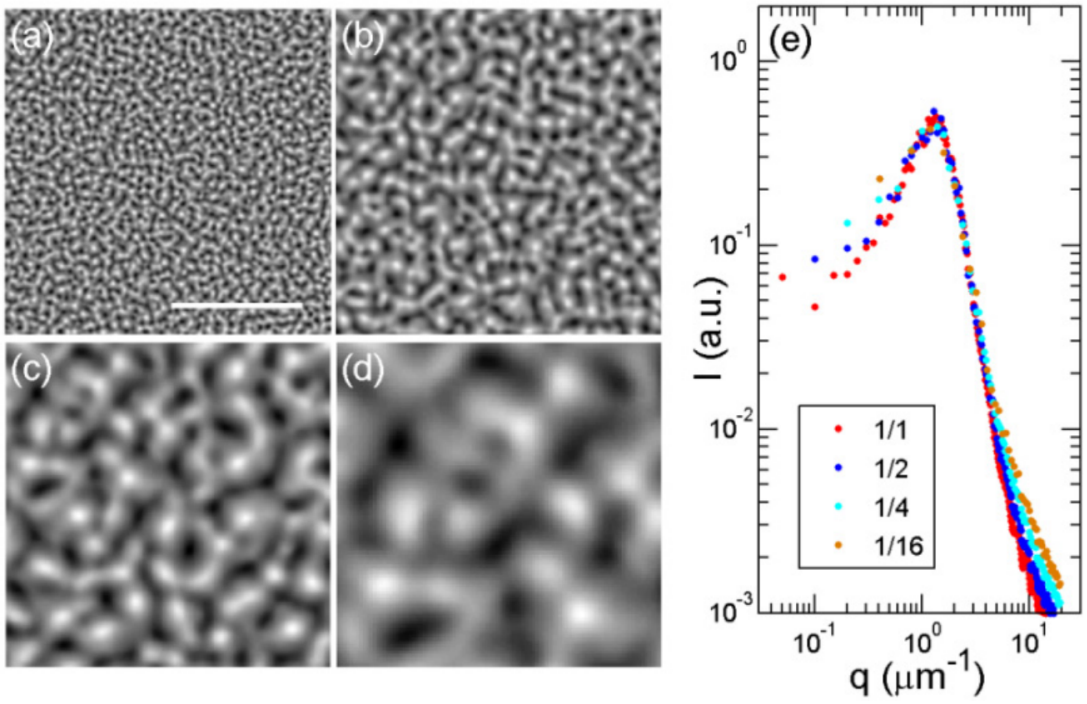


Figure 3.16: Effect of image size on structure function for nanoemulsion droplets undergoing spinodal decomposition. (a) Original size (scalebar 50 $\mu m$), (b) 1/2 original size, (c) 1/4 original size, (d) 1/16 original size. (e) Radially averaged Fourier transforms of (a)-(d). Reproduced from [127].

In addition to the raw image, the local Texture Analysis Microscopy algorithm requires additional inputs: radius of the Gaussian template texture $w$, width of the Gaussian template texture $w_g$, and pixel size (in micron). The values of ($w$, $w_g$) determine the template texture and are optimized within an appropriate range (see Section 3.4.2). The pixel size is calculated simply from the image scale and pixel dimensions of the image.

**Textural mapping**

The sensitivity of the algorithm to values of ($w$, $w_g$) can be better understood by considering the underlying textural mapping function, *i.e.*, the calculation of the correlation coefficient. The correlation coefficient $\rho$ is defined as the statistical similarity between the textural kernel $\boldsymbol{G}(w, w_g)$ and region of interest $\boldsymbol{B}$(x,y,$w$):

$$\rho(x, y, w, w_g) = corr\left[\mathbf{B}(x, y, w), \mathbf{G}(w, w_g)\right] = \frac{\sum_{i=1}^{2w+1}\sum_{j=1}^{2w+1}(B_{i,j} - \overline{B})(G_{i,j} - \overline{G})}{(2w+1)^2\sigma_B\sigma_G} \tag{3.8}$$

As such, the range of possible values for the correlation coefficient is between [-1, 1], with the limits of -1 and 1 corresponding to perfect anti-correlation and perfect correlation, respectively. Figure 3.17 shows the correlation coefficients as a function of ($w$, $w_g$). The ($w$, $w_g$) values that result in the highest value of $\rho$ are chosen as the optimized parameters used in later local optimization.

In the ideal case, a wide range of values would be used to scan for the optimal input parameters. However, the computational time for each additional input is fairly significant: each iteration (*i.e.*, each ($w$, $w_g$) evaluation) of the texture analysis function takes about 6–8 seconds. A large array of test values can quickly add up. To account for this, limits to the appropriate search range are estimated using the line measurement tool in ImageJ.

**Local feature recognition**

With specified ranges of $w$ and $w_g$ defining the textural map, feature recognition can be applied using additional criteria: the minimum distance between local maxima, $r$, and the minimum cutoff intensity of local maxima, $I_{cut}$. These parameters are used to sort features by their intensities and position constraints, then identify the most probable locations of local maxima for a given ($w$, $w_g$). For spinodal dewetting, the most important considerations are that $r$ does not overcount features—especially potentially unfilled voids—and that $I_{cut}$ does not overcount noise and spurious features. Further explanation and clarification are well-detailed in Gao *et al*. 2014 [127].

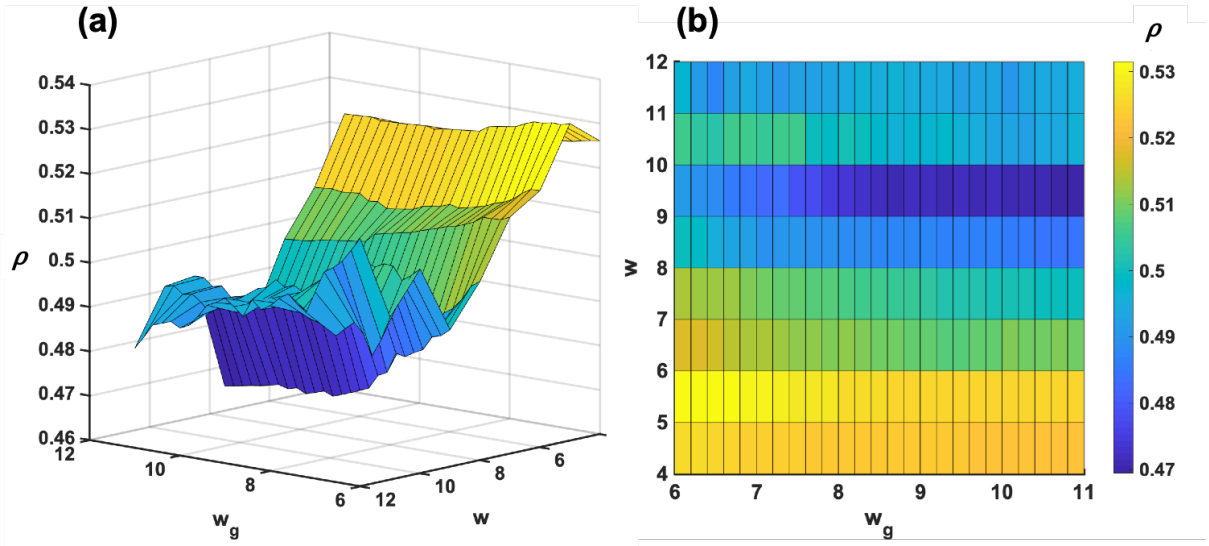


Figure 3.17: Sensitivity analysis of input parameters in texture analysis microscopy algorithm applied to 75 layers of Ni-on-HOPG.

### Comparison to Gwyddion/ImageJ analysis

Following the selection criteria and careful selection of $r$ and $I_{cut}$ detailed above, the TAM algorithm is applied to the image of interest. Figure 3.18 shows the comparison between (a) the original Gwyddion-leveled image, (b) the same image with 40% brightened correction (for comparison ease), and (c) optimum correlation coefficient map calculated based on the most probable feature morphologies (c). Comparing these images, it is clear that the correlation coefficient map effectively depicts a reasonable parallel to the true image, but with a higher signal-to-noise ratio, minimized noise, and improved specular contrast. In many regions that had shadow effects due to indirect beam alignment on "tall" morphological features are minimized. Notably, features that were seemingly connected or consolidated into singular regions are more clearly delineated in the textural map. The enhanced fidelity enabled by TAM is significant and provides greater confidence for subsequent analysis.

In Figure 3.19, the power spectral density function is calculated for the optimized correlation coefficient map. As expected, curvature of the PSD is markedly improved compared to the previous cases with low-fidelity images after Gwyddion/Image-J processing shown in 3.15. As such, this curvature enables more accurate quantification of the $q^*$ position. In the end, this gives a general spinodal dewetting length of approximately 0.4 $\mu m$, comparable to values obtained from manual analysis. The principles outlined above are used to improve the validity of the assessment of $q^*$ given a non-

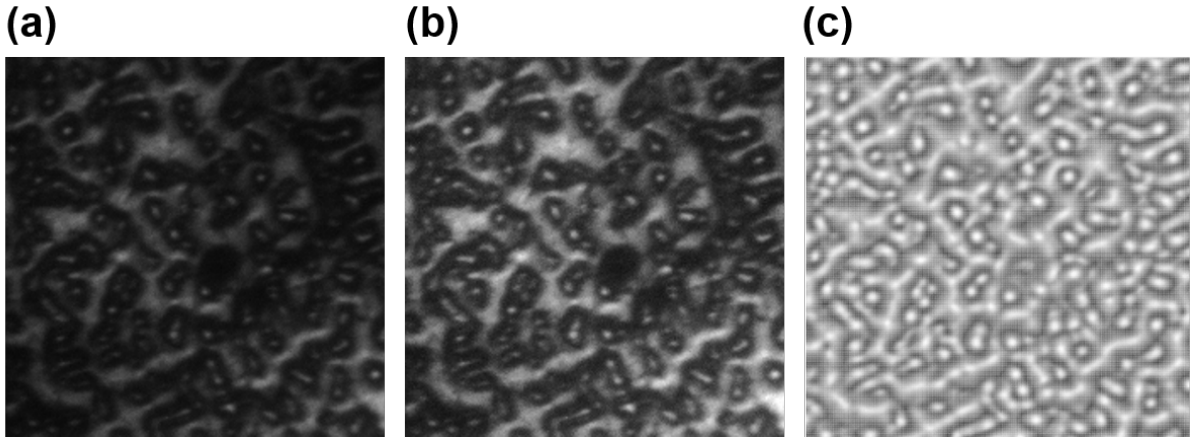


Figure 3.18: Application of texture analysis microscopy on 75 layers of Ni-on-HOPG. (a) Original imported image, (b) 40% brightened image for comparison purposes, (c) calculated optimum correlation coefficient map based on image (a).

ideal acquisition image.

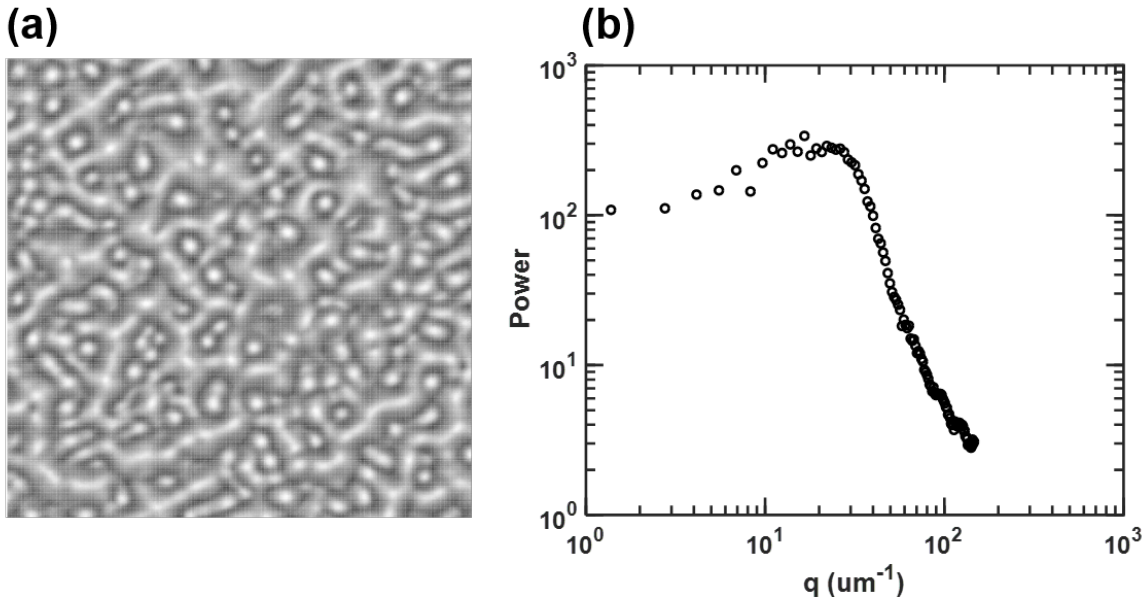


Figure 3.19: Application of texture analysis microscopy on 75 layers of Ni-on-HOPG. (a) TAM-calculated optimum correlation coefficient map, (b) PSD calculation based on (a).

As mentioned previously, the selection of $w$ and $w_g$ dictates the correlation coefficient map and thus the resulting quantification of $q^*$. The values of $q^*$ for a range of $w$ and

$w_g$ are shown in Figure 3.20. The sensitivity of $q^*$ appears to be more significant for incremental texture width $w_g$ than for comparative texture radius $w$ increments; the peak position shifting more as a function of edge sharpness makes sense intuitively when considering the texture kernel morphology in low-valued ranges.

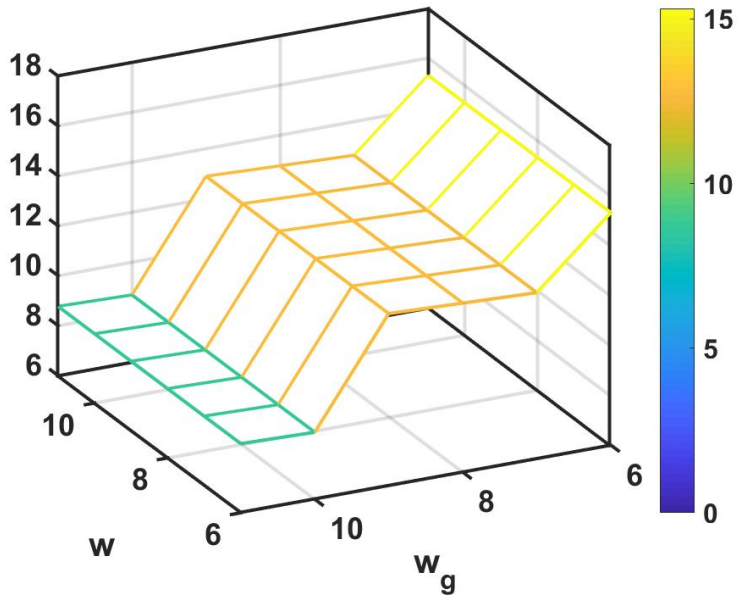


Figure 3.20: Sensitivity analysis of $w$ and $w_g$ values on $q^*$.

At the end of the day, the ultimate goal of this extensive image optimization and analysis is to systematically design a protocol for amplifying the quality and ensuring accuracy in image quantification. The steps and choices are means for enabling the clearest, most reliable starting points achievable with images gathered from low-energy electron microscopy.

## 3.5 Spinodal dewetting length analysis

### 3.5.1 Effect of metal thickness

The spinodal dewetting length has a unique relationship with metal film thickness; this is particularly relevant when there is a need to resolve or quantify thickness thresholds for a given system. Theoretical models have shown that the dewetting wavelength $\lambda$ should scale with film thickness $h$ according to equation 3.9. The characteristic length

scale $\alpha$ depends on the substrate and film materials and encapsulates the Hamaker constant and surface tension to characterize the surface stability of a particular system [92, 95].

$$\lambda = 2\pi\sqrt{\frac{2}{3}\frac{h^2}{\alpha}} \tag{3.9}$$

To probe the $\lambda(h)$ relationship, nickel thicknesses of 0.9, 4.5, 7.5, or 22.5 nm were deposited on freshly cleaved and outgassed HOPG and annealed to 350 °C. The deposition was verified by AES and LEED (Figure 3.21). Following characterization, the sample was heated immediately to the target temperature using a built-in cartridge filament element. Real-space images of the sample surface were collected during the ramp-up process through thermal equilibration—characterized by cessation of image drift, sample drift, and focus offset. After image collection, the sample was cooled back to room temperature before further characterization. The HOPG was recleaved, reloaded, and recleaned after each experiment. The same procedure was repeated for each of the nickel thicknesses. The equilibrated acquisitions were used for image analysis, following image optimization with the TAM methods outlined previously.

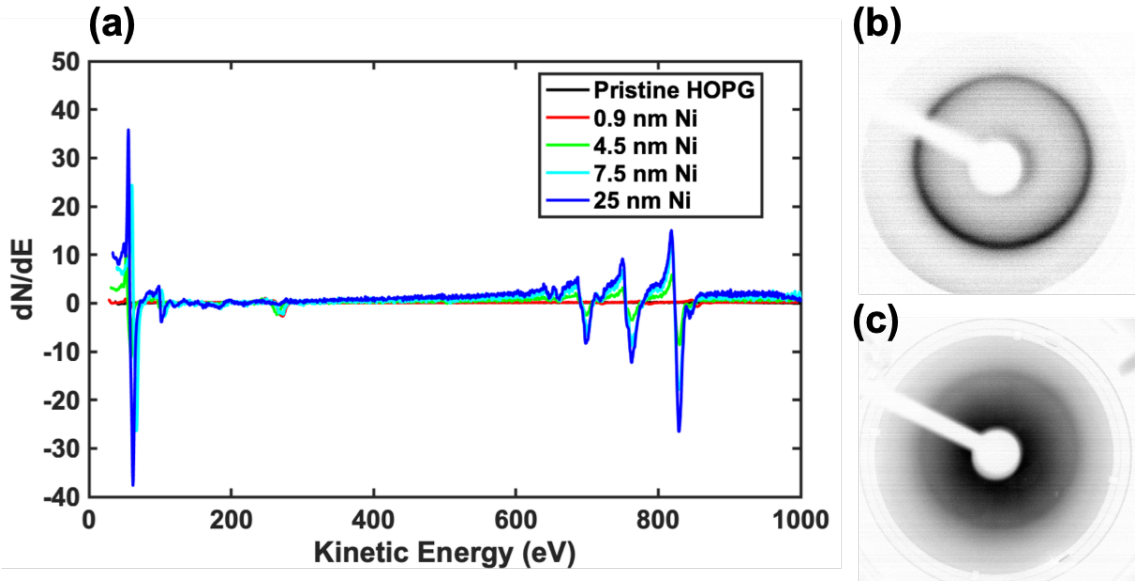


Figure 3.21: *In situ* characterization after Ni deposition on HOPG. (a) Auger spectroscopy data of various thicknesses, (b) low-energy electron diffraction pattern of pristine HOPG at 144 eV, (c) low-energy electron diffraction pattern of 7.5 nm Ni-on-HOPG at 144 eV.

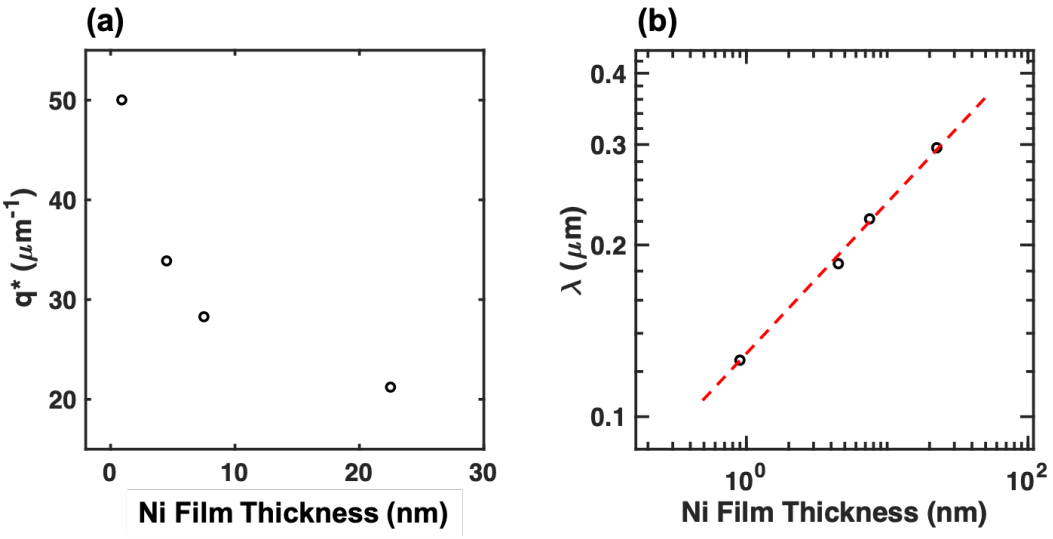


Figure 3.22: Experimental values of (a) spinodal wavelength maximum $q^*$ and (b) characteristic wavelength $\lambda$ as a function of 0.9–22.5 nm nickel film thickness on HOPG, extracted from images processed with texture analysis microscopy algorithm.

Figure 3.22 shows the resulting $q^*$ values extracted from the equilibrated samples deposited with a range of nickel thicknesses. The $q^*$ value decreases as nickel thickness is increased. Using the relation $\lambda = 2\pi/q^*$ (equation 3.3), plot 3.22b depicts the characteristic spinodal dewetting wavelength $\lambda$ increasing with increasing film thickness. Equation 3.9 suggests that a quadratic dependence is expected for $\lambda(h)$. Indeed, a linear fit of the logarithmic spinodal dewetting length as a function of film thickness (dotted red line) shows strong correlation with the data ($R^2 = 0.99$). As such, the experimental data matches theory, and the characteristic parameter $\alpha$ is calculated to be 5.1 nm, which is on the same order of magnitude as literature for spinodal dewetting of gold on fused silica ($\alpha = 4.3$ nm) [95].

The characteristic rise time $\tau$ is defined in equation 3.10, where $\nu$ is the space velocity (surface energy $\gamma$/viscosity $\eta$).

$$\tau = \frac{4}{3}\frac{h^5}{\alpha^4 \nu} \tag{3.10}$$

For liquid nickel at the melting temperature, $\nu$ is 361 m/s ($\gamma = 1.7$ N/m [128, 129], $\eta = 4.7 \times 10^{-3}$ Ns/m$^2$ [130, 131]) and the rise time is calculated for various thicknesses as shown in Figure 3.23. The rise time of a nickel thickness of 25 nm is calculated to be approximately 52 ns. Although this value is below that of the acquisition resolution capabilities of the LEEM tool, it is still possible to extract valuable equilibrium data from

the acquired images.

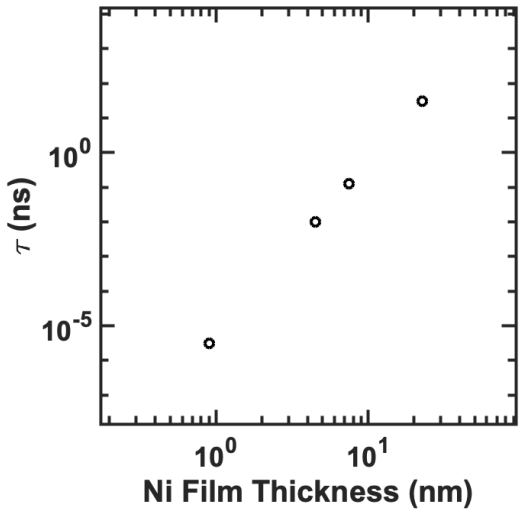


Figure 3.23: Calculated values of characteristic rise time $\tau$ as a function of 0.9–22.5 nm nickel film thickness on HOPG, based on from images processed with texture analysis microscopy algorithm.

### 3.5.2 Effect of time

Temporal variations in spinodal wavelength can also bring insight into the character of interfacial energetics. Xie et al. described that spinodal dewetting wavelength should decrease with time [91].

Similar to the protocol outlined previously, 7.5 nm nickel was deposited on newly-cleaved, outgassed HOPG and then annealed immediately to the target temperature (350 °C). Upon heating, the sample expands and the beam position drifts considerably as a result of the added applied charge, leading to inevitable image loss in the initial stages of the heating. The acquisition was saved as soon as temperature neared or appeared to reach stability. Images were recorded and analyzed by TAM as previously described.

Consistent with earlier calculations of the characteristic rise time on the order of nanoseconds for nickel thicknesses of interest, no apparent changes in the surface morphology could be clearly captured via real-time LEEM. Figure 3.24 plots the calculated $q^*$ of sequential images taken of 7.5 nm nickel-on-HOPG in real time. At early times in the annealing process, the value of $q^*$ appears to be nearly constant, with $R^2$ = .004, indicating lack of correlation with time.

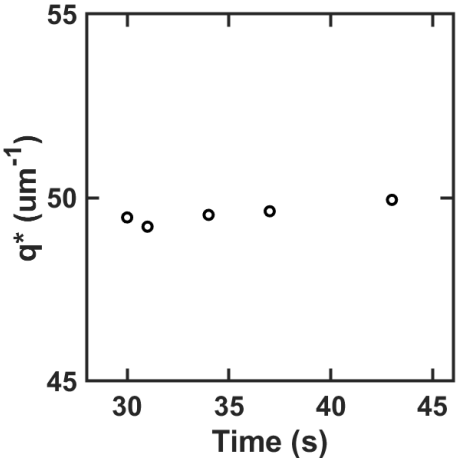


Figure 3.24: Experimental values of $q^*$ at short times for 7.5 nm nickel-on-HOPG, suggesting lack of correlation with time during initial stages.

The acquisition resolution of one second is limited by a complex array of optics and electron gun constraints; ultimately, it comes down to an optimization of trade-offs between acquisition averaging time and image resolution. Beyond temporal limitations, the heating process also leads to sample expansion and physical shifting, requiring constant readjustments of tilt, focus, and beam alignment. Evaporation of material during heating also leads to poorer resolution. Nevertheless, the resulting images still paint a clearer picture of the phenomenological transitions that are happening at the interface of nickel and HOPG during mild annealing.

Figure 3.25 shows the morphological changes on the surface with extended annealing time. The representative image captures from the start of annealing (a) to the end of 60 minutes (h) show the progression from a smooth, pristine surface to a rough, mottled surface with notable clusters over time.

To further elucidate the elemental composition and local bonding states, Figure 3.26 shows additional *ex situ* characterization by XPS for the oxygen 1s, carbon 1s, and valence band regions. Figures 3.26a-c show the spectra for pristine HOPG and Figures 3.26 show the spectra for 7.5 nm Ni deposited on HOPG annealed up to $\approx$ 420 °C for 3.5 hours. In the oxygen 1s region, after nickel deposition and annealing, there is the appearance of an extra shoulder around 530 eV binding energy, which is attributed to the NiO peak. There is no shift in the carbon 1s peak binding energy position, which suggests that there is no reaction happening between the nickel and carbon to form nickel carbide at these temperatures. As expected, the HOPG does not have a clear valence band peak.

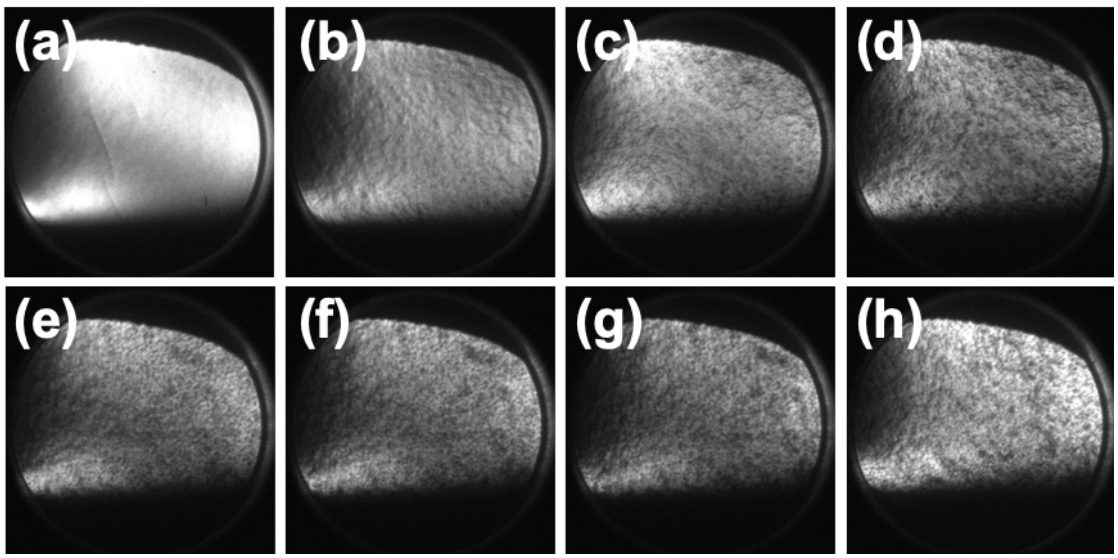


Figure 3.25: Representative LEEM images of 7.5 nm nickel-on-HOPG annealed to ≈ 350 °C from (a) 0 minutes to (h) 60 minutes.

### 3.5.3 Nickel-on-HOPG summary

*In situ* LEEM studies of thin nickel films deposited on HOPG can provide insight on surface morphology during and after annealing. Above a minimum critical thickness of nickel, it is possible to acquire real-time, real-space images using LEEM.

In these studies, image processing and texture analysis microscopy were applied to obtain quantitative information from the acquired LEEM images. A characteristic interaction parameter length $\alpha$ was calculated to be 5.1 nm for nickel on HOPG. The characteristic rise time $\tau$ was calculated to be approximately 52 ns for 25 nm nickel on HOPG. These values and corresponding LEEM images, LEED patterns, and XPS analysis suggest physical dewetting without chemical reaction with graphite.

Although nickel is a commonly-used catalyst in top-layer graphene synthesis, other metals (*e.g.*, copper) are also studied [17, 26, 43]. Analogous studies of other metals on HOPG could provide further information on the relative proclivity for spinodal dewetting on HOPG.

## 3.6 Copper-on-HOPG comparison

Parallel experiments were done with copper on HOPG in order to explore the differences between the interfacial characteristics of each of these metals with HOPG.

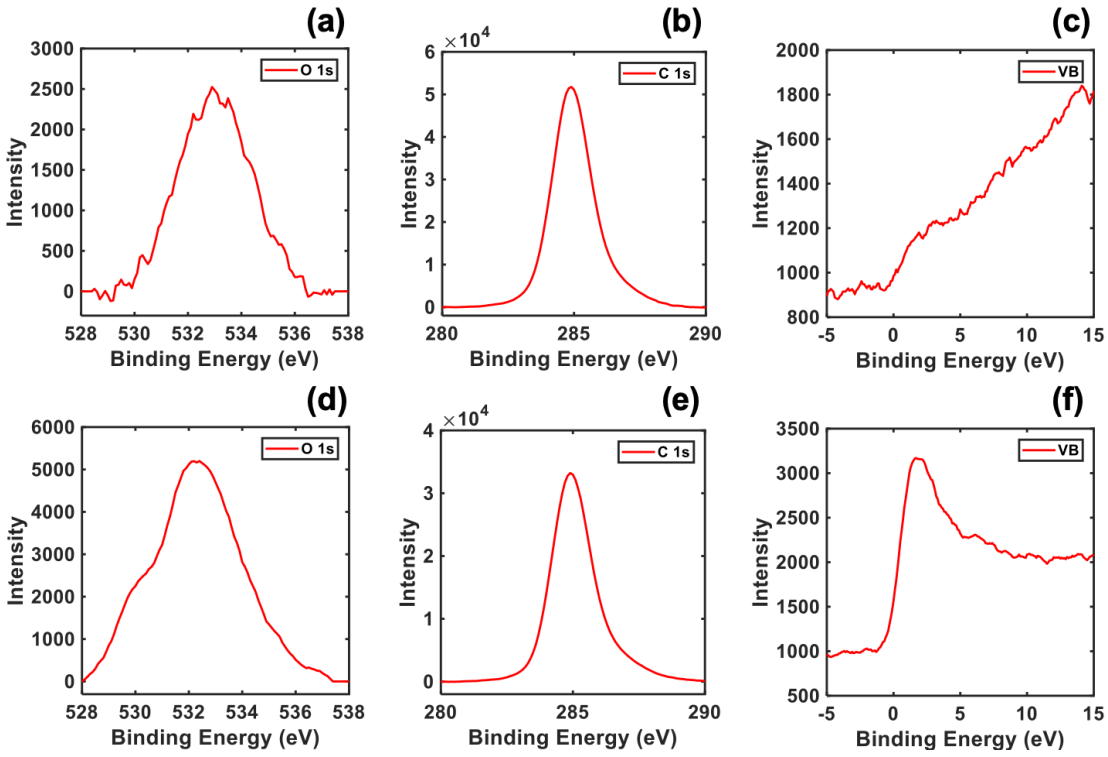


Figure 3.26: X-ray photoelectron spectroscopy of pristine HOPG and 7.5 nm nickel-on-HOPG annealed to ≈ 420 °C for 3.5 hours.

Again, HOPG was first cleaved, loaded, and outgassed *in situ* as previously described (Section 3.2.1). The copper doser was calibrated in the same way as the nickel system (Section 3.2.2), using Cu(100) as a calibration substrate. Figure 3.27 shows the final calibration intensity plot that resulting in a dosing rate of approximately 120 seconds per monolayer of copper.

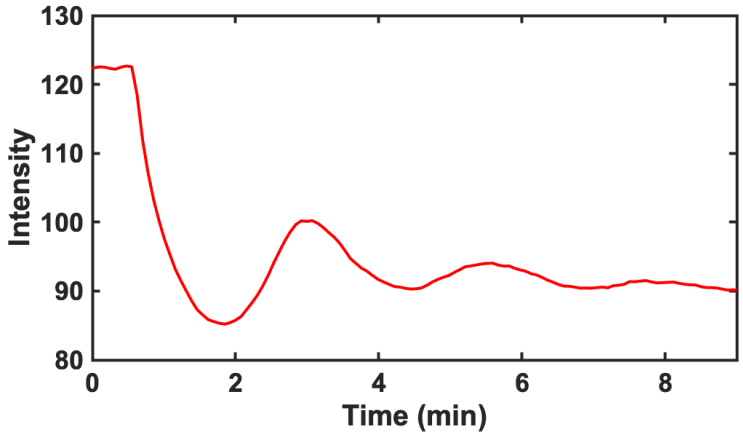


Figure 3.27: LEEM reflectivity as a function of start voltage used to calibrate copper dosing rate on Cu(100).

Using this dosing rate, approximately 25 layers of copper were deposited on HOPG at liquid nitrogen temperature. The sample temperature was then increased directly to the target of 350 °C, mirroring the previous experiments on nickel. Image acquisition began as soon as the image became reasonably stable but not yet at thermal equilibrium in order to capture as much of the dynamics as possible. Figure 3.28 shows representative images of copper on HOPG with increasing annealing time. The total annealing time from the first image to the last image was sixty minutes. There is almost no change in the surface morphology over time. Compared to the nickel-on-HOPG case, this is a marked contrast—there is no noticeable formation of surface features such as hillocks or valleys as easily identified in Figure 3.25. Since texture analysis microscopy algorithm relies on feature recognition, it cannot be applied similarly for copper due to this lack of observable features.

## 3.7 Conclusion

The spinodal dewetting phenomenon informs a deeper understanding of interfacial dynamics for thin films on various substrates. Systematic studies of few-nm nickel deposited on HOPG and annealed *in situ* enabled unprecedented real-time recordings of

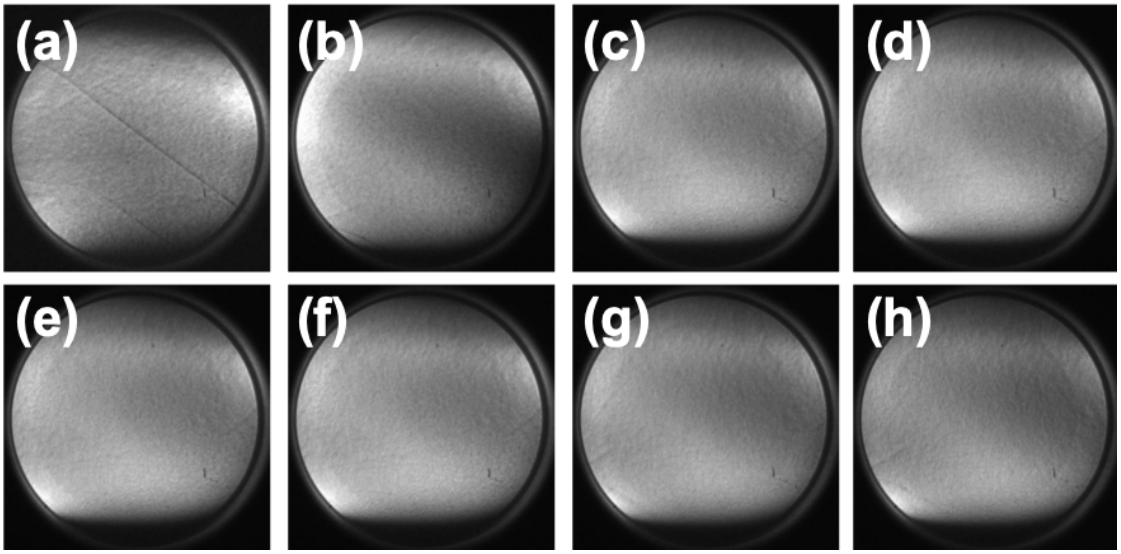


Figure 3.28: Representative LEEM images of ∼25 layers copper on HOPG annealed to 350 °C with increasing time.

changes in surface morphology after annealing. Extensive studies of software-assisted image analysis and application of texture analysis microscopy established a robust methodology for processing acquired images. The results of nickel-on-HOPG spinodal dewetting, along with parallel studies of copper-on-HOPG, are consistent with the results seen previously for low-pressure chemical vapor deposition of graphene with nickel and copper catalysts. In a broader sense, these studies provide fundamental insight on the limitations for evaluating catalyst thickness when pursuing metal-assisted graphene growth in low-pressure systems.

# Chapter 4

# Hydrogen plasma treatment of tungsten diselenide[1]

## 4.1 Introduction

TMDCs have gained significant traction in recent years due to their uniquely layer-dependent properties. These $MX_2$ trilayers—composed of two chalcogen ($X$) atoms and one metal ($M$) atom—have an $X$-$M$-$X$ sandwich structure and weak interlayer van der Waals bonding, enabling scalable, extremely thin ($\sim$6-7 Å) monolayers with no surface dangling bonds, particularly susceptible to induced defects [19, 132]. TMDCs such as tungsten diselenide ($WSe_2$) and molydenum disulfide ($MoS_2$) exhibit an indirect-to-direct band gap transition from bulk to monolayer form, offering a compelling alternative over graphene, which lacks an intrinsic bandgap [20–22]. As such, these materials are attractive for scalable, surface-sensitive device applications such as gas sensors and field-effect transistors (FETs) [133, 134].

Despite the rapid advances in proof-of-concept TMDC devices, device performance is still limited by fundamental issues such as large contact resistances [28–31]. To lower the contact resistance, intentional doping can be used to reduce the depletion width (*i.e.*, the Schottky barrier width), increasing the probability of electron tunneling [32]. To date, controllable methods for doping TMDCs *via* defect engineering are still in early stages of study [33].

Plasma treatment has been demonstrated as a way to induce defects in TMDCs. In contrast to other *ex situ* defect generation techniques such as electron beam irradiation

[1] A modified version of this work was published in Tosun, M.; Chan, L.; Amani, M.; Roy, T.; Ahn, G. H.; Taheri, P.; Carraro, C.; Ager, J. W.; Maboudian, R.; Javey, A. Air Stable n-Doping of $WSe_2$ by Anion Vacancy Formation with Mild Plasma Treatment. *ACS Nano* **2016**, *10* (7), 6853–6860. DOI: 10.1021/acsnano.6b02521.

or thermal annealing, plasma allows for high-energy reactive species to impinge on a sample without excessive heating. Previous studies have utilized oxygen, argon, and higher molecular weight plasmas (*e.g.*, $SF_6$, $CF_4$, $CHF_3$) to form new bonds [135–139], induce vacancies [140], or separate TMDC layers [139]. However, plasma-induced defect engineering with hydrogen ($H_2$) has not yet been explored. Given its low molecular weight, small atomic size, and common availability in semiconductor fabrication settings, hydrogen plasma is a promising candidate for controlled defect engineering of TMDCs such as $WSe_2$.

In this study, the effect of hydrogen plasma treatment on the material composition and device performance of $WSe_2$ is quantified using an *in situ* XPS and inductively coupled plasma (ICP) system. The investigation suggests the generation of selenium vacancies in $WSe_2$ and demonstrates n-doping up to degenerate levels. Finally, n-type FETs with plasma-treated contact regions are compared to control devices without treatment and exhibit more than two orders of magnitude lower contact resistances.

### 4.1.1 Hydrogen plasma treatment

An inductively coupled hydrogen plasma system was built to induce defects in bulk $WSe_2$ crystals (Figure 4.1a, 4.1b). To minimize contamination, the bulk crystal was first introduced into a load lock and pumped down to pressures of $<10^{-8}$ torr. A 200 mtorr charge of hydrogen gas (99.999%, Praxair) was then introduced into the load lock. Hydrogen plasma was imparted at a radio frequency 13.56 MHz and irradiated in three second increments at 3 W power. After the hydrogen plasma treatment, the sample was transferred (*in situ*) for XPS characterization (Figure 4.1c).

### 4.1.2 X-ray photoelectron spectroscopy analysis

X-ray photoemission spectroscopy (XPS) is a surface-sensitive technique used to investigate the effect of $H_2$ plasma on the material properties and chemical composition of the $WSe_2$ lattice. Compared to other ultra-high vacuum (UHV) surface characterization techniques, XPS is one of the most surface sensitive, as the mean free path of the electrons in solids is small (escape depth on the order of 1–10 nm) [141].

As shown in Figure 4.2a, in XPS a solid is irradiated with soft X-rays, leading to the emission of electrons *via* the photoelectric effect. The emitted electrons are detected and analyzed as a function of kinetic energy. The resulting spectrum, which plots the number of emitted electrons per energy interval, can provide information about the elements present in the sample, the chemical state of each element, and quantitative information about elemental composition.

In XPS analysis, the kinetic energy is simply given as the difference between the

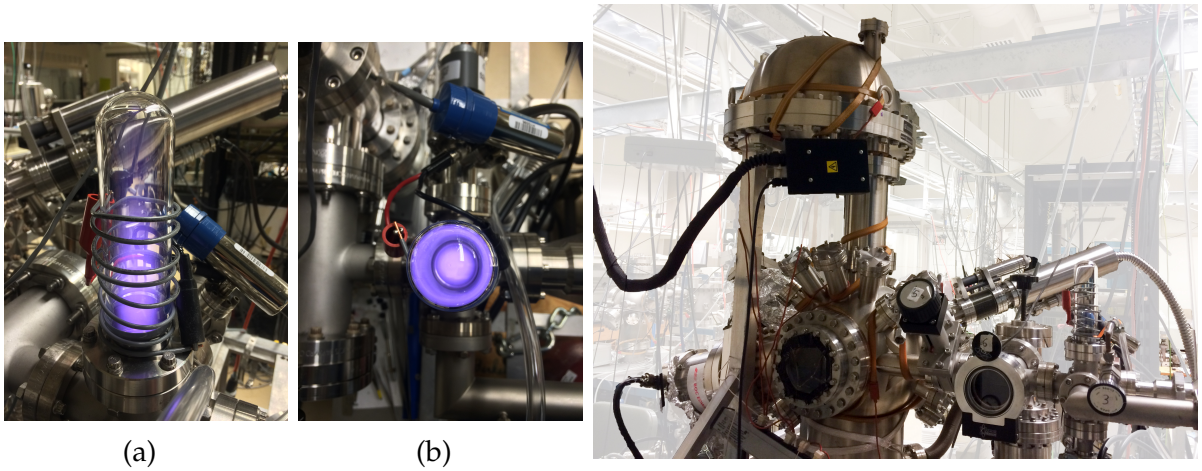

(a) (b) (c)

Figure 4.1: (a) Side and (b) top views of $H_2$ plasma chamber. (c) *In situ* XPS and plasma system

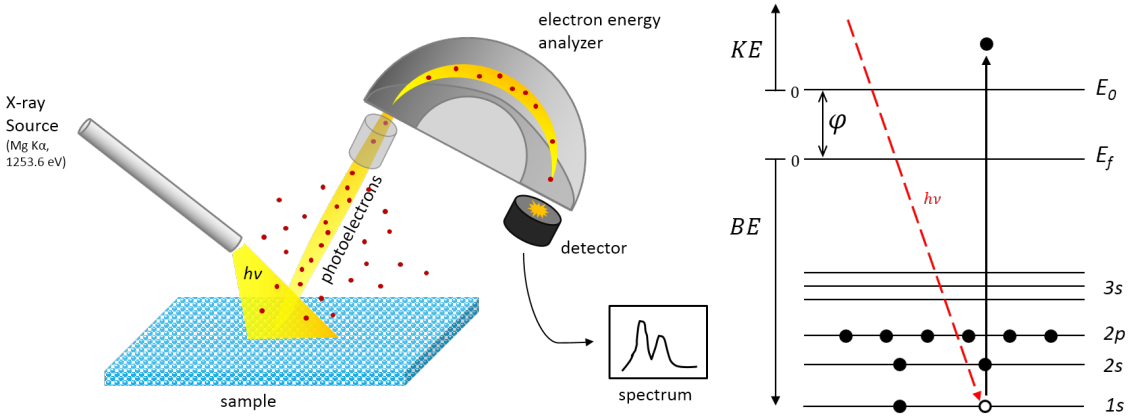


(a) (b)

Figure 4.2: Schematic of XPS system

incident energy ($h\nu$) and the sum of the binding energy (BE) and work function of the sample ($\phi_s$):

$$KE = h\nu - (BE + \phi_s) \tag{4.1}$$

The binding energy is defined as the energy of the atomic orbital from which an electron originates. While a sample's work function may be unknown, because the sample and spectrometer are both grounded, the relevant work function ends up being mathematically equivalent to the work function of the spectrometer.

In this study, the *in situ* XPS analysis was performed with an Omicron Dar400 achromatic Mg K$\alpha$ X-ray source and an Omicron EA 125 hemispherical analyzer operated at constant 50 eV pass energy. Bulk $WSe_2$ was loaded onto a sample holder and pumped down to ultra-high vacuum conditions ($P < 10^{-9}$) prior to measurement.

### 4.1.3 Field-effect transistor performance

To determine the effect of hydrogen plasma treatment on the contact resistance of $WSe_2$ FETs, two devices were fabricated on a single $WSe_2$ flake [142, 143]. $WSe_2$ was exfoliated on a heavily doped silicon wafer with 12 nm $ZrO_2$ as a back gate. In both devices, the contact regions were defined using e-beam lithography followed by 30 nm Ni metal deposition and liftoff using acetone. In the $H_2$-treated device, the contact regions were selectively treated with mild 140 mTorr 100 sccm $H_2$ plasma at 5 W for 5 s (Plasma-Therm PK-12 Reactive Ion Etch) prior to 30 nm Ni evaporation and liftoff in acetone. Both devices had the same channel width (L = 1 $\mu$m) and contact metal width.

## 4.2 XPS characterization

XPS was performed to investigate the effect of $H_2$ plasma on the chemical composition and material properties of $WSe_2$.

### 4.2.1 Effect of $H_2$ plasma on chemical composition

Figures 4.3a and 4.3b show the Se 3d and W 4f peaks prior to exposure and after 3, 6, and 12 seconds of exposure to $H_2$ plasma. With increasing exposure times, the binding energies increase. The upshift by 0.5 eV (after 12 seconds of treatment) indicates a Fermi level shift away from the valence band toward the conduction band edge which can be attributed to n-doping. This core-level shift toward higher binding energy is also consistent with previous studies of n-doped $WSe_2$ [143].

The Se 3d and W 4f peaks can also be used to quantify elemental ratios in the sample (*i.e.*, the Se:W atomic ratio). For homogenous samples such as bulk $WSe_2$, elemental

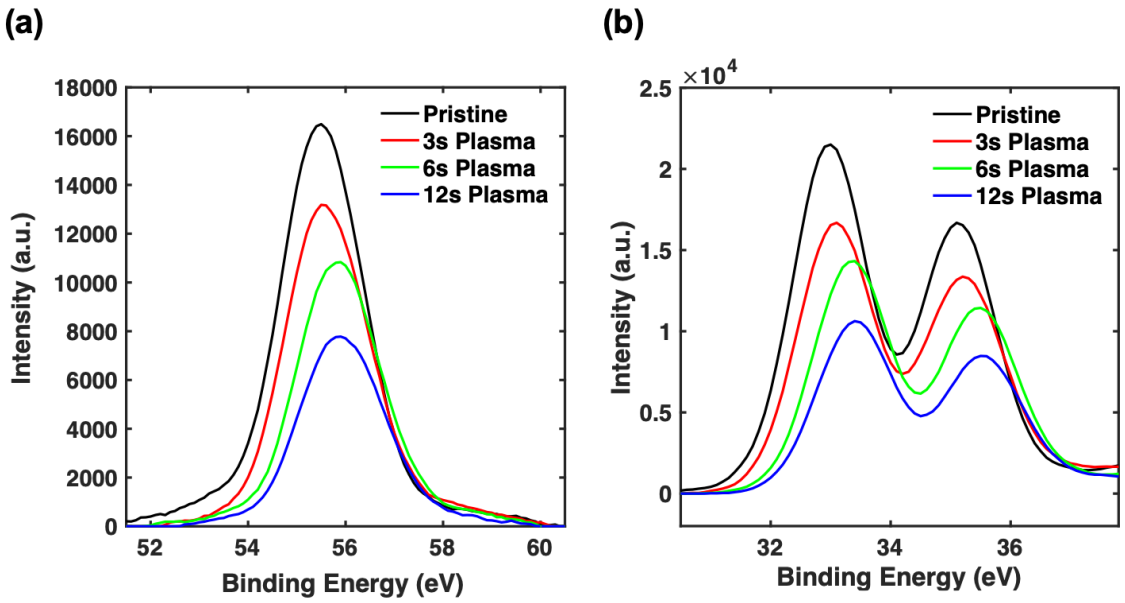


Figure 4.3: (a) Selenium 3d and (b) tungsten 4f XPS peaks of bulk $WSe_2$ as a function of $H_2$ plasma treatment time

ratios can be calculated by a simple relation between peak areas:

$$\frac{n_1}{n_2} = \frac{\left(\frac{I_1}{S_1}\right)}{\left(\frac{I_2}{S_2}\right)} \tag{4.2}$$

where $n_i$ is the number of atoms of element $i$, $I_i$ is the peak intensity (*i.e.*, peak area) after background subtraction, and $S_i$ is the angle-adjusted atomic sensitivity factor.

The peak areas for Se and W are quantified using regions of interest of 52.5–58.25 eV and 30.2–40.2. eV, respectively. Figure 4.4 shows the Se 3d and W 4f peaks and corresponding curve fits (70% Gaussian, 30% Lorentzian) after Shirley background subtraction [141]. These fits are used to determine the nominal peak areas prior to corrections.

For multi-layer systems, overlayer thickness leads to exponential attenuation of the photoelectron signal according to the Beer Lambert Law, $I_S = I_o e^{-d/\lambda}$, where $d$ is the overlayer depth and $\lambda$ is the mean free path of an electron through the material. In the case of multiple layers of stacked Se-W-Se, the final elemental ratio of Se/W is given by:

$$\frac{n_{Se}}{n_W} = \frac{\frac{I_{Se_1}}{S_{Se}(1-e^{-d_{Se}/\lambda_{Se}})} + \frac{I_{Se_2}}{S_{Se}(1-e^{-d_{Se}/\lambda_{Se}})(e^{-d_{Se}/\lambda_{Se}})(e^{-d_W/\lambda_W})}}{\frac{2I_W}{S_W(1-e^{-d_W/\lambda_W})(e^{-d_{Se}/\lambda_{Se}})}} \tag{4.3}$$

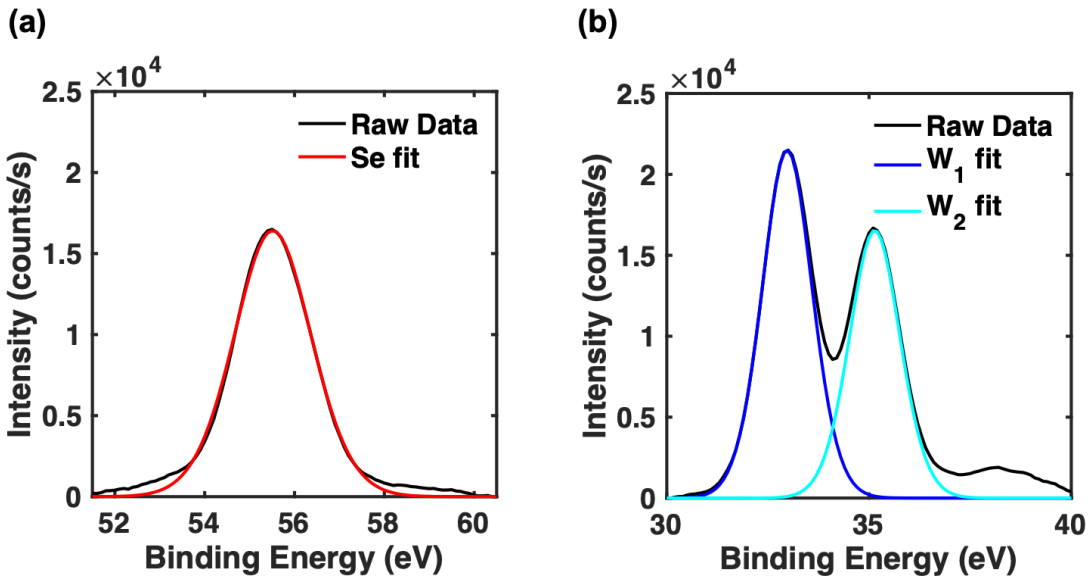


Figure 4.4: XPS spectra of (a) selenium 3d and (b) tungsten 4f peaks of bulk $WSe_2$ prior to $H_2$ plasma treatment with 70% Gaussian, 30% Lorentzian peak fits after Shirley background subtraction

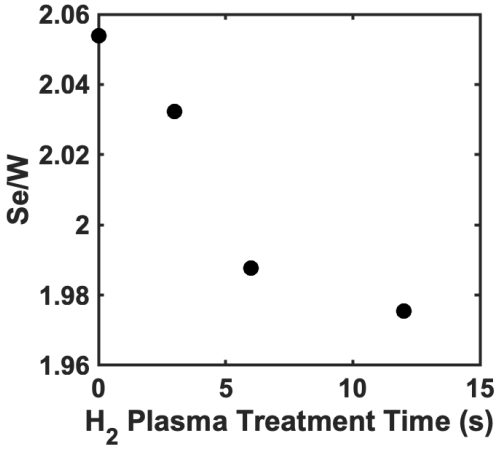


Figure 4.5: Se/W ratio of bulk $WSe_2$ with increasing $H_2$ plasma treatment times

Figure 4.5 shows the calculated ratio of the areas under the Se 3d and W 4f peaks as a function of plasma treatment time. Thicknesses $d$ are calculated based on material parameters, and $\lambda$ values are taken from predictive models from the NIST Electron Inelastic-Mean-Free-Path Database [144].

The final ratios are sensitive to the background subtraction parameters, particularly the region of interest in which background subtraction is carried out. Alternative choices of a constant Se region width ($+/-$ 0.5 eV) can translate into a uniform shift of the curve in Figure 4.5 of up to 5%, but will not affect the relative ratio decrease as a function of plasma exposure time. Different sources for the mean free path values can also introduce systematic error, but this similarly has a negligible effect on the overall trend.

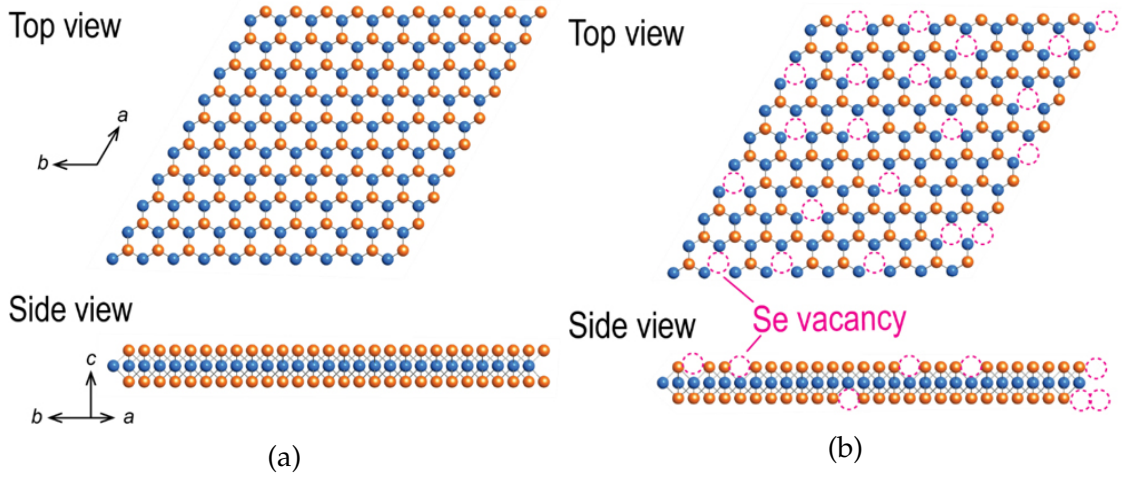


Figure 4.6: (a) Schematic of pristine $WSe_2$ flake (b) Schematic of $WSe_2$ flake after $H_2$ plasma treatment [142]

The Se/W ratio decreases with $H_2$ plasma time, indicating the loss of selenium atoms with increased exposure to hydrogen plasma. As depicted in Figure 4.6, the doping is induced by creating Se vacancies in the $WSe_2$ lattice.

### 4.2.2 Effect of $H_2$ plasma on doping concentration

To gain insight on the effect of $H_2$ plasma treatment on electron doping concentration, the XPS valence band spectra can be analyzed. Figure 4.7 shows the valence band spectra of $WSe_2$ with increasing $H_2$ plasma time. Linear extrapolation of the valence band edge tail, indicated by dotted lines in the figure, is used to extract the difference between the Fermi energy ($E_F$) and the valence band energy ($E_V$). As shown in Figure 4.7b, ($E_F - E_V$) evolves from 0.73 to 1.19 eV from 0–12 seconds of hydrogen plasma

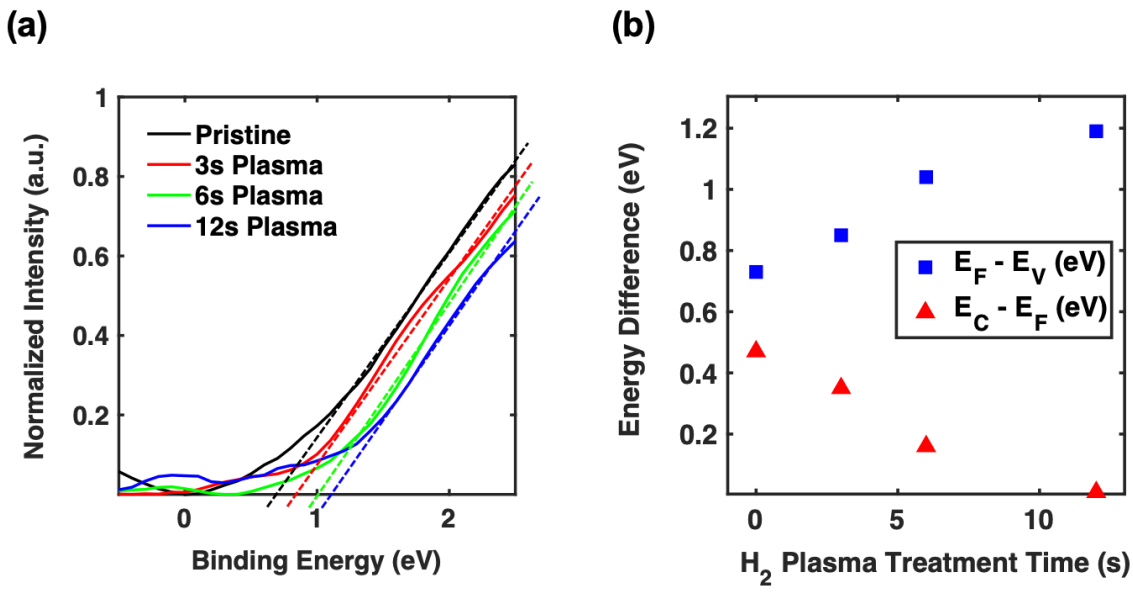


Figure 4.7: (a) Normalized valence band spectra of bulk $WSe_2$ with increasing $H_2$ plasma treatment time. (b) Energy difference calculated with values extracted from valence band spectra

treatment. Assuming a band gap value of 1.2 eV for multilayer $WSe_2$ [145], the difference between the conduction band energy ($E_C$) and the Fermi energy, ($E_C - E_F$) can also be calculated and is shown in the same plot (red triangles). At the longest $H_2$ plasma treatment time of 12 seconds, the difference between conduction band edge and the Fermi level is calculated to be 10 meV. This corresponds to $E_C - E_F < 3kT$ at room temperature, indicating controllable degenerate n-doping of $WSe_2$.

After determining the position of the Fermi level relative to the conduction band edge, the electron doping concentration ($N_D$) is calculated. The 3-D effective density of states ($N_C$) for electrons is calculated by using

$$N_C = 2\left(\frac{2\pi m_n kT}{h^2}\right)^{3/2} \tag{4.4}$$

where $m_n$ is the effective mass for electrons, $k$ is the Boltzmann constant, $T$ is the temperature, and $h$ is Planck's constant. At room temperature, by assuming $m_n$ to be 0.53 $m_0$ [146], $N_C$ is calculated to be 8.8 x $10^{18}$ $cm^{-3}$. Given this value and the energy difference calculated in Figure 4.7b, the doping concentration $N_D$ can be calculated using:

$$N_D = N_C e^{\frac{(E_F - E_C)}{kT}} \tag{4.5}$$

and is plotted in Figure 4.8. Note that this equation only applies to shorter $H_2$ plasma treatment times (<12 s), since the Boltzmann approximation does not apply at degenerate levels. Given that the boundary condition for degenerate doping, $E_C - E_F = 3kT$, results in a doping concentration of 4 x $10^{17}$ $cm^{-3}$, $N_D$ is assumed to be greater than 4 x $10^{17}$ $cm^{-3}$ at room temperature. As shown in Figure 4.8, $N_D$ shows a monotonic increase with $H_2$ plasma treatment time.

## 4.3 n-FET performance

Contact resistance ($R_c$) values were compared for the control and $H_2$ plasma treated n-FETs following the fabrication steps in Section 4.1.3 (Figure 4.9a). As shown in Figure 4.9b, the total resistance of the channel and the contacts can be fitted to an exponentially decaying function. The asymptote at large $V_{GS}$ is defined as $2R_C$ as the channel resistance becomes negligible. The contact resistance for the $H_2$-plasma-treated device was 8 $k\Omega \cdot \mu m$, more than 2 orders of magnitude lower than for the control devices. While this $R_C$ value is on the same order of magnitude as $WSe_2$ FETs fabricated using alternative ($NO_2$, K) doping schemes [143, 147], $H_2$ plasma treatment has a marked advantage for its stability in air and common availability in semiconductor fabrication.

To further determine if plasma treatment indeed induced vacancies in the $WSe_2$ lattice, He plasma treatment was also tested on $WSe_2$ FETs fabricated on the same flake.

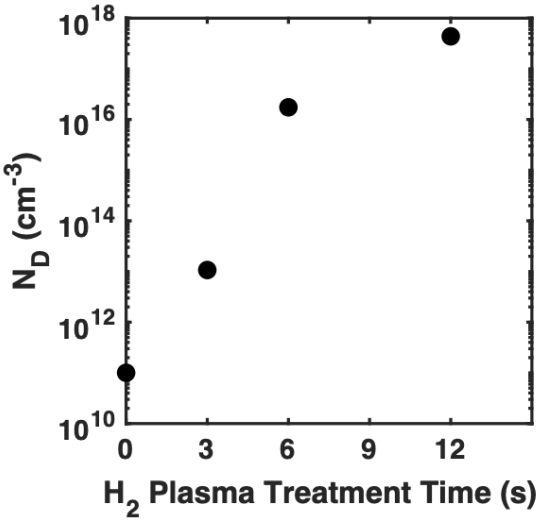


Figure 4.8: Doping concentration in bulk $WSe_2$ with increasing $H_2$ plasma treatment time

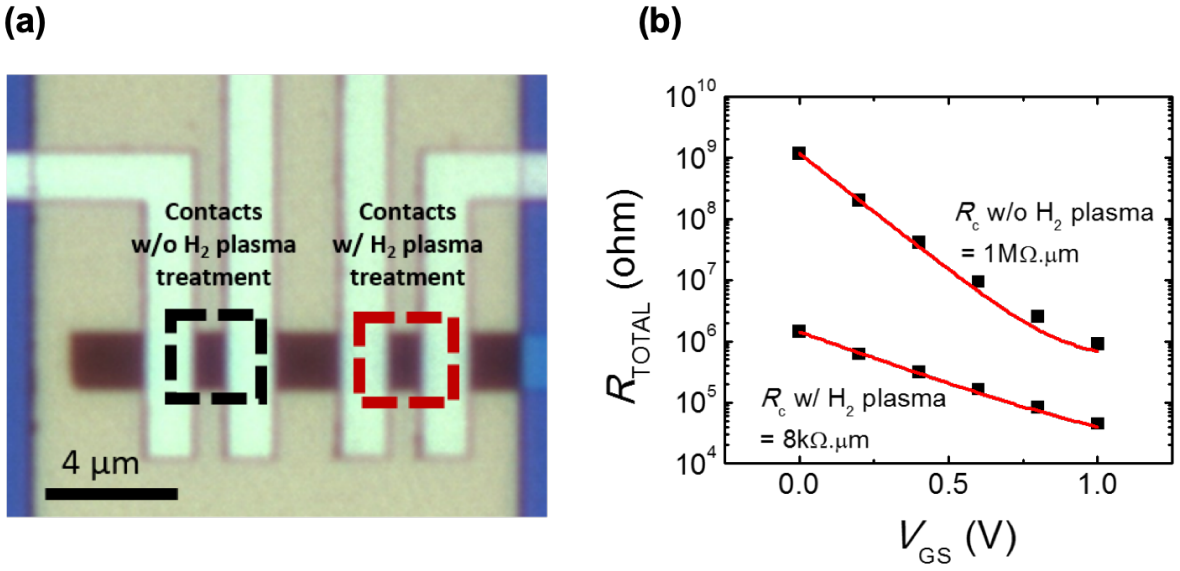


Figure 4.9: (a) Optical image of control (left) and $H_2$-plasma-treated (right) field-effect transistors fabricated on single $WSe_2$ flake (b) n-FET contact resistance with and without $H_2$ plasma treatment [142]

Following He-plasma treatment, the FETs had an ON current improvement of 3 orders of magnitude and also showed n-type transfer characteristics, suggesting that the doping indeed results from the formation of Se vacancies rather than a chemical reaction to $H_2$ plasma.

The electrical performance of $WSe_2$ n-FETs is impacted by the efficacy of electron tunneling through the Schottky barrier width. For a prototypical FET device, the depletion width $W_{dep}$ is a function of the doping concentration $N_D$, semiconductor permittivity $\epsilon_s$, built-in potential $\phi_{bi}$, and charge $q$ [148]:

$$W_{dep} = \sqrt{\frac{2\epsilon_s \phi_{bi}}{qN_D}} \tag{4.6}$$

It follows that $H_2$ plasma treatment—which increases the doping concentration $N_D$—decreases the depletion width $W_{dep}$. As such, the probability of electron tunneling through the Schottky barrier increases and this results in a reduced metal contact resistance.

A typical TMDC–metal interface is separated by a van der Waals gap due to the lack of dangling bonds on the ideal TMDC surface [39]. In the ideal case, this contributes to an additional tunneling barrier. However, when Se vacancies are created using plasma treatment, dangling bonds and defects are introduced; these help disrupt the interface and facilitate bonding between the metal and TMDC interface.

Together, this increase in doping concentration and the generation of induced defects creates a diminished Schottky barrier width, increasing the probability of electron tunneling and enabling a novel method for lowering the contact resistance of $WSe_2$ in FET devices.

## 4.4 Conclusion

This study demonstrates the effect of hydrogen plasma treatment on the material properties of $WSe_2$. Selenium vacancies selectively form in the $WSe_2$ lattice, leading to degenerate n-doping with extended plasma treatment times. $WSe_2$ n-FETs are fabricated and demonstrate two orders of magnitude decrease in contact resistance after hydrogen plasma treatment.

Defect engineering of TMDCs is a topic of increasing importance as devices come closer to realization. This investigation demonstrates how controlled modifications to device interfaces can help improve device properties. A deeper understanding of the defect formation of TMDCs can enable intelligent design of scalable electronics and chemical sensing devices. Since the time of these studies, additional groups have continued to work on plasma treatment and other doping methods [33–36]. Continuing work offers a

cumulative assortment of alternatives and learning points; many opportunities remain for further exploration.

# Chapter 5

# Conclusion

Two-dimensional materials are in a golden age of research; however, challenges are growing increasingly formidable as progress evolves from proof-of-concept devices to consumer products. This work focused on two particular classes of 2DMs: graphene and TMDCs. Two barriers to high-performance FETs—the transfer step requirement and the high 2DM–metal contact resistance—were investigated from synthesis and defect engineering angles.

To address the non-ideal transfer step required to move metal-catalyzed CVD-graphene onto target insulating substrates, transfer-free CVD graphene synthesis was explored and optimized. Adapting from previous work and using a two-step annealing process, bottom-layer graphene was successfully achieved from low-pressure CVD with gaseous methane as a carbon precursor. Using nickel as a catalyst, defect-minimized regions of monolayer graphene with $> 45$ % coverage were obtained. Using copper as a catalyst, uniform, 2–3 layer graphene with complete coverage was obtained. The results validated that nickel and copper catalysts behave differently (as in top-layer graphene growth) and suggested contrasting mechanistic regimes for bottom-layer graphene growth.

To better understand the differences between nickel and copper in metal-catalyzed graphene growth, real-time, real-space low-energy electron microscopy (LEEM) was used to study spinodal dewetting of thin metal films on HOPG. Image processing techniques and texture analysis microscopy were adapted and applied to address imaging limitations of LEEM and obtain quantitative interaction parameters.

Finally, the high contact resistance of TMDCs in field-effect transistors was addressed by using mild hydrogen plasma treatment to systematically dope $WSe_2$ in contact regions. XPS was used to identify and quantify the n-doping of $WSe_2$ with increasing plasma treatment times. The plasma treatment selectively induced selenium vacancies and lowered contact resistances in field effect transistors by more than two orders of magnitude.

These studies add to the growing set of literature informing judicious selection of process parameters for high-performance electronics applications. Moving forward, investigations on transfer-free growth would be well-served by analogous *in situ* studies of spinodal dewetting on other metals (*i.e.*, beyond nickel and copper) on HOPG. As defect engineering of 2DMs continues to advance, fundamental studies exploring the physical, chemical, and electronic consequences and mechanisms of doping/vacancy formation would add considerable depth. Needless to say, rapid progress in 2DM research has been encouraging to date; continued emphasis on fundamental studies will behoove the field as industry leans into 2DMs and pushes towards scalable production of beyond-silicon electronics for multifarious applications.

# Bibliography


(1) Novoselov, K. S.; Jiang, D.; Schedin, F.; Booth, T. J.; Khotkevich, V. V.; Morozov, S. V.; Geim, a. K. *Proceedings of the National Academy of Sciences of the United States of America* **2005**, *102*, 10451–10453.

(2) Novoselov, K. S.; Fal'Ko, V. I.; Colombo, L.; Gellert, P. R.; Schwab, M. G.; Kim, K. *Nature* **2012**, *490*, 192–200.

(3) Chhowalla, M.; Shin, H. S.; Eda, G.; Li, L.-J.; Loh, K. P.; Zhang, H. *Nature Chemistry* **2013**, *5*, 263–75.

(4) Ferrari, A. C.; Katsnelson, M.; Vandersypen, L.; Loiseau, A.; Morandi, V.; Tredicucci, A.; Williams, G. M.; Hong, H. *Nanoscale* **2015**, *7*, 4598–4810.

(5) Das, S.; Kim, M.; Lee, J.-w.; Choi, W. *Critical Reviews in Solid State and Materials Sciences* **2014**, *39*, 231–252.

(6) Mas-Ballesté, R.; Gómez-Navarro, C.; Gómez-Herrero, J.; Zamora, F. *Nanoscale* **2011**, *3*, 20–30.

(7) Zhu, Y.; Murali, S.; Cai, W.; Li, X.; Suk, J. W.; Potts, J. R.; Ruoff, R. S. *Advanced Materials* **2010**, *22*, 3906–3924.

(8) Slonczewski, J.; Weiss, P. *Physical Review* **1958**, *109*, 272.

(9) Morozov, S. V.; Novoselov, K. S.; Katsnelson, M. I.; Schedin, F.; Elias, D. C.; Jaszczak, J. A.; Geim, A. K. *Physical Review Letters* **2008**, *100*, 016602.

(10) Lee, C.; Wei, X.; Kysar, J. W.; Hone, J. *Science* **2008**, *321*, 385–388.

(11) Balandin, A. A. Thermal properties of graphene and nanostructured carbon materials., 2011.

(12) Geim, A. K.; Novoselov, K. S. *Nature Materials* **2007**, *6*, 183–191.

(13) Lemme, M. *Solid State Phenomena* **2009**, *156-158*, 499–509.

(14) Mattevi, C.; Kim, H.; Chhowalla, M. *J. Mater. Chem.* **2011**, *21*, 3324–3334.

(15) Choi, W.; Lahiri, I.; Seelaboyina, R.; Kang, Y. S. *Critical Reviews in Solid State and Materials Sciences* **2010**, *35*, 52–71.

(16) Zhang, Y.; Zhang, L.; Zhou, C. *Accounts of Chemical Research* **2013**, *46*, 2329–2339.

(17) Lee, H. C.; Liu, W.-W.; Chai, S.-P.; Mohamed, A. R.; Aziz, A.; Khe, C.-S.; Hidayah, N. M. S.; Hashim, U. *RSC Adv.* **2017**, *7*, 15644–15693.

(18) Hofmann, S.; Braeuninger-Weimer, P.; Weatherup, R. S. *Journal of Physical Chemistry Letters* **2015**, *6*, 2714–2721.

(19) Radisavljevic, B.; Radenovic, A.; Brivio, J.; Giacometti, V.; Kis, A. *Nature Nanotechnology* **2011**, *6*, 147–150.

(20) Novoselov, K. S.; Geim, A. K.; Morozov, S. V.; Jiang, D.; Zhang, Y.; Dubonos, S. V.; Grigorieva, I. V.; Firsov, A. A. *Science* **2004**, *306*, 666–669.

(21) Ding, Y.; Wang, Y.; Ni, J.; Shi, L.; Shi, S.; Tang, W. *Physica B: Condensed Matter* **2011**, *406*, 2254–2260.

(22) Mak, K. F.; Lee, C.; Hone, J.; Shan, J.; Heinz, T. F. *Physical Review Letters* **2010**, *105*, DOI: 10.1103/PhysRevLett.105.136805.

(23) Yuan, H.; Wang, H.; Cui, Y. *Accounts of Chemical Research* **2015**, *48*, 81–90.

(24) Najmaei, S.; Yuan, J.; Zhang, J.; Ajayan, P.; Lou, J. *Accounts of Chemical Research* **2015**, *48*, 31–40.

(25) Shi, Y.; Li, L.-j. *Chemical Society Reviews* **2014**, *44*, 2744–2756.

(26) Plutnar, J.; Pumera, M.; Sofer, Z. *Journal of Materials Chemistry C* **2018**, DOI: 10.1039/C8TC00463C.

(27) Chen, X.; Wu, B.; Liu, Y. *Chem. Soc. Rev. Chem. Soc. Rev* **2016**, *45*, 2057–2074.

(28) Baugher, B. W. H.; Churchill, H. O. H.; Yang, Y.; Jarillo-Herrero, P. *Nature Nanotechnology* **2014**, *9*, 262–7.

(29) Ross, J. S.; Klement, P.; Jones, A. M.; Ghimire, N. J.; Yan, J.; Mandrus, D. G.; Taniguchi, T.; Watanabe, K.; Kitamura, K.; Yao, W.; Cobden, D. H.; Xu, X. *Nature Nanotechnology* **2014**, *9*, 268–72.

(30) Allain, A.; Kang, J.; Banerjee, K.; Kis, A. *Nature Materials* **2015**, *14*, 1195–1205.

(31) Xu, Y.; Cheng, C.; Du, S.; Yang, J.; Yu, B.; Luo, J.; Yin, W.; Li, E.; Dong, S.; Ye, P.; Duan, X. *ACS Nano* **2016**, acsnano.6b01842.

(32) Tosun, M.; Chan, L.; Amani, M.; Roy, T.; Ahn, G. H.; Taheri, P.; Carraro, C.; Ager, J. W.; Maboudian, R.; Javey, A. *ACS Nano* **2016**, acsnano.6b02521.

(33) Lin, Z.; Carvalho, B. R.; Kahn, E.; Lv, R.; Rao, R.; Terrones, H.; Pimenta, M. A.; Terrones, M. *2D Materials* **2016**, *3*, 022002.

(34) Zhao, Y.; Xu, K.; Pan, F.; Zhou, C.; Zhou, F.; Chai, Y. *Advanced Functional Materials* **2017**, *27*, DOI: 10.1002/adfm.201603484.

(35) Luo, P.; Zhuge, F.; Zhang, Q.; Chen, Y.; Lv, L.; Huang, Y.; Li, H.; Zhai, T. *Nanoscale Horizons* **2019**, *4*, 26–51.

(36) Wang, Y.; Kim, J. C.; Wu, R. J.; Martinez, J.; Song, X.; Yang, J.; Zhao, F.; Mkhoyan, A.; Jeong, H. Y.; Chhowalla, M. *Nature* **2019**, *568*, 70–74.

(37) Theis, T. N.; Solomon, P. M. It's time to reinvent the transistor!, 2010.

(38) Frank, D. J.; Taur, Y.; Wong, H.-S. P. *Generalized Scale Length for Two-Dimensional Effects in MOSFET's*; tech. rep. 10; 1998, p 385.

(39) Schwierz, F. *Nature Nanotechnology* **2010**, *5*, 487–496.

(40) Muñoz, R.; Gómez-Aleixandre, C. *Chemical Vapor Deposition* **2013**, *19*, 297–322.

(41) Habib, M.; Liang, T.; Yu, X.; Pi, X.; Liu, Y.; Xu, M. *Reports on Progress in Physics* **2018**, *81*, DOI: 10.1088/1361-6633/aa9bbf.

(42) Tan, H.; Wang, D.; Guo, Y. *Coatings* **2018**, *8*, 40.

(43) Ning, J.; Wang, D.; Chai, Y.; Feng, X.; Mu, M.; Guo, L.; Zhang, J.; Hao, Y. *Nanotechnology* **2017**, *28*, 284001.

(44) Ulman, A. *Chemical Reviews* **1996**, *96*, 1533–1554.

(45) Prashar, D. *International Journal of ChemTech Research* **2012**, *4*, 258–265.

(46) Schwartz, D. K. *Annual Review of Physical Chemistry* **2001**, *52*, 107–137.

(47) Shin, H. J.; Choi, W. M.; Yoon, S. M.; Han, G. H.; Woo, Y. S.; Kim, E. S.; Chae, S. J.; Li, X. S.; Benayad, A.; Loc, D. D.; Gunes, F.; Lee, Y. H.; Choi, J. Y. *Advanced Materials* **2011**, *23*, 4392–4397.

(48) Yang, G.; Kim, H.-Y.; Jang, S.; Kim, J. *ACS Applied Materials & Interfaces* **2016**, *8*, 27115–27121.

(49) Turchanin, A.; Weber, D.; Büenfeld, M.; Kisielowski, C.; Fistul, M. V.; Efetov, K. B.; Weimann, T.; Stosch, R.; Mayer, J.; Gölzhäuser, A. *ACS Nano* **2011**, *5*, 3896–3904.

(50) Byun, S. J.; Lim, H.; Shin, G. Y.; Han, T. H.; Oh, S. H.; Ahn, J. H.; Choi, H. C.; Lee, T. W. *Journal of Physical Chemistry Letters* **2011**, *2*, 493–497.

(51) Yan, Z.; Peng, Z.; Sun, Z.; Yao, J.; Zhu, Y.; Liu, Z.; Ajayan, P. M.; Tour, J. M. *ACS Nano* **2011**, *5*, 8187–8192.

(52) Peng, Z.; Yan, Z.; Sun, Z.; Tour, J. M. *ACS Nano* **2011**, *5*, 8241–8247.

(53) Pan, G.; Li, B.; Heath, M.; Horsell, D.; Wears, M. L.; Al Taan, L.; Awan, S. *Carbon* **2013**, *65*, 349–358.

(54) Xiong, W.; Zhou, Y. S.; Jiang, L. J.; Sarkar, A.; Mahjouri-Samani, M.; Xie, Z. Q.; Gao, Y.; Ianno, N. J.; Jiang, L.; Lu, Y. F. *Advanced Materials* **2013**, *25*, 630–634.

(55) Zhuo, Q. Q.; Wang, Q.; Zhang, Y. P.; Zhang, D.; Li, Q. L.; Gao, C. H.; Sun, Y. Q.; Ding, L.; Sun, Q. J.; Wang, S. D.; Zhong, J.; Sun, X. H.; Lee, S. T. *ACS Nano* **2015**, *9*, 594–601.

(56) Reina, A.; Thiele, S.; Jia, X.; Bhaviripudi, S.; Dresselhaus, M. S.; Schaefer, J. A.; Kong, J. *Nano Res* **2009**, *2*, 509–516.

(57) McNerny, D. Q.; Viswanath, B.; Copic, D.; Laye, F. R.; Prohoda, C.; Brieland-Shoultz, A. C.; Polsen, E. S.; Dee, N. T.; Veerasamy, V. S.; Hart, A. J. *Scientific Reports* **2014**, *4*, 1–9.

(58) Baraton, L.; He, Z. B.; Lee, C. S.; Cojocaru, C. S.; Châtelet, M.; Maurice, J.-L.; Lee, Y. H.; Pribat, D. *EPL (Europhysics Letters)* **2011**, *96*, 46003.

(59) Singleton, M.; Nash, P. *Bulletin of Alloy Phase Diagrams* **1989**, *10*, 121–126.

(60) Lander, J. J.; Kern, H. E.; Beach, A. L. *Journal of Applied Physics* **1952**, *23*, DOI: 10.1063/1.3318263.

(61) Kim, H.; Saiz, E.; Chhowalla, M.; Mattevi, C. *New Journal of Physics* **2013**, *15*, DOI: 10.1088/1367-2630/15/5/053012.

(62) Casiraghi, C.; Hartschuh, A.; Lidorikis, E.; Qian, H.; Harutyunyan, H.; Gokus, T.; Novoselov, K. S.; Ferrari, A. C. *Nano Letters* **2007**, *7*, 2711–2717.

(63) Ferrari, A. C.; Meyer, J. C.; Scardaci, V.; Casiraghi, C.; Lazzeri, M.; Mauri, F.; Piscanec, S.; Jiang, D.; Novoselov, K. S.; Roth, S.; Geim, A. K. *Physical Review Letters* **2006**, *97*, 1–4.

(64) Ferrari, A. C. *Solid State Communications* **2007**, *143*, 47–57.

(65) Graf, D.; Molitor, F.; Ensslin, K.; Stampfer, C.; Jungen, A.; Hierold, C.; Wirtz, L. *Nano Letters* **2007**, *7*, 238–242.

(66) Su, C. Y.; Lu, A. Y.; Wu, C. Y.; Li, Y. T.; Liu, K. K.; Zhang, W.; Lin, S. Y.; Juang, Z. Y.; Zhong, Y. L.; Chen, F. R.; Li, L. J. *Nano Letters* **2011**, *11*, 3612–3616.

(67) Lee, P. S.; Mangelinck, D.; Pey, K. L.; Shen, Z.; Ding, J.; Osipowicz, T.; See, A. *Electrochemical and Solid-State Letters* **2000**, *3*, 153–155.

(68) Donthu, S. K.; Tripathy, S.; Chi, D. Z.; Chua, S. J. *Journal of Raman Spectroscopy* **2004**, *35*, 536–540.

(69) Bhaskaran, M.; Sriram, S.; Perova, T. S.; Ermakov, V.; Thorogood, G. J.; Short, K. T.; Holland, A. S. *Micron* **2009**, *40*, 89–93.

(70) Huet, B.; Raskin, J.-P. *Chemistry of Materials* **2017**, *29*, 3431–3440.

(71) Scherrer, P. *Nachrichten von der Gesellschaft der Wissenschaften zu Göttingen, Mathematisch-Physikalische Klasse* **1918**, 98–100.

(72) Patterson, A. L. *The Scherrer Formula for X-Ray Particle Size Determination*; tech. rep.; 1939.

(73) Ibrahim, A.; Akhtar, S.; Atieh, M.; Karnik, R.; Laoui, T. *Carbon* **2015**, *94*, 369–377.

(74) Shu, H.; Tao, X.-M.; Ding, F. *Nanoscale* **2015**, *7*, 1627–1634.

(75) Zhang, W.; Wu, P.; Li, Z.; Yang, J. *Journal of Physical Chemistry C* **2011**, *115*, 17782–17787.

(76) Cabrero-Vilatela, A.; Weatherup, R. S.; Braeuninger-Weimer, P.; Caneva, S.; Hofmann, S. *Nanoscale* **2016**, *8*, 2149–2158.

(77) Fang, H. et al. *Proceedings of the National Academy of Sciences of the United States of America* **2014**, *111*, 6198–202.

(78) Losurdo, M.; Giangregorio, M. M.; Capezzuto, P.; Bruno, G. *Physical Chemistry Chemical Physics* **2011**, *13*, 20836.

(79) Weatherup, R. S. et al. *Journal of the American Chemical Society* **2014**, *136*, 13698–13708.

(80) López, G. A.; Mittemeijer, E. J. *Scripta Materialia* **2004**, *51*, 1–5.

(81) Celebi, K.; Cole, M. T.; Choi, J. W.; Wyczisk, F.; Legagneux, P.; Rupesinghe, N.; Robertson, J.; Teo, K. B. K.; Park, H. G. *Nano Letters* **2013**, *13*, 967–974.

(82) Bhaviripudi, S.; Jia, X.; Dresselhaus, M. S.; Kong, J. *Nano Letters* **2010**, *10*, 4128–4133.

(83) Wang, S.; Hibino, H.; Suzuki, S.; Yamamoto, H. *Chemistry of Materials* **2016**, *28*, 4893–4900.

(84) Kato, T.; Hatakeyama, R. *ACS Nano* **2012**, *6*, 8508–8515.

(85) Vrij, A. *Discussions of the Faraday Society* **1966**, *42*, 23.

(86) Vrij, A.; Overbeek, J. T. G. *Journal of the American Chemical Society* **1968**, *90*, 3074–3078.

(87) Reiter, G. *Langmuir* **1993**, *9*, 1344–1351.

(88) Seemann, R.; Herminghaus, S.; Jacobs, K. *Physical Review Letters* **2001**, *86*, 5534–5537.

(89) Herminghaus, S. *Science* **1998**, *282*, 916–919.

(90) Wyart, F. B.; Martin, P.; Redon, C. *J. F. Physico Chem. hydrodyn* **1993**, *9*, 3682–3690.

(91) Xie, R.; Karim, A.; Douglas, J. F.; Han, C. C.; Weiss, R. A. *Physical Review Letters* **1998**, *81*, 1251–1254.

(92) Wyart, F. B.; Daillant, J. *Canadian Journal of Physics* **1990**, *68*, 1084–1088.

(93) Seemann, R.; Herminghaus, S.; Jacobs, K. *Journal of Physics Condensed Matter* **2001**, *13*, 4925–4938.

(94) Seemann, R.; Herminghaus, S.; Neto, C.; Schlagowski, S.; Podzimek, D.; Konrad, R.; Mantz, H.; Jacobs, K. *Journal of Physics Condensed Matter* **2005**, *17*, DOI: 10.1088/0953-8984/17/9/001.

(95) Bischof, J.; Scherer, D.; Herminghaus, S.; Leiderer, P. *Physical Review Letters* **1996**, *77*, 1536–1539.

(96) Reiter, G. *Phys. Rev. Lett.* **1992**, *68*, 75–78.

(97) Cahn, J. W.; Hilliard, J. E. *Kinetics of Phase Change. I General Theory The Journal of Chemical Physics* **1958**, *28*, 333.

(98) Cahn, J. W. *Acta Metallurgica* **1961**, *9*, 795–801.

(99) Cahn, J. W. *Acta Metallurgica* **1962**, *10*, 907–913.

(100) Ruckenstein, E.; Jain, R. K. *Journal of the Chemical Society, Faraday Transactions 2: Molecular and Chemical Physics* **1974**, *70*, 132–147.

(101) Singh, S. P. *Advances in Condensed Matter Physics* **2011**, *2011*, DOI: 10.1155/2011/526397.

(102) McKeown, J. T.; Roberts, N. A.; Fowlkes, J. D.; Wu, Y.; Lagrange, T.; Reed, B. W.; Campbell, G. H.; Rack, P. D. *Langmuir* **2012**, *28*, 17168–17175.

(103) Krishna, H.; Sachan, R.; Strader, J.; Favazza, C.; Khenner, M.; Kalyanaraman, R. *Nanotechnology* **2010**, *21*, DOI: 10.1088/0957-4484/21/15/155601.

(104) Fuentes-Cabrera, M.; Rhodes, B. H.; Fowlkes, J. D.; López-Benzanilla, A.; Terrones, H.; Simpson, M. L.; Rack, P. D. *Physical Review E - Statistical, Nonlinear, and Soft Matter Physics* **2011**, *83*, DOI: 10.1103/PhysRevE.83.041603.

(105) Trice, J.; Thomas, D.; Favazza, C.; Sureshkumar, R.; Kalyanaraman, R. *Physical Review B - Condensed Matter and Materials Physics* **2007**, *75*, 1–15.

(106) Amarandei, G.; O'Dwyer, C.; Arshak, A.; Corcoran, D. *Soft Matter* **2013**, *9*, 2695.

(107) Burke, S. A.; Topple, J. M.; Grütter, P. *Journal of Physics: Condensed Matter* **2009**, *21*, 423101.

(108) Maekawa, Y.; Shibuta, Y. *Chemical Physics Letters* **2016**, *658*, 30–36.

(109) Held, G. *Bunsen Magazin* **2010**, *12*, 124–131.

(110) Ferralis, N.; Pussi, K.; Finberg, S. E.; Smerdon, J.; Lindroos, M.; McGrath, R.; Diehl, R. D. *Physical Review B* **2004**, *70*, 245407.

(111) Hibino, H.; Kageshima, H.; Maeda, F.; Nagase, M.; Kobayashi, Y.; Yamaguchi, H. *Physical Review B - Condensed Matter and Materials Physics* **2008**, *77*, DOI: 10.1103/PhysRevB.77.075413.

(112) Ohta, T.; El Gabaly, F.; Bostwick, A.; McChesney, J. L.; Emtsev, K. V.; Schmid, A. K.; Seyller, T.; Horn, K.; Rotenberg, E. *New Journal of Physics* **2008**, *10*, DOI: 10.1088/1367-2630/10/2/023034.

(113) Davis, L. E.; MacDonald, N. C.; Palmberg, P. W.; Riach, G. E.; Weber, R. E., *Handbook of Auger Electron Spectroscopy*, 2nd Ed.; Physical Electronics Division: Eden Prairie, Minnesota, 1976.

(114) Lesiak, B.; Ozek, P.; Jabloński, A.; Jóźwik, A. *Surface and Interface Analysis* **1986**, *8*, 121–126.

(115) Omega Engineering, I. Transactions in Measurement and Control: Vol. 1., Stamford, CT, 1998.

(116) Rougemaille, N.; Ndiaye, A. T.; Coraux, J.; Vo-Van, C.; Fruchart, O.; Schmid, A. K. *Applied Physics Letters* **2012**, *101*, DOI: 10.1063/1.4749818.

(117) Sinharoy, S.; Smith, M.; Levenson, L. L. *Journal of Vacuum Science and Technology* **1977**, *14*, 475–478.

(118) Coad, J. P.; Riviere, J. C. *Surface Science* **1971**, *25*, 609–624.

(119) Sinharoy, S.; Smith, M.; Levenson, L. *Surface Science* **1978**, *72*, 710–718.

(120) Sinharoy, S.; Levenson, L. L. *Thin Solid Films* **1978**, *53*, 31–36.

(121) Alcock, C.; Itkin, V.; Horrigan, M. *Canadian Metallurgical Quarterly* **1984**, *23*, 309–313.

(122) Ago, H.; Kugler, T.; Cacialli, F.; Petritsch, K.; Friend, R.; Salaneck, W.; Ono, Y.; Yamabe, T.; Tanaka, K. *Synthetic Metals* **1999**, *103*, 2494–2495.

(123) Shiraishi, M.; Ata, M. *Materials Research* **2001**, *633*, DOI: 10.1016/S0008-6223(00)00322-5.

(124) Klapetek, P.; Nečas, D.; Anderson, C. *Gwyddion User Guide*; tech. rep.; 2018.

(125) Ferreira, T.; Rasband, W. *ImageJ User Guide ImageJ User Guide IJ 1.46r*; tech. rep.; 2012.

(126) Kanafi, M. M. Radial PSD., 2016.

(127) Gao, Y.; Helgeson, M. E. *Optics Express* **2014**, *22*, 10046.

(128) Munson, R. A. *Carbon* **1967**, *5*, 471–474.

(129) Egry, I.; Lohoefer, G.; Jacobs, G. *Physical Review Letters* **1995**, *75*, 4043–4046.

(130) Rozas, R. E.; Demirağ, A. D.; Toledo, P. G.; Horbach, J. *Journal of Chemical Physics* **2016**, *145*, 64515.

(131) Cherne, F. J.; Baskes, M. I.; Deymier, P. A. *Physical Review B - Condensed Matter and Materials Physics* **2002**, *65*, 242091–242099.

(132) Hersam, M. C. *Journal of Physical Chemistry Letters* **2015**, *6*, 2738–2739.

(133) Wang, Q. H.; Kalantar-Zadeh, K.; Kis, A.; Coleman, J. N.; Strano, M. S. *Nature Nanotechnology* **2012**, *7*, 699–712.

(134) Jariwala, D.; Sangwan, V. K.; Lauhon, L. J.; Marks, T. J.; Hersam, M. C. *ACS Nano* **2014**, *8*, 1102–1120.

(135) Sun, L.; Hu, H.; Zhan, D.; Yan, J.; Liu, L.; Teguh, J. S.; Yeow, E. K. L.; Lee, P. S.; Shen, Z. *Small* **2014**, *10*, 1090–5.

(136) Kang, N.; Paudel, H. P.; Leuenberger, M. N.; Tetard, L.; Khondaker, S. I. *The Journal of Physical Chemistry C* **2014**, *118*, 21258–21263.

(137) Islam, M. R.; Kang, N.; Bhanu, U.; Paudel, H. P.; Erementchouk, M.; Tetard, L.; Leuenberger, M. N.; Khondaker, S. I. *Nanoscale* **2014**, *6*, 10033–9.

(138) Wi, S.; Kim, H.; Chen, M.; Nam, H.; Guo, L. J.; Meyhofer, E.; Liang, X. *ACS Nano* **2014**, *8*, 5270–5281.

(139) Chen, M.; Nam, H.; Wi, S.; Priessnitz, G.; Gunawan, I. M.; Liang, X. *ACS Nano* **2014**, *8*, 4023–4032.

(140) Chow, P. K.; Jacobs-Gedrim, R. B.; Gao, J.; Lu, T. M.; Yu, B.; Terrones, H.; Koratkar, N. *ACS Nano* **2015**, *9*, 1520–1527.

(141) CasaXPS User Manual: XPS Spectra., 2013.

(142) Tosun, M.; Chan, L.; Amani, M.; Roy, T.; Ahn, G. H.; Taheri, P.; Carraro, C.; Ager, J. W.; Maboudian, R.; Javey, A. *ACS Nano* **2016**, *10*, 6853–6860.

(143) Fang, H.; Tosun, M.; Seol, G.; Chang, T. C.; Takei, K.; Guo, J.; Javey, A. *Nano Letters* **2013**, *13*, 1991–1995.

(144) Powell, C. J.; Jablonski, A. *NIST Electron Inelastic-Mean-Free-Path Database, Version 1.2*; tech. rep.; Gaithersburg, MD: National Institute of Standards and Technology, 2010.

(145) Yousefi, G. H. *Materials Letters* **1989**, *9*, 38–40.

(146) Ramasubramaniam, A. *Physical Review B - Condensed Matter and Materials Physics* **2012**, *86*, 1–6.

(147) Fang, H.; Chuang, S.; Chang, T. C.; Takei, K.; Takahashi, T.; Javey, A. *Nano Letters* **2012**, *12*, 3788–3792.

(148) Chenming Hu In *Modern Semiconductor Devices for Integrated Circuits*, 2009; Chapter 4, pp 89–156.

# Appendix A

# LEEM Manual

## A.1 Load Lock

### A.1.1 Loading a Sample

1. Make sure your samples are accounted for and there is an empty spot for your new sample. Check that the load lock is fully retracted.
2. Close the turbo pump. Make sure the roughing pump is also closed.
3. Turn on $N_2$ gas (release green knob CCW). You will hear a hiss.
4. Open Swagelock/cap.
5. Load sample (facing downwards) using mini spring arm.
6. Close cap/tighten swagelock.
7. Close valve 1 (to turbo).
8. Open valve 2 (to roughing pump).
9. Watch the pressure decrease on the gray box (above LEED/AES gauge).
10. When P $<$ (=) 0.0 mtorr, close valve 2.
11. Open valve 1 (to the turbo).
12. Open turbo pump. Wait $>$ 10 minutes for pressure to further decrease.
13. Open gate valve to garage to transfer sample inside.

### A.1.2 Removing a Sample

1. Check $P_{garage}$. Make sure the turbo is still running (green light is on/current is $\sim$ 0.2 A).
2. Watch the pressure as you open gate valve to load lock slowly.
3. Lower load lock arm fully. (Don't let it fall down too quickly).
4. Load sample (facing downwards) into load lock.
5. Pull load lock back up.
6. Close gate valve to garage.
7. Close turbo pump.
8. Turn on $N_2$ (release green knob CCW).
9. Open/vent load lock.
10. Take out sample/quickly reload sample as needed.
11. Close cap/tighten Swagelock.
12. Close valve 1 (to turbo).
13. Open valve 2 (to roughing pump).
14. Watch the pressure decrease on the gray box (above LEED/AES gauge).
15. When P $<$ (=) 0.0 mtorr, close valve 2.
16. Open valve 1 (to the turbo).
17. Open turbo pump.
18. Wait $>$10 minutes for pressure to further decrease.

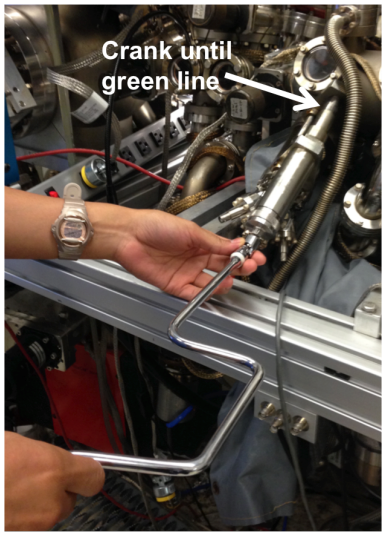


## A.2 Sputter Chamber

### A.2.1 Sample Loading

1. Check to make sure that the transfer arm is retracted from sputter chamber.
2. Use the U-shaped hex tool to move the stage into the chamber until the green line is reached.
3. Use the transfer arm to insert cartridge into sample holder. Be careful of the angle of the cartridge: if it is rotated incorrectly, the metal contact loops under the cartridge will break.

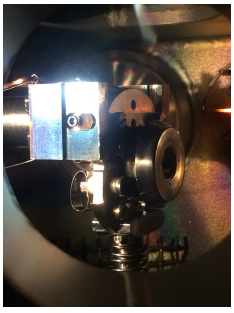

(a)

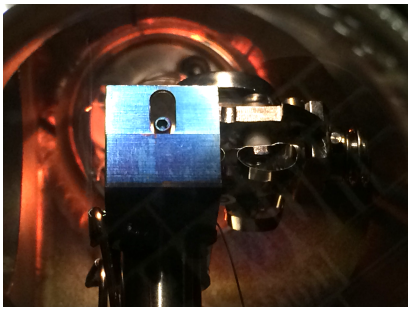

(b)

Figure A.1: (a) Top and (b) side views of sputter chamber.

### A.2.2 $O_2$ Flash Heating

1. Check that both adjacent gate valves are closed.
2. Turn on oxygen by carefully opening the leak valve (turn counterclockwise and press down on the lever to make sure the internal spring is properly compressed) until $P_{sputter} \sim 3$ x $10^{-}8$ torr.
3. Check that cables are plugged in correctly on the sputter chamber.
4. Turn on Kepco High Voltage Power Supply.
5. Set voltage $=$ 990 V.
6. Set current to $\sim$ 100 mA (or whatever is needed, but start small).
7. Press Output On/Off to turn on the power.
8. Check to make sure the leakage current is not too high. Ideally, the current value should be 0 mA if there is no leakage current.
9. If 40" timer is needed, press both green rod buttons at the same time to begin the flash. If not, press the right green rod button only to turn on the circuit.
10. Slowly increase the sample heating filament current (rotate black knob). The current should start to change above filament I $\sim$ 2.00A.
11. Keep increasing filament until desired current setting is reached. Make sure the voltage remains at the set value; otherwise you may need to decrease the filament current or reset the maximum current setting.
12. Use pyrometer to read temperature. Remember to use the filter, set the emissivity according to the material, and turn off the sputter ion gauge before measuring.
13. If only O is used (no Ar), open LEED/AES gate valve for final flash.
14. To turn off:
    a. Turn the sample heating filament current back to 0.
    b. Press both white rod buttons to turn off.
    c. Turn off power supply.
    d. Close $O_2$ valve.

### A.2.3 Ar sputtering

1. Check that both adjacent gate valves are closed.
2. Introduce $\sim 10^{-6}$ torr Ar (carefully open the leak valve by turning counterclockwise while pressing down on the lever).
3. Close shutter.
4. Turn on Ar+ sputtering power.
5. Turn emission up as needed (e.g. 15 mA).
6. Turn on beam energy. Choose beam energy as desired (e.g 0.5, 1, 1.5, or 2 kV).
7. Sputter/flash as needed (see above).
8. Turn off beam energy.
9. Close Ar valve/pump down sputter chamber.

### A.2.4 RGA Measurement

1. Turn on the RGA box (note that the fan will make the LEEM image blurrier so remember to turn it off after use).
2. Plug USB into laptop.
3. Turn on software for RGA measurement.
4. Press filament button.
5. Press MCP button if pressure is sufficiently low ($< 10^{-6}$ torr).
6. Press start on the program to start measuring.
7. You may need to adjust the vertical and horizontal axes as needed.
8. Note that the output is mass. Common peaks include $H_2$ (2), C (12), O (16), CO (28), $CO_2$ (44).
9. Remember to turn off filament, MCP, and RGA after use.

# A.3 LEEM Chamber

## A.3.1 Loading Sample

1. Check pressure gauges. If pressures are all reasonably low ($<10^{-9}$ torr), open the three valves on the horizontal axis.
2. If cartridge is already on transfer arm, move into LEEM chamber. Remember that the sample should be facing the electron gun (toward the wall with Auger system/toward the pressure gauge readouts).
3. Carefully align sample edges in holder rails by adjusting the vertical/horizontal location. It will be helpful to look through the view window at the side end of the instrument.
4. Gently push transfer arm slightly further inward.
5. Rotate transfer arm $90^o$; long pins should be perpendicular to the face of the sample in the final state (for release).
6. Pull out transfer arm carefully, checking to make sure that cartridge does not come out with it.
7. Lightly tap sample to ensure it is fully in the holder.
8. Pull out transfer out all the way back to the LEED chamber. Close gate valves.
9. Check that the shutter is open (open shutter = open camera). Rotate large stage knob while holding a thumb in place to prevent sample crashing.
10. Continue rotating large knob until the sample looks very close to the lens but not yet touching. Be careful not to crash the sample! Better safe than sorry–this can damage the sample and cause sparks in the chamber.
11. Continue to Getting an Image.

## A.3.2 Removing Sample

1. Realign tilt back to center position. (Stage has markings showing approximate final location)
2. Retract stage by rotating large knob (CCW) until it stops rotating.

3. Check pressure gauges. If pressures are all reasonably low (¡10-9 torr), open the three valves on the horizontal axis.
4. Pull transfer arm into LEEM chamber. Be careful that the arm is centered while maneuve ring through closed regions.
5. Align pins such that the tip is aligned with the cartridge hole and the long pins are horizontal (perpendicular to sample direction).
6. Continue pushing forward gently.
7. Rotate knob $90^o$, and pull out.
8. Watch the sample while pulling out to avoid crashing.

### A.3.3 Flash Heating

1. Make sure voltage plugs are plugged in correctly. For the LEEM chamber, the red wire should be connected to the black wire labeled with red tape. (As a polarity check, electron beam should move downward as voltage increases).
2. Turn on power of KEPCO high voltage power supply.
3. Set voltage (e.g. 850 V). (Press "V set", then enter value, then enter.)
4. Set current maximum. (Press "I set", then enter value, then enter.)
5. Press green current button to turn on filament.
6. Slowly increase sample heating filament by turning black knob. The current display on the bottom box should start increasing after 2.1 A
7. Watch to make sure that the voltage is maximized and current is at the set point. If the current is too low, increase the filament slightly. If the voltage is decreasing, decrease the filament to optimize the values.
8. During heating, a few things may happen:
   – beam may shift downward. Solution: adjust the gun deflector Y.
   – sample may drift. Solution: adjust the stage to realign the sample.
   – sample may expand. Solution: decrease the focus.
9. See LEEM Measurements.

### A.3.4 Evaporation (*e.g.*, Nickel Dosing)

1. Always double check that water cooling line is running (tap on water lines). Make sure that the water level in the bucket in the top corner of the room is filled to the top of the red tape (should always be up to there).
2. Nickel: assume ∼4 minutes per monolayer. Every 8 minutes, 0.35 nm (note that this number might be slightly different because it was calibrated on Co).
3. Turn on MgO e-beam HV.
4. Turn on MgO e-beam filament.
5. Press HV on button.
6. Set to 25 W and stabilize power at 25W (wait for 5 minutes).
7. Make sure shutter is closed.
8. Open shutter to deposit.
9. Close shutter when done.
10. Turn off red HV button.
11. Then turn off green button.
12. Turn off MgO filament.

## A.4 LEEM Measurements

### A.4.1 Turning on the Cathode

1. Top box: Turn on current to 3.4-3.7A (should be the max).
2. Watch until emission current peaks.
3. Lower cathode to 0V when the current peaks/saturates. Otherwise, leave at ∼1 or 2V.

### A.4.2 Notes on Finding the Beam

(a) Use trackpad to adjust items so we can undo the action. If the beam is lost and a parameter is changed, change something. (Make sure mouse is on the SPLEEM control window so it works.)

(b) If beam is not flat: adjust rotator (optimal ∼220V), C (∼1200V), D.

(c) Note that stigmation has a huge effect on how well we can adjust the image. (but much more difficult). Astigmatism: steps show up, but maybe more contrast/crisper steps in one direction than another

Adjusting the beam itself:

– Don't touch the magnets! Hysteresis effects prevent going back.

– Don't change objective deflector.

– Simultaneously adjust the following to get beam as bright and flat as possible:

- Gun deflector (X,Y)

- Illumination deflector (X,Y).

- C, D Potential Controls (gentler than A, B). Change these in conjunction w/ gun deflector.

- Rotator Potential Control (beam shape).

- Knock top of chamber with big wrench to ensure stability.

### A.4.3 Getting an Image

1. Open shutter and make sure camera is on.
2. Rotate sample stage closer to beam (CW), until it is about 3 ridges away from the plates. (Place your thumb in the gap to prevent crashing). Or until cartridge front appears very close to the lens on the screen. You can tell where it is by the reflection.
3. Open ImageJ SPLEEM plugin until image appears. Make sure the screen is live (not frozen).
4. Circle the region of interest (inside the black circle).
5. Start with an exposure time of 250ms so the refresh rate is fast.

6. Start with Projective 1 at a high setting (∼800V) to see the entire "footprint" of the beam.
7. Starting at a higher start voltage (e.g. 15V), slowly increase MCP gain until "snow" appears. If snow is very faint, you may need to adjust the projector lens. If it's still faint, use the gun deflector to bring the bright spot to the center.
8. Decrease the start voltage until the snow disappears/becomes very faint.
9. Adjust the tilt to maximize the intensity. Keep an eye on the image–if it gets too bright, immediately decrease the MCP so as not to overexpose.
10. Repeat steps 7-8 until you reach a low voltage/until you can go down to a start voltage of 0V.
11. Optimize the tilt at 0V.
12. Change the exposure time to 1s for a better integration time/clearer image.
13. Adjust MCP so the initial intensity at 0V is ∼210.
14. Adjust focus until beam shape looks correct (slightly ovular). E.g. start at 1800-2200 V until you see a clear image. Then decrease back to 1800 V and move stage closer until you recover the image (may need to retilt). (Ideal objective focus ∼1100, 1200V.)
15. Adjust the beam with the gun/image deflectors as needed. (Want "flat" beam–smooth/homogeneous.)
16. Go back to a higher voltage (e.g., 4V) to get a clearer image.
17. Return to Projective 1: 338.2V (known magnification: FOV = 12 $\mu$m diameter).
18. Readjust the focus. (If image is still blurry, check that the RGA is off).

### A.4.4 Taking a Spectrum

1. Create a new folder.
2. Edit Macros → 1 spectrum:

   Don't need to change other numbers except:

   frames = 1

   start_E = 0

step_E = 0.1

stop_E = 20

3. Press Simple Spectrum: Start.

### A.4.5 Restarting ImageJ

1. Quit ImageJ.
2. On SPLEEM Main Control Window: Tools → TCP/IP Interface.
3. In the interface: press Stop. then Start.
4. Open ImageJ again.
5. ImageJ → Plugins → Spleem_ → Spleem.
6. TCP/IP Interface should be green/say Connected. MIDI board should restart.

### A.4.6 Analyzing Data

1. Load sequence (File → Import → Image sequence, specify number of images).
2. Circle area of interest (full FOV = 450x450 pixels).
3. Images → Stacks → Plot Z-axis profile.

## A.5 Auger Electron Spectroscopy

1. Move sample to LEED chamber and face the sample toward the AES detector (toward the pump controller).
2. Turn off LEED/AES ion gauge by switching the lower left-hand side button (labeled "Filament").
3. Align sample vertically to the marked AES line and horizontally to the end of the plate (away from the pump controller).
4. Check that the sample is vertical. If not, the Auger spectrum may be shifted.
5. Turn on power of Electron Gun Supply.
6. Turn on power of Electron Multiplier Supply.

7. Turn on power switch on Digital AES Control.
8. Press red On button for beam voltage.
9. Slowly increase emission current until ∼0.1 mA emission current is detected. (∼5.5 turns–overturn, then return to 5.5 tick mark.)
10. Open AugerScan program on desktop. (You may need to click OK for a few windows first.)
11. File → New Acquisition.
    a. Select Survey.
    b. Select AES.
    c. Press OK.
12. Acquisition → Settings.
    a. For a general sweep, start with:
       i. Start voltage: 30 eV
       ii. End voltage: 1000 eV
       iii. Step size: 0.5 eV
       iv. Sweeps: 1-3 (or as desired)
       v. Time/step: 50 mS
    b. Adjust as needed.
13. Press acquire and let program run. If spectrum becomes saturated at high energies, decrease the emission current slightly and retake.
14. Analyze data as needed (book is in drawer under the computer).
15. Remember to save as both .ASN and .txt so you can still access the data without the software.

## A.6 Low-Energy Electron Diffraction

### A.6.1 Taking a LEED pattern

1. Align sample to center (follow AES line for vertical reference, center tick for horizontal reference). Sample should face the LEED camera (away from pump controller).

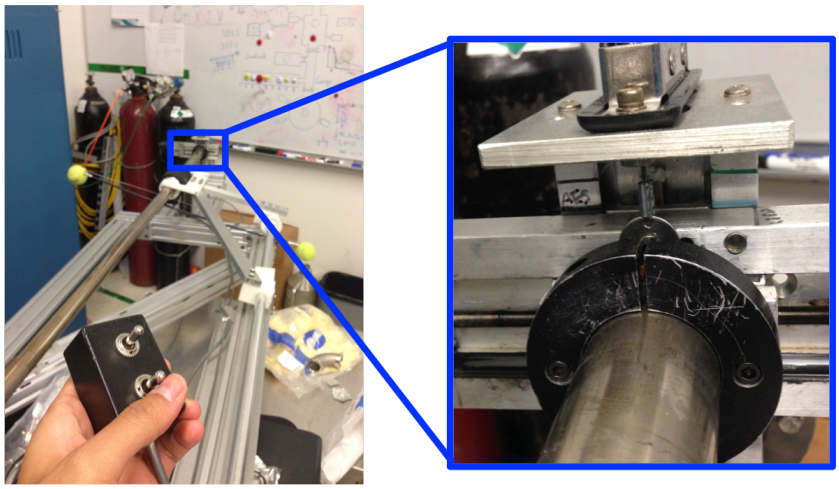

2. Turn on white Power button.
3. Turn on red HV On button.
4. Turn on I Max button.
5. Turn on Power switch.
6. Slowly increase voltage to 4 kV using black knob. Watch the right meter while rotating (ignore the knob numbers).
7. Very slowly increase Filament I to 1.7 A (1.65 A to be safe) (update 10/24/2017: 1.9A to get correct emission). There is a strong delay, so be careful. Value shows on screen if DPM is on correct mode ("Filament I A").

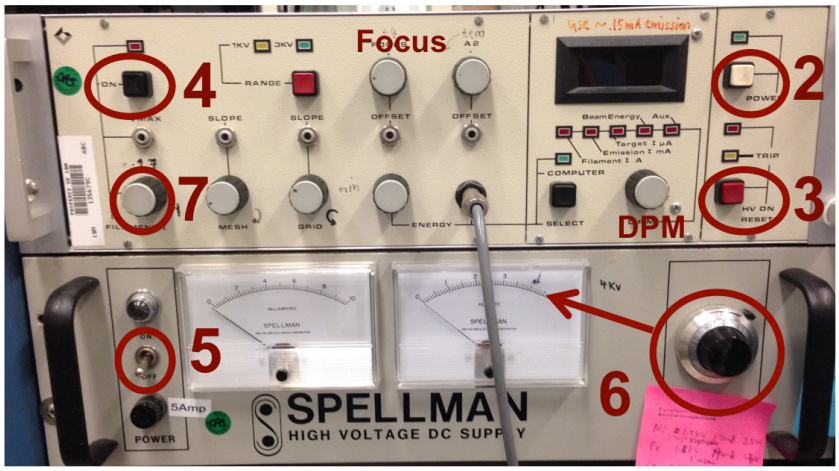

8. Turn off LEED/AES ion gauge by switching the lower left-hand side button (labeled "Filament"). This will darken the LEED chamber and let you better see your diffraction spots.

9. Place and align camera hardware onto the LEED chamber.

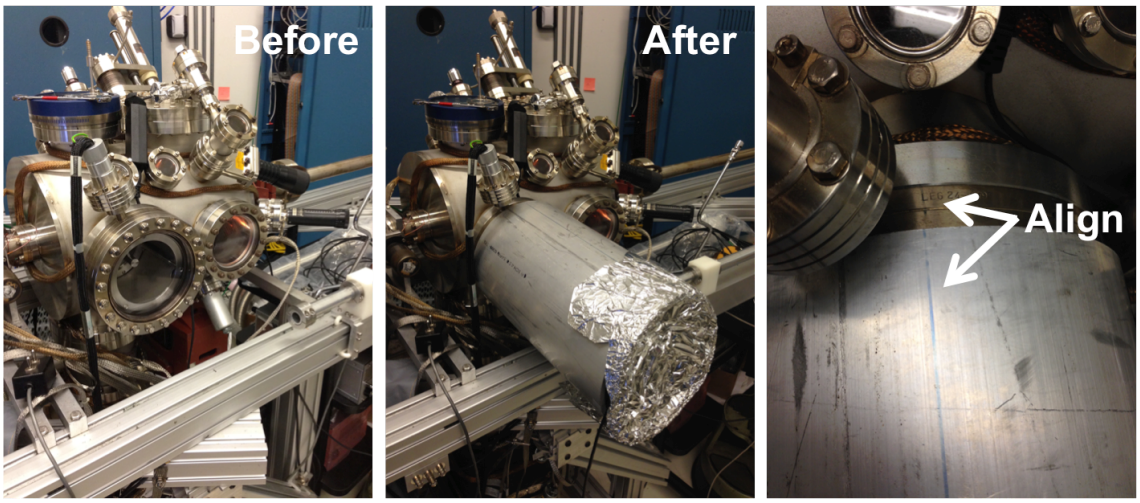


10. Open UC480 viewer on the computer desktop, select for video, and press play. Turn off room lights and cover the camera system if possible.

11. Switch DPM knob to beam energy. Adjust beam energy (usually in the range of 0.057–0.200 V) until you see a good diffraction pattern.

12. Adjust focus knob until you get a crisp image. If your image isn't clear and you are below 1.7 mA (step 7) increase carefully increase to 1.7, adjust beam energy and focus as needed.

13. If the image still isn't clear, adjust the position of the sample using the transfer arm.

14. When done, save image.

15. Turn down the beam energy and save another image for background subtraction.

16. Turn down HV from 4 kV to 0 (knob 6) and switch power supply OFF (switch 5). Turn down filament from 1.7 to 0 (knob 7) and switch OFF filament power (button 4). Turn OFF HV ON (red button 3) and turn OFF main power (white button 2).

### A.6.2 LEED Image Processing (General)

1. Import both images (pattern + background) into ImageJ.
2. Open Image → Calculator. Input:

   Image 1 = LEED image of interest.

   Action: subtract.

   Image 2 = bg (make sure the settings are the same when taking the image).
3. Optional: invert image (CTRL + SHIFT +I) and adjust the contrast (CTRL + SHIFT + C) as needed.